

**Abstract**

**Measurement of total hadronic differential cross  
sections in the LArIAT experiment**

Elena Gramellini

2018

Abstract goes here. Limit 750 words.

# **Measurement of total hadronic differential cross sections in the LArIAT experiment**

A Dissertation  
Presented to the Faculty of the Graduate School  
of  
Yale University  
in Candidacy for the Degree of  
Doctor of Philosophy

by  
Elena Gramellini

Dissertation Director: Bonnie T. Fleming

Date you'll receive your degree

Copyright © 2017 by Elena Gramellini

All rights reserved.

# Contents

<b>Acknowledgements</b>	<b>iv</b>
<b>0 Introduction</b>	<b>1</b>
<b>1 The theoretical framework</b>	<b>2</b>
1.1 The Standard Model . . . . .	2
1.2 Neutrinos: tiny cracks in the Standard Model . . . . .	4
1.2.1 Neutrinos in the Standard Model . . . . .	4
1.2.2 Neutrino Oscillations . . . . .	6
1.2.3 Make up of Neutrino Interactions . . . . .	7
1.3 Beyond the Standard Model . . . . .	11
1.3.1 Open Questions in Neutrino Physics . . . . .	11
1.3.2 Towards a more fundamental theory: GUTs . . . . .	15
1.4 Motivations for Hadronic Cross Sections in Argon . . . . .	18
1.4.1 Pion-Argon Total Hadronic Cross Section . . . . .	19
1.4.2 Kaon-Argon Total Hadronic Cross Section . . . . .	29
<b>2 Liquid Argon Detectors at the Intensity Frontier</b>	<b>34</b>
2.1 The Liquid Argon Time Projection Chamber Technology . . . . .	34
2.1.1 TPCs, Neutrinos & Argon . . . . .	34
2.1.2 LArTPC: Principles of Operation . . . . .	36

2.1.3	Liquid Argon: Ionization Charge . . . . .	38
2.1.4	Liquid Argon: Scintillation Light . . . . .	42
2.1.5	Signal Processing and Event Reconstruction . . . . .	46
2.2	The Intensity Frontier Program . . . . .	49
2.2.1	SBN: Neutrino Interaction and Detection . . . . .	49
2.2.2	DUNE: Rare Decay Searches . . . . .	49
2.2.3	Enabling the next generation of discoveries: LArIAT . . . . .	49
<b>3</b>	<b>LArIAT: Liquid Argon In A Testbeam</b>	<b>52</b>
3.1	The Particles Path to LArIAT . . . . .	52
3.2	LArIAT Tertiary Beam Instrumentation . . . . .	55
3.2.1	Bending Magnets . . . . .	55
3.2.2	Multi-Wire Proportional Chambers . . . . .	57
3.2.3	Time-of-Flight System . . . . .	59
3.2.4	Punch-Through and Muon Range Stack Instruments . . . . .	60
3.2.5	LArIAT Cosmic Ray Paddle Detectors . . . . .	62
3.3	In the Cryostat . . . . .	63
3.3.1	Cryogenics and Argon Purity . . . . .	63
3.3.2	LArTPC: Charge Collection . . . . .	66
3.3.3	LArTPC: Light Collection System . . . . .	69
3.4	Trigger and DAQ . . . . .	72
3.5	Control Systems . . . . .	73
<b>4</b>	<b>Hadron Interactions in Argon: Cross Section</b>	<b>79</b>
4.1	How to Measure a Hadron Cross Section in LArIAT . . . . .	79
4.1.1	Event Selection . . . . .	80
4.1.2	Wire Chamber to TPC Match . . . . .	82
4.1.3	The Thin Slice Method . . . . .	83

4.1.4	Procedure testing with truth quantities . . . . .	86
<b>A</b>	<b>Measurement of LArIAT Electric Field</b>	<b>89</b>

# Acknowledgements

A lot of people are awesome, especially you, since you probably agreed to read this when it was a draft.

# **Chapter 0**

## **Introduction**

# Chapter 1

## The theoretical framework

### 1.1 The Standard Model

The Standard Model (SM) of particle physics is the most accurate theoretical description of the subatomic world and, in general, one of the most precisely tested theories in the history of physics. The SM describes the strong, electromagnetic and weak interactions among elementary particles in the framework of quantum field theory, accounting for the unification of electromagnetic and weak interactions for energies above the vacuum expectation value (VEV) of the Higgs field. The SM does not describe gravity or general relativity.

The Standard Model is a gauge theory based on the local group of symmetry

$$G_{SM} = SU(3)_C \otimes SU(2)_T \otimes U(1)_Y \quad (1.1)$$

where the subscripts indicate the conserved charges: the strong charge, or color C, the weak isospin T (or rather its third component T<sub>3</sub>) and the hypercharge Y. These quantities can be related to the electric charge Q through the Gell-Mann-Nishijima relation:

$$Q = \frac{Y}{2} + T_3. \quad (1.2)$$

Generation	I	II	III	T	Y	Q
Leptons	$\begin{pmatrix} \nu_e \\ e \end{pmatrix}_L$	$\begin{pmatrix} \nu_\mu \\ \mu \end{pmatrix}_L$	$\begin{pmatrix} \nu_\tau \\ \tau \end{pmatrix}_L$	1/2 -1/2	-1 -1	0 -1
	$e_R$	$\mu_R$	$\tau_R$	0	-2	1
Quarks	$\begin{pmatrix} u \\ d' \end{pmatrix}_L$	$\begin{pmatrix} c \\ s' \end{pmatrix}_L$	$\begin{pmatrix} t \\ b' \end{pmatrix}_L$	1/2 -1/2	1/3 1/3	2/3 -1/3
	$u_R$ $d'_R$	$c_R$ $s'_R$	$t_R$ $b'_R$	0 0	4/3 -2/3	2/3 -1/3

Table 1.1: SM elementary fermions. The subscripts L and R indicate respectively the negative helicity (left-handed) and the positive helicity (right-handed).

In the quantum field framework, the elementary particles correspond to the irreducible representations of the  $G_{SM}$  symmetry group. In particular, the particles are divided in two categories, fermions and bosons, according to their spin-statistics. Described by the Fermi-Dirac statistics, fermions have half-integer spin and are sometimes called “matter-particles”. Bosons or “force carriers” have integer spin, follow the Bose-Einstein statistics and mediate the interaction between fermions. The fundamental fermions and their quantum numbers are listed in Tab 1.1.

Quarks can interact via all three the fundamental forces; they are triplets of  $SU(3)_C$ , that is they can exist in three different colors: C = R, G, B. If one chooses a base where  $u$ ,  $c$  and  $t$  quarks are simultaneously eigenstates of both the strong and the weak interactions, the remaining eigenstates are usually written as  $d$ ,  $s$  and  $b$  for the strong interaction and  $d'$ ,  $s'$  and  $b'$  for the weak interaction, because the latter ones are the result of a Cabibbo rotation on the first ones. Charged leptons interact via the weak and the electromagnetic forces, while neutrinos only interact via the weak force. The gauge group univocally determines the number of gauge bosons that carry the interaction; the gauge bosons correspond to the generators

of the group: eight gluons (g) for the strong interaction, one photon ( $\gamma$ ) and three bosons ( $W^\pm$ ,  $Z^0$ ) for the electroweak interaction. A gauge theory by itself can not provide a description of massive particles, but it is experimentally well known that most of the elementary particles have non-zero masses. The introduction of massive fields in the Standard Model lagrangian would make the theory non-renormalizable, and - so far - mathematically impossible to handle. This problem is solved in the SM by the introduction of a scalar iso-doublet  $\Phi(x)$ , the Higgs field, which gives mass to  $W^\pm$  and  $Z^0$  gauge bosons through the electroweak symmetry breaking mechanism and to the fermions through Yukawa coupling [48, 49]. The discovery of the Higgs boson in 2012 by the LHC experiments [21, 22] marked the ultimate confirmation of a long history of successful predictions by the SM.

## 1.2 Neutrinos: tiny cracks in the Standard Model

### 1.2.1 Neutrinos in the Standard Model

Neutrino were introduced in the SM as left-handed massless Weyl spinors. The Dirac equation of motion

$$(i\gamma^\mu \partial_\mu - m)\psi = 0 \quad (1.3)$$

for a fermionic field

$$\psi = \psi_L + \psi_R \quad (1.4)$$

is equivalent to the equaitons

$$i\gamma^\mu \partial_\mu \psi_L = m\psi_R \quad (1.5)$$

$$i\gamma^\mu \partial_\mu \psi_R = m\psi_L \quad (1.6)$$

for the chiral fields  $\psi_R$  and  $\psi_L$ , whose evolution in space and time is coupled through the mass  $m$ . If the fermion is massless, the chiral fields decouple and the

fermion can be described by a single Weyl spinor with two independent components [73]. Pauli initially rejected the description of a physical particle through a single Weyl spinor because of its implication of parity violation. In fact, since the spatial inversion operator throws  $\psi_R \leftrightarrow \psi_L$ , parity is conserved only if the both the chiral components exist at the same time. For the neutrino introduction in the SM, experiments came in help of the theoretical description. The constraint of parity conservation weakened after Wu's experiment in 1957 [76]. Additionally, there was no experimental indication for massive neutrinos, nor evidence of interaction via the neutrino right-handed component.

The symmetry group  $SU(2)_T \otimes U(1)_Y$  is the only group relevant for neutrino interactions. The SM electroweak lagrangian is the most general renormalizable lagrangian invariant under the local symmetry group  $SU(2)_T \otimes U(1)_Y$ . The lagrangian couples the weak isotopic spin doublets and singlets described in Table 1.1 with the gauge bosons  $A_a^\mu$  ( $a = 1, 2, 3$ ) and  $B^\mu$ , and Higgs doublet  $\Phi(x)$ :

$$\begin{aligned}
\mathcal{L} = & i \sum_{\alpha=e,\mu,\tau} \bar{L}'_{\alpha L} \not{D} L'_{\alpha L} + i \sum_{\alpha=1,2,3} \bar{Q}'_{\alpha L} \not{D} Q'_{\alpha L} \\
& + i \sum_{\alpha=e,\mu,\tau} \bar{l}'_{\alpha R} \not{D} l'_{\alpha R} + i \sum_{\alpha=d,s,b} \bar{q}'^D_{\alpha R} \not{D} q'^D_{\alpha R} + i \sum_{\alpha=u,c,t} \bar{q}'^U_{\alpha R} \not{D} q'^U_{\alpha R} \\
& - \frac{1}{4} A_{\mu\nu} A^{\mu\nu} - \frac{1}{4} B_{\mu\nu} B^{\mu\nu} \\
& + (D_\rho \Phi)^\dagger (D^\rho \Phi) - \mu^2 \Phi^\dagger \Phi - \lambda (\Phi^\dagger \Phi)^2 \\
& - \sum_{\alpha,\beta=e,\mu,\tau} \left( Y_{\alpha\beta}^n \bar{L}'_{\alpha L} \Phi l'_{\beta R} + Y_{\alpha\beta}^{n*} \bar{l}'_{\beta R} \Phi^\dagger L'_{\alpha L} \right) \\
& - \sum_{\alpha=1,2,3} \sum_{\beta=d,s,b} \left( Y_{\alpha\beta}^D \bar{Q}'_{\alpha L} \Phi q'^D_{\beta R} + Y_{\alpha\beta}^{D*} \bar{q}'^D_{\beta R} \Phi^\dagger Q'_{\alpha L} \right) \\
& - \sum_{\alpha=1,2,3} \sum_{\beta=u,c,t} \left( Y_{\alpha\beta}^U \bar{Q}'_{\alpha L} \tilde{\Phi} q'^U_{\beta R} + Y_{\alpha\beta}^{U*} \bar{q}'^U_{\beta R} \tilde{\Phi}^\dagger Q'_{\alpha L} \right). \tag{1.7}
\end{aligned}$$

The first two lines of the lagrangian summarize the kinetic terms for the fermionic

fields and their coupling to the gauge bosons  $A_a^{\mu\nu}$ ,  $B^{\mu\nu}$ <sup>1</sup>. The third line describes the kinetic terms and the self-coupling terms of the gauge bosons. The forth line is the Higgs lagrangian, which results in the spontaneous symmetry breaking. The last three lines describe the Yukawa coupling between fermions and the Higgs field, origin of the fermions' mass.

The coupling between left-handed and right-handed field generates the mass term for fermions. The SM assumes only left-handed components for neutrinos, thus implying zero neutrino mass. Since any linear combination of massless fields results in a massless field, the flavor eigenstates are identical to the mass eigenstates in the SM.

### 1.2.2 Neutrino Oscillations

The determination of the flavor of a neutrino dynamically arises from the corresponding charged lepton associated in a change current interaction; for example, a  $\nu_e$  is a neutrino which produces an  $e^-$ , a  $\bar{\nu}_\mu$  is a neutrino which produces a  $\mu^+$ , *etc.* The neutrino flavor eigenstates  $|\nu_\alpha\rangle$ , with  $\alpha = e, \mu, \tau$ , are orthogonal to each other and form a base for the weak interaction matrix.

Overwhelming experimental data show neutrinos change flavor during their propagation [64]. This phenomenon, called “neutrino oscillations”, was predicted first by Bruno Pontecorvo in 1957 [65]. Neutrino oscillations are possible only if the neutrino flavor eigenstate are not identical to the mass eigenstates, thus resulting in the first evidence of physics beyond the Standard Model. A minimal extension of the SM introduces three mass eigenstates,  $|\nu_i\rangle$  ( $i = 1, 2, 3$ ), whose mass  $m_i$  is well defined. The unitary Pontecorvo-Maki-Nakagawa-Sakata matrix transforms the spinor wave functions ( $\psi$ ) of each component between the flavor and mass bases as follows

---

1. In gauge theories the ordinary derivative  $\partial_\mu$  is substituted with the covariant derivative  $D_\mu$ . Here  $D_\mu = \partial_\mu + igA_\mu \cdot I + ig'B_\mu \frac{Y}{2}$ , where I and Y are the SU(2)<sub>L</sub> and U(1)<sub>Y</sub> generators, respectively.

$$\sum_{\alpha} \psi_{\alpha} |\nu_{\alpha}\rangle = \sum_i \psi_i |\nu_i\rangle, \rightarrow \psi_{\alpha} = U_{PMNS} \psi_i, \quad (1.8)$$

with

$$U_{PMNS} = \begin{bmatrix} c_{12} & s_{12} & 0 \\ -s_{12} & c_{12} & 0 \\ 0 & 0 & 1 \end{bmatrix} \begin{bmatrix} c_{13} & 0 & s_{13} e^{-i\delta} \\ 0 & 1 & 0 \\ -s_{13} e^{-i\delta} & 0 & c_{13} \end{bmatrix} \begin{bmatrix} 1 & 0 & 0 \\ 0 & c_{23} & s_{23} \\ 0 & -s_{23} & c_{23} \end{bmatrix} \begin{bmatrix} e^{i\alpha_1} & 0 & 0 \\ 0 & e^{i\alpha_2} & 0 \\ 0 & 0 & 1 \end{bmatrix} \quad (1.9)$$

where  $c$  e  $s$  stand respectively for cosine and sine of the corresponding mixing angles ( $\theta_{12}$ ,  $\theta_{23}$  and  $\theta_{13}$ ),  $\delta$  is the Dirac CP violation phase,  $\alpha_1$  and  $\alpha_2$  is the eventual Majorana CP violation phases. Experimental results on neutrino oscillations are generally reported in terms of the mixing angles and of the squared mass splitting  $\Delta m_{ab}^2 = m_a^2 - m_b^2$ , where  $a$  and  $b$  represent the mass eigenstates. A summary of the current status of experimental results, albeit partial, is given in table 1.2.

Table 1.2: Summary of experimental results on neutrino oscillation parameters. **ADD CITATIONS**

	Value	Precision	Experiment
$\theta_{23}$	$45^\circ$	9.0%	Super Kamiokande, MINOS,
$\Delta m_{23}^2$	$2.5 \cdot 10^{-3} \text{ eV}^2$	1.8%	No $\nu$ a, MACRO
$\theta_{12}$	$34^\circ$	5.8%	SNO, Gallex,
$\Delta m_{12}^2$	$7.4 \cdot 10^{-5} \text{ eV}^2$	2.8%	SAGE, KamLAND
$\theta_{13}$	$9^\circ$	4.7%	DAYA Bay,
$\Delta m_{13}^2$	$2.5 \cdot 10^{-3} \text{ eV}^2$	1.8%	RENO

### 1.2.3 Make up of Neutrino Interactions

All neutrino experiments involving the detection of single neutrinos are concerned with neutrino interactions (and neutrino cross sections) on nuclei. Given the invisible nature of the neutrino, characterizing the products of its interaction is the only

method to a) assess the neutrino presence, b) detect its flavor in case of a charge current interaction and c) eventually reconstruct its energy.

Historically, neutrino interactions with the nucleus in the GeV region are divided into three categories as a function of increasing neutrino energy: quasi elastic (QE), resonant, and deep inelastic (DIS) scattering. All current and forthcoming oscillation experiments live in the 0.1-10 GeV transition region, which encompasses the energy where the QE neutrino-nucleus interaction transitions into resonant scattering and the energy where resonance scattering transitions into DIS. Schematically, neutrino and antineutrino QE charge current scattering refers to the process  $\nu_l n \rightarrow l^- p$  and  $\bar{\nu}_l p \rightarrow l^+ n$  where a charged lepton and single nucleon are ejected in the elastic interaction, leaving the target nucleus in its ground state. Resonant scattering refers to an inelastic collision producing a nucleon excited state ( $\Delta, N^*$ ) – the resonance, indeed – which then quickly decays, most often to a nucleon and single-pion final state. DIS refers to the head-on collision between the neutrino and a parton inside the nucleon, producing hadronization and subsequent abundant production of mesons and nucleons. In addition to such interactions between the neutrino and a single component of the nucleus, neutrinos can also interact with the nucleus as a whole, albeit more rarely, a well documented process called coherent meson production scattering [36]; the signature of such process is the production of a distinctly forward-scattered single meson final state, most often a pion. This simple picture of neutrino interactions works rather well for scattering off of light nuclear targets, such as the H<sub>2</sub> and D<sub>2</sub> of bubble chamber experiments [39], but the complexity of the nuclear structure for heavier nuclei such as argon complicates this model.

As we will discuss in Chapter 2, the properties of argon make it a good candidate for interacting medium in neutrino experiments; in particular the density of its interaction centers augments the yield of neutrino interactions and allows for relatively compact detectors. Though, the choice of a relatively heavy nuclear target comes at

the cost of enhancing nuclear effects which modify the kinematic and final state of the neutrino interaction products.

Nuclear effects can potentially affect the neutrino event rates, nucleon emission, neutrino energy reconstruction, and the neutrino/antineutrino ratios, carrying deep implications for oscillation experiments. Even in the case of “simple” QE scattering, intra-nuclear hadron rescattering and correlation effects between the target nucleons can cause the ejection of additional nucleons in the final state, modifying the final state kinematics and topology. In case of resonant and DIS scattering, the hadronic interactions of meson and nucleons produced in the decay of the resonance or during hadronization complicate this picture even more. A large source of uncertainty in modeling nuclear effects in neutrino interactions come from mesons interactions (and re-interactions) in the nucleus, e.g., pion re-scattering, charge exchange, and absorption.

A renewed interest for neutrino cross section measurements surged in recent years, along with a lively discussion on the data reporting; the historical method of reporting the neutrino cross section as a function of the neutrino energy or momentum transferred shakes under the weight of its dependency on the chosen nuclear model. On one hand, correcting for nuclear effects in neutrino interaction can introduce unwanted sources of uncertainty and model dependency especially due to the mis-modeling of the meson interactions. On the other, avoiding this correction makes a comparison between neutrino interactions on different target nuclei extremely difficult.

Data on neutrino scattering off many different nuclei are available for both charged current (CC) and neutral current (NC) channels, as summarized in [39]. A summary of the results on QE, resonant and DIS scattering for neutrinos and antineutrinos from accelerators on different target is reported in Figure 1.1, where the (NUANCE) [19] event generator is used as comparison with the theory.

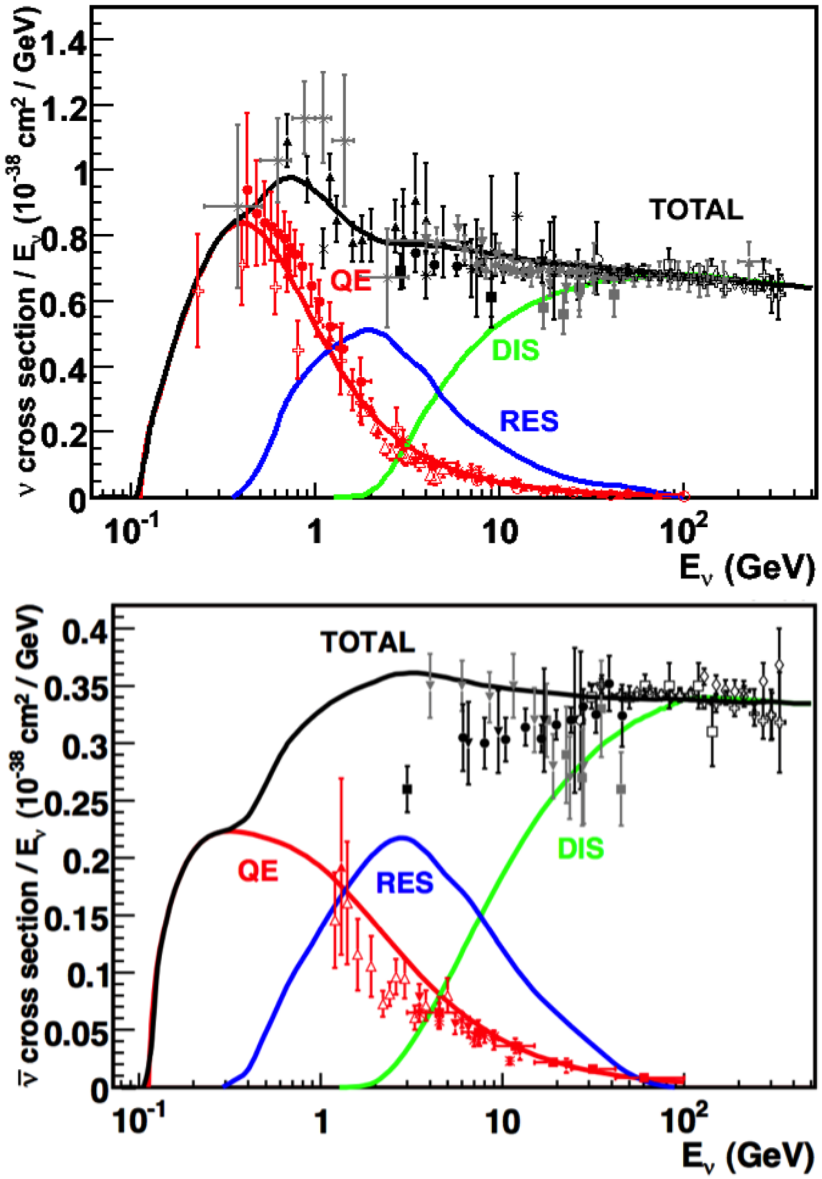


Figure 1.1: Total neutrino (top) and antineutrino (bottom) CC cross sections per nucleon divided by neutrino energy as a function of energy as reported in [39]. Predictions for the total (black), the QE (red), resonant (blue) and DIS (green) are provided by the NUANCE generator. The quasi-elastic scattering data and predictions have been averaged over neutron and proton targets (isoscalar target).

## 1.3 Beyond the Standard Model

The discovery of neutrino oscillation and its implication of non-zero neutrino mass mark the beginning of a new, exciting era in neutrino physics: the era of physics Beyond the Standard Model (BSM) at the intensity frontier. We are currently searching for new, deeper theories that can accommodate neutrinos with tiny but non-zero masses, while remaining consistent with the rest of the Standard Model.

### 1.3.1 Open Questions in Neutrino Physics

On one hand, the last three decades of experiments in neutrino oscillations brought spectacular advancements in the understanding of the oscillations pattern, measuring the neutrino mixing angles and mass splitting with a precision of less than 10%. On the other, it opened the field for a series of questions needing experimental answers.

**Sterile neutrinos.** Hints to the existence of at least one additional neutrino, in the form of various anomalies, have been puzzling physicists almost from the beginning of neutrino oscillation searches. Originally designed to look for evidence of neutrino oscillation, the Liquid Scintillator Neutrino Detector (LSND) [32] provided a first conflicting result with the Standard Model expectation of only three neutrinos. A second conflicting result has also been provided by the MiniBooNE experiment [28]. The LSND and MiniBooNE  $\nu_e$  and  $\bar{\nu}_e$  appearance results, known as the “LSND and MiniBooNE anomalies” [7, 8, 13], may be interpreted under the assumption of a new right-handed neutrino. The additional neutrino needs to be “sterile”, i.e needs not to couple with the electroweak force carriers, in order to meet the constraint imposed by the measurement of the width of the Z boson [1]. The new sterile neutrino would mainly be composed of a heavy neutrino  $\nu_4$  with mass  $m_4$  such that  $m_1, m_2, m_3 \ll m_4$  and  $\Delta m^2 = \Delta m_{14}^2 \sim [0.1 - 10] \text{ eV}^2$ . The introduction of sterile neutrinos is an appealing line of thinking, since this renormalizable generalization of the SM has the

potential to impact long standing questions in high energy physics and cosmology: light sterile neutrinos are candidates for dark matter particles and there are ideas that the theory could be adjusted to explain the baryon asymmetry of the Universe via leptogenesis [45].

**CP Violation In Lepton Sector.** The measurement of non-zero value for the oscillation parameter  $\theta_{13}$  allows the exploration of low-energy CP violation in the lepton sector at neutrino long baseline oscillation experiments, enabling the possibility to measure the Dirac CP-violating phase  $\delta$ . Exciting theoretical results tie  $\delta$  directly to the generation of the baryon asymmetry of the Universe at the Grand Unified Theory scale [a couple of cit would be nice](#). According to the theoretical model described in [63], for example, leptogenesis can be achieved if  $|\sin \theta_{13} \sin \delta| > 0.11$ , i.e.  $\sin \delta > 0.7$ .

The asymmetry in the oscillation probability of neutrinos and antineutrinos is the observable sensitive to the Dirac CP-violating phase  $\delta$  leveraged in neutrino oscillation experiments. Using the parameterization of the PMNS matrix shown in Equation 1.9, the difference between the probability of  $\nu_e \rightarrow \nu_\mu$  oscillation and the probability of  $\bar{\nu}_e \rightarrow \bar{\nu}_\mu$  oscillation can be parametrized as follows [20],

$$P_{\nu_e \rightarrow \nu_\mu} - P_{\bar{\nu}_e \rightarrow \bar{\nu}_\mu} = J \cos \left( \pm \delta - \frac{\Delta_{31} L}{2} \right) \sin \left( \frac{\Delta_{21} L}{2} \right) \sin \left( \frac{\Delta_{31} L}{2} \right) \quad (1.10)$$

where

$$J = \cos \theta_{13} \sin 2\theta_{13} \sin 2\theta_{12} \sin 2\theta_{23} \quad (1.11)$$

is the Jarlskog invariant [51],  $L$  the neutrino baseline, i.e. the distance between the neutrino production and detection points, and  $\Delta_{ab}$  a factor proportional to the sign and magnitude of the mass splitting. From these equations, it is clear how the relative large value of  $\theta_{13}$  is a happy accident necessary not to completely suppress the sensitivity to CP violation. The equations also show how the sensitivity to  $\delta$  is tied

to the measurement of the least precisely measured mixing angle,  $\theta_{23}$  (via the  $\sin 2\theta_{23}$  term) and to an other unknown quantity, the neutrino “mass hierarchy” (via the  $\Delta_{ab}$  terms). The precise determination of  $\theta_{23}$  is often referred as to “the octant problem”. Current experimental results [2, 6] are consistent with  $\theta_{23} = 45^\circ$ , which would imply maximal mixing between  $\nu_\mu - \nu_\tau$ , hinting to an intriguing new symmetry. Therefore, a precise measurement of  $\theta_{23}$  is of great interest for theoretical models of quark-lepton universality [47, 59, 66], whose quark and lepton mixing matrices are proportional to the deviation of  $\theta_{23}$  from  $45^\circ$ .

**Neutrino mass hierarchy.** The “mass hierarchy” problem refers to the unknown ordering of the value of absolute mass of the neutrino mass eigenstates. Current oscillation experiments are sensitive only to the magnitude of the mass splitting, and not directly to its sign. In a framework where the lightest neutrino mass (arbitrarily) corresponds to the first eigenstate  $m_1$ , it is unknown whether  $m_2 - m_1 < m_3 - m_1$  (Normal Hierarchy) or  $m_2 - m_1 > m_3 - m_1$  (Inverted Hierarchy). The mass hierarchy affects not only the sensitivity to CP violation searches in long baseline oscillation experiments, but also the sensitivity to determine whether neutrinos are Majorana particles in neutrinoless double beta decay experiments.

**Majorana or Dirac?** Evidence of neutrino oscillations demands the introduction of a mechanism which can give mass to the neutrinos. This mechanism should possibly also explain why neutrino masses are at least six orders of magnitude lower than the electron mass (the second lightest SM fermion). In a description of neutrinos as Dirac 4-component spinors, the neutrino field acquires mass via the Higgs mechanism as any other fermion of the SM. In this case, the neutrino mass is given by  $m_a = \frac{y_a^\nu v}{\sqrt{2}}$ , where  $v$  is the Higgs VEV and  $y_a^\nu$  is the Yukawa coupling between the Higgs and the neutrino. The smallness of neutrino masses can only be pinned on a tiny Yukawa coupling which is not justified by the theory.

In 1937, Majorana demonstrated that the introduction of a two components spinor is

sufficient to describe a massive fermion [58]. The Dirac equations of motion for the chiral fields (equations 1.5 and 1.6) hold true in the case of two components spinor under the assumption that the chiral components  $\psi_R$  and  $\psi_L$  are correlated through the charge conjugation matrix  $\mathcal{C}$ ,  $\psi_R = \mathcal{C}\bar{\psi}_L$ . Therefore the theory is applicable only to neutral fermions. Neutrinos are the only neutral elementary particles in the SM – the only possible Majorana particle candidate. This theory constructs a neutrino Majorana mass term  $\mathcal{L}_5$  of the following form in the Higgs unitary gauge

$$\mathcal{L}_5 = \frac{1}{2} \frac{gv^2}{\mathcal{M}} \nu_L^T \mathcal{C}^\dagger \nu_L, \quad (1.12)$$

where  $g$  is the coupling coefficient,  $v$  the Higgs VEV and  $\mathcal{M}$  a constant with the dimension of the mass proportional to the scale of new physics. The  $\mathcal{L}_5$  term would introduce a non-renormalizable term in the lagrangian, since it has dimensions of energy to the fifth power. This is not allowed in the SM lagrangian; however, the existence of such terms is plausible if we consider the SM as an effective theory at low energy, manifestation of the symmetry breaking of a more general theory at higher energy, e.g. a Grand Unified Theory (GUT), and not the definitive theory. The mass term in eq 1.12 implies the neutrino mass to be  $m = \frac{gv^2}{\mathcal{M}}$ . The coupling coefficient can be of the order of any other fermion's coupling coefficient, since the smallness of neutrino masses is achieved by the big value of the new physics mass scale alone. This vanilla formulation is the conceptual basis for many flavors of *see-saw mechanism* [78], which we will not discuss here in any detail. However, it is fascinating how the puzzle of the neutrino mass hints to the existence of a deeper and more complete theory.

From a kinematic point of view, Dirac and Majorana neutrinos satisfy the same energy-momentum dispersion relationship. Thus, it is impossible to discern the neutrino nature through kinematic effects such as neutrino oscillations. Neutrinoless

double beta decay searches are the most promising way to understand the nature of the neutrino and are therefore subject of great theoretical and experimental interest. Observation of the lepton number violating process  $0\nu\beta\beta$  would imply neutrinos have a Majorana component. Depending on the mass hierarchy, the theory also predicts  $0\nu\beta\beta$  exclusion regions and confirmation of the sole Dirac component for neutrinos [23].

### 1.3.2 Towards a more fundamental theory: GUTs

Despite its highly predictive power, a number of conceptual issues arise in the SM which disfavor it to be a good candidate for a fundamental theory.

The SM does not include a suitable dark matter candidate and a mechanisms that accounts for the baryon asymmetry of the universe. Additionally, up to a total of 25 parameters remain seemingly arbitrary and need to be fitted to data: 3 gauge couplings, 9 charged fermion masses, 3 mixing angles and one CP phase in the CKM matrix, the Higgs mass and quartic coupling,  $\theta_{QCD}$ , 3 neutrino mixing angles, 1 Dirac phase and, eventually, 2 Majorana phases.

From a group theory perspective, the SM has a rather complex group structure, where a gauge group is formed with the direct product of other three groups as shown in eq. 1.1. Drawing a parallel with the electroweak symmetry breaking mechanism, where the  $SU(2)_T \otimes U(1)_Y$  is recovered from  $U(1)_{EM}$ , an interesting line of simplification for the SM group structure would be to devise a similar mechanism where  $SU(3)_C \otimes SU(2)_T \otimes U(1)_Y$  is recovered from an hypothetical larger group. IS THIS CORRECT? Just as the electroweak unification becomes evident at energies higher than the Higgs VEV, a direct manifestation of Grand Unification Theories (GUTs) would occur at even higher energies.

As the smallness of neutrino masses suggests the existence of a higher mass scale,

an other, even stronger, hint to Grand Unification comes from the slope of running of the coupling constants. The coupling constants for the electromagnetic, weak and strong interactions in the SM vary as a function of the interaction energy as shown in figure 1.2; they do not exactly meet under the current experimental constraints, but their trend is interesting enough to push for the construction of theories where perfect unification is achieved through the addition of new particles.

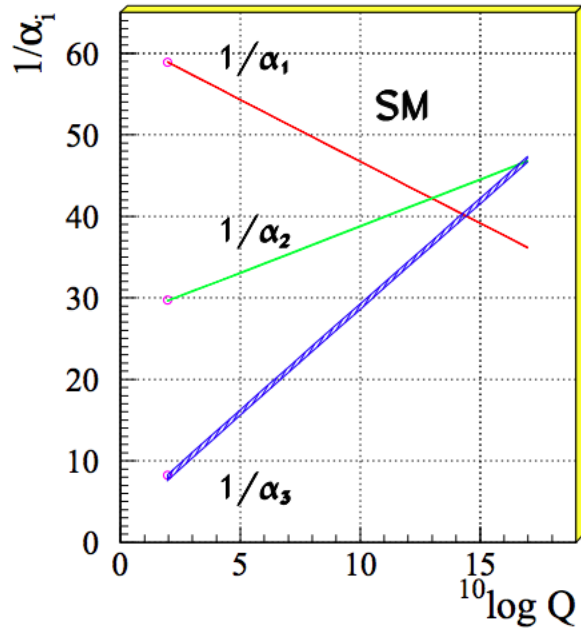


Figure 1.2: Evolution of the inverse of the three coupling constants in the Standard Model as a function of the momentum transferred, [54].

**SU(5).** The smallest simple group containing  $SU(3)_C \otimes SU(2)_T \otimes U(1)_Y$  is SU(5), as shown first by Georgi and Glashow in [42]. Quarks and leptons in this group fit the  $\bar{5}$  and 10 representations. The representation for left-handed fermions are the following

$$\bar{5} = (\nu_e, e^-)_L + \bar{d}_L \quad (1.13)$$

$$10 = e_L^+ + \bar{u}_L + (u, d)_L, \quad (1.14)$$

while the boson structure gains a new couple of super heavy bosons (X,Y)

$$24 = \underbrace{(8, 1)}_{\text{gluons}} + \underbrace{(1, 3) + (1, 1)}_{W^\pm, Z, \gamma} \dots + \underbrace{(3, 2) + (\bar{3}, 2)}_{X, Y \text{ bosons}}. \quad (1.15)$$

Nice features such as charge quantization and the identity between the positron and proton charge value come directly from the group structure. The new super heavy bosons are colored and form a weak doublet. Their are the mediator of the interaction that turns quarks into leptons, leading to predict the existence of processes that violate baryon number, such as  $p \rightarrow \pi^0 + e^+$  (see fig 1.8, right). The prediction for proton decay lifetime,  $\tau_p \sim \frac{M_X^4}{m_p^5} \sim 10^{30 \pm 1.5}$  years, is unfortunately experimentally disproved by IMB and Super-K [?].

**SO(10).** More complicated group structures, such as SO(10) are still viable candidates for GUT. SO(10) includes the same type of  $X$  and  $Y$  bosons as SU(5). Right-handed massive neutrinos are embedded in the construction of the irreducible representation of SO(10). Different patterns of SO(10) symmetry breaking to recover the SM are possible and lead to different predictions for the proton decay lifetime; some of these predictions are not excluded by the experiments [55].

**SUSY GUTs.** Supersymmetry theories allow for another family of GUTs [?]. In SUSY, every fundamental particle in the SM has a “superpartner”, identical in each quantum number except for the spin-statistics: the fermion supersymmetric partners are bosons and vice versa. Collider experiments (mainly LHC) constrain the mass of the supersymmetric partners to be very heavy [?]. The SU(5), SU(10) groups with a SUSY twist are the basic groups for SUSY GUTs. From the phenomenology point of view, SUSY models tend to push the proton decay life time higher by a factor of four, they solve the “hierarchy problem”, and they also predict new channels for the proton decay. In particular they predict the presence of kaons in the final product, with a dominant mode of  $p \rightarrow \bar{\nu} K^+$ . Predictions on the proton decay lifetime depend

on the chosen SUSY model; again, some of the predictions are not excluded by the experiments [56, 57, 69].

## 1.4 Motivations for Hadronic Cross Sections in Argon

Critical challenges await the next decade of experimental physics at the intensity frontier. Following the recommendation of the latest Particle Physics Project Prioritization Panel [67], the US is dedicating substantial resources to the development of a short- and long- baseline neutrino program to address many of open questions in neutrino physics today. This program pivots on the Liquid Argon Time Projection Chamber (LArTPC) detector technology which will be described in Chapter 2.

The main goals of these research programs include:

- the assessment of the existence of right-handed sterile neutrinos via the study of accelerator neutrinos on a short baseline (SBN),
- the determination of the sign of  $\Delta m_{13}^2$  (or  $\Delta m_{23}^2$ ), i.e., the neutrino mass hierarchy via the study of accelerator neutrinos on a long baseline (DUNE),
- the determination of the octant, i.e. whether  $\theta_{23}$  is maximal, via the study of accelerator neutrinos on a long baseline (DUNE),
- the determination the status of CP symmetry in the lepton sector, via the study of accelerator neutrinos on a long baseline (DUNE),
- the search for observables predicted by GUTs, such as proton decay via the study of non accelerator physics in massive underground detectors (DUNE).

### 1.4.1 Pion-Argon Total Hadronic Cross Section

This section outlines the importance of the pion-argon total hadronic cross section in the context of the current and upcoming liquid argon neutrino experiments, SBN and DUNE. We describe the signal signature and historical measurements of pion-nucleus cross section, as well as the implementation of this cross sections in the current version of the simulation package used by LArIAT.

#### $\pi^-$ Ar Cross Section in the Context of Neutrino Searches

As outlined in 1.2.3, neutrino experiments use the products of neutrino interactions to identify the energy and flavor of the incoming neutrino. Pions are a common product of neutrino interaction, especially in resonant scattering, DIS and coherent pion production. For neutrino experiments in argon, there are two main reasons why understanding pion hadronic interactions with argon is important: to model the behavior of the pion inside the nucleus struck by the neutrino and to model the behavior of the pion during its propagation inside the detector medium.

Assumptions on the nuclear models and on the interaction of hadrons inside the nucleus performed at the level of the neutrino event generator bridge the measurement of the products of a neutrino interaction to the reconstruction of the neutrino energy and flavor. Thus, understanding pion hadronic interactions with the nucleus is particularly important to model correctly resonant, DIS and coherent pion production in neutrino interactions, where the presence of pions in the nucleus is abundant. For example, in case of resonant scattering,

$$\nu_l + N \rightarrow l + \Delta/N^* \rightarrow l + \pi + N', \quad (1.16)$$

the  $\Delta$  and  $N^*$  and excited states will decay hadronically in matters of  $\sim 10^{-24}$  s inside the nucleus producing pions which will bounce within the nuclear medium. The decay

modes for the lower mass  $\Delta$  (1232) and  $N^*(1440)$  are listed in table 1.3.

We illustrate here the basis of the GENIE Neutrino Generator [10], since it is one the most popular event generators for LAr experiments.

The key elements of a neutrino event generators for resonance and DIS events are the nuclear model and the hadron treatment (both production and transportation). We illustrate here the conceptual basis of the GENIE Neutrino Generator [10] as an example, since GENIE is one the most popular event generators for LAr experiments. For example, the nuclear model used by GENIE for all processes is a relativistic Fermi gas (RFG) modified to incorporate short range nucleon-nucleon correlations [16]. This means that the initial momentum and binding energy of the struck nucleon is determined by assuming nucleons inside the nucleus are quasi-free, acting independently in the mean field of the nucleus. For  $A > 20$  like argon, the 2-parameter Woods-Saxon shell model for density function is used. The GENIE module INTRANUKE [53] is used to simulate the final-state interactions (FSI) which is the hadron re-interaction inside the nucleus. This module places the outgoing particles in the nucleus and propagates them using the “hA model”. In the INTRANUKE hA model, hadrons can undergo at most one FSI per event. When possible, external hadron-nucleus scattering data are used to tune INTRANUKE. Since no data is available for Argon, GENIE uses an interpolation of data from heavier and lighter nuclei for the pion-argon cross section leading to big uncertainties in the INTRANUKE module.

Once the pion has left the target nucleus, the pion-argon hadronic cross section plays an important role in the pion transportation inside the argon medium: processes like pion absorption with emission of nucleons or pion charge exchange can greatly modify the topology of a neutrino interactions in the detector and lead to errors in the event classification. Being able to reconstruct the details of pions inside the detector is an imperative for modern liquid argon neutrino experiment to achieve the design resolution for their key physics measurements.

## $\pi^-$ -Ar Hadronic Interaction: Signal Signatures

Strong hadronic interaction models [27, 43] predict the pion interaction processes with argon in the [100 - 1200] MeV energy range. The total hadronic  $\pi^-$ -Ar interaction cross section is defined as the one related to the single process driven only by the strong interaction which is dominant in the considered energy range. In measuring the “total” cross section, we include both the elastic and reaction channels, regardless of the final state,

$$\sigma_{Tot} = \sigma_{Elastic} + \sigma_{Reaction}; \quad (1.17)$$

the reaction channel is further characterized by several exclusive channels with defined topologies,

$$\sigma_{Reaction} = \sigma_{Inelastic} + \sigma_{abs} + \sigma_{chex} + \sigma_{\pi prod}. \quad (1.18)$$

A summary of the pion final states in order of pion multiplicity is given in table 1.4. Pion capture and pion decay at rest dominate the cross section under 100 MeV. We define pion capture as the process determining the formation of a pionic atom and the subsequent pion’s end of life. Stopping negative pions can form pionic argon, where the negative pion plays the role of an orbital electron. Since the pion mass is two orders of magnitude greater than the electron mass, the spatial wave form of the pion will overlap way more with the nucleus compared to the electron case. After the electromagnetic formation of the pionic atom, the pion will quickly be absorbed by the nucleus, which is put in an excited state. The nucleus then de-excites with the emission of low energy nucleons and photons. Pion capture is predominant compared to pion decay, the other important process for very low energy pions. The decay of a pion is governed by the weak force; the pion decay life time is  $\tau_\pi = 2.6 \times 10^{-8}$  s and the main decay mode is  $\pi^- \rightarrow \mu^- + \bar{\nu}_\mu$  (BR 99.98%). Since pion capture can be considered an electromagnetic process and pion decay is a weak process, this energy region is purposely excluded from the hadronic cross section measurement.

## Previous measurements: Lighter and Heavier Nuclei

Many experiments with pion beams have studied the hadronic interaction of pions on light and heavy materials, such as He, Li, C, Fe, Pb [18]. However, data on argon are rare: the total differential hadronic cross section has never been measured before on argon. Simulation packages like Geant4 base their pion transportation for argon on data from lighter and heavier nuclei: the goal of LArIAT’s dedicated measurement on argon is to bridge this gap in data, thus reducing the uncertainties related to pions interaction in argon in both neutrino event generators and in simulation packages of pion transportation.

The shape of the pion-nucleus interaction cross section in the energy range considered shows the distinct features that indicate the presence of a resonance. In fact, the mean free path of a pion of kinetic energy between 100 and 400 MeV is much shorter than the average distance between nucleons (which is of the order of 1 fm). Therefore, the pion interacts with surface nucleons. A  $\Delta$  resonance is often produced in the interaction, which subsequently decays inside the nucleus. Experimental results on several nuclei as reported in [18] are shown in Figure 1.3; it is interesting to notice here how the shape of the  $\Delta$  resonance become less pronounced as a function of the mass number of the target nucleus. Pion interactions with heavier nuclei also shift the peak of the resonance at lower energy; this effect is due to kinematic considerations and to the difference in propagation of the  $\Delta$  inside the nucleus. Multiple scattering effect modify the resonance width, which is larger than the natural-decay width. As an example of a fairly well studied target, Figure 1.4 reports the negative pion cross section on Carbon for the elastic and reaction<sup>2</sup> channels, and their sum [33].

---

2. This paper calls “inelastic interaction” what we refer as to “reaction channel”.

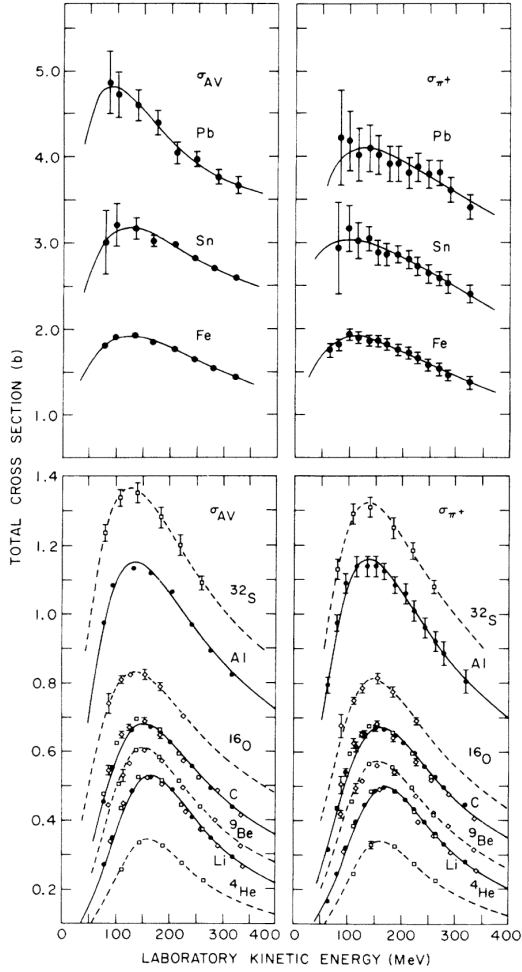


Figure 1.3: Pion-nucleus total cross sections:  $\sigma_{\pi^+}$  for positive pions (right) and  $\sigma_{AV}$  (left) for the average between positive and negative pions  $\sigma_{AV} = \frac{\sigma_{\pi^+} + \sigma_{\pi^-}}{2}$  in the  $\Delta$  resonance region. The error bars include estimates of systematic uncertainties. The curves are the results of fits to the data assuming a Breit-Wigner shape. This summary plot is reported in [18] and uses data from [30, 74].

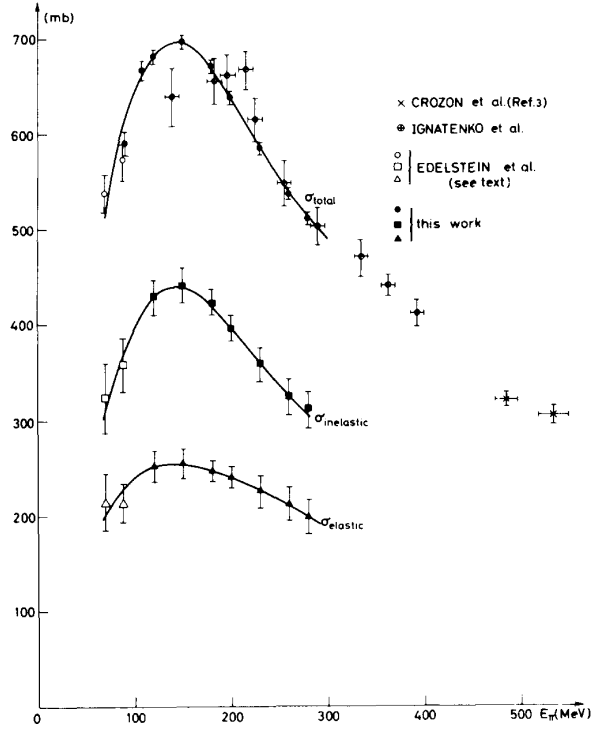


Figure 1.4: Negative pion nucleus total, elastic and reaction cross sections on  $^{12}\text{C}$  as from [33].

### Negative Pion Interaction Cross Section in Simulation Packages

LArIAT uses Geant4 as the default simulation package. In particular, pions (and kaons) transportation is achieved through the Geant4 FTFP\_BERT physics list. In this physics list, Geant4 uses the Bertini cascade model [75] to simulate the products of the pion-nucleus interaction as well as the secondary hadrons re-interactions inside the target nucleus (intra-nuclear cascade). The target nucleus is represented as a continuous gas where the nuclear potential follows concentrical shells whose depths approximate the Woods-Saxon shape. The CERN-HERA compilations [71, 72] of hadron-nucleon interaction data is the data base used for the decision making process after the cascade is invoked. The cross section model determines if the pion interacts, the eventual type of interaction and the interaction multiplicity. For hadron projectiles with energy less than 20 GeV, Geant4 reports the uncertainty on the cross

section model to be about the size of the error bars on the data used, or about 10%, increasing to 20-30% in energy regions where data is sparse.

The relevance of the GENIE generator for neutrino physics and its basic working principles have been outlined earlier in this section. Given GENIE’s modularity, information on hadron-nucleus interactions can be extracted from the INTRANUKE module and directly compared against the Geant4 predictions.

The work in [62] reviews the current status of negative and positive pion simulation in Geant4 and GENIE for  $^{12}\text{C}$ ,  $^{56}\text{Fe}$ , and  $^{40}\text{Ca}$ . From that work, we report the results for  $^{12}\text{C}$  in Figure 1.5 as it allows a direct comparison between Geant4, GENIE and data. Geant4 predictions for  $\pi^-$  on Carbon are in good agreement with data over all the spectrum, while GENIE predictions seem to show some features at around 500 MeV and 900 MeV, maybe due to higher resonances in the hA model. From the same work, we also report the negative pion cross section on  $^{40}\text{Ca}$  in Figure 1.6, since this is the nuclear medium closest to argon with some available data. The predictions from both Geant4 and GENIE agree with data in the high energy region. The predictions diverge in the resonance region, where data is not available.

For the  $\pi^-$  argon total cross section measurement, we use the Geant4 Bertini Cascade model, whose predictions for the total, elastic and reaction cross sections are shown in Figure 1.7.

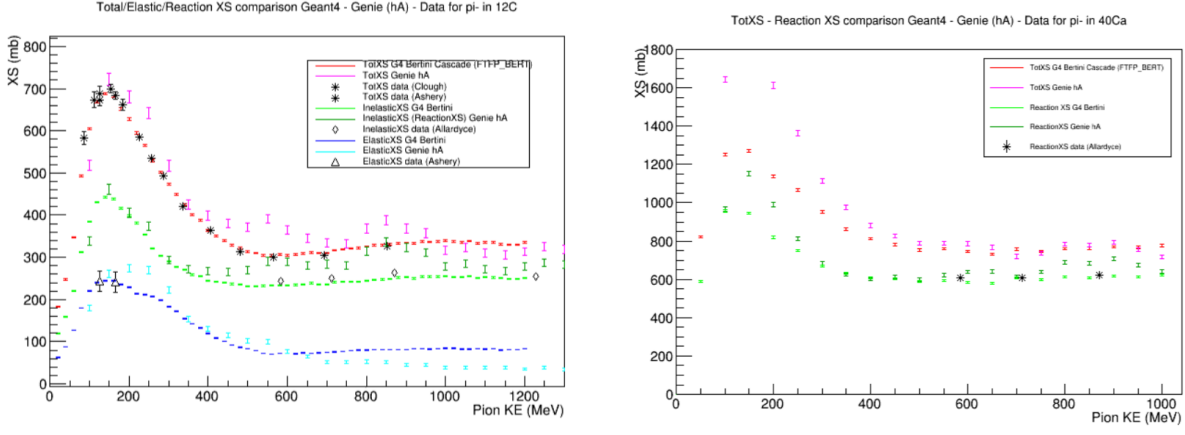


Figure 1.5: Total, elastic and reaction cross section for  $\pi^-$  on  $^{12}\text{C}$ . Comparison between results from Geant4 simulation (Bertini cascade model), Genie simulation (hA model), and experimental data [12, 30, 31, 68].

Figure 1.6: Total, elastic and reaction cross section for  $\pi^-$  on  $^{40}\text{Ca}$ . Comparison between results from Geant4 simulation (Bertini cascade model), Genie simulation (hA model), and experimental data [31].

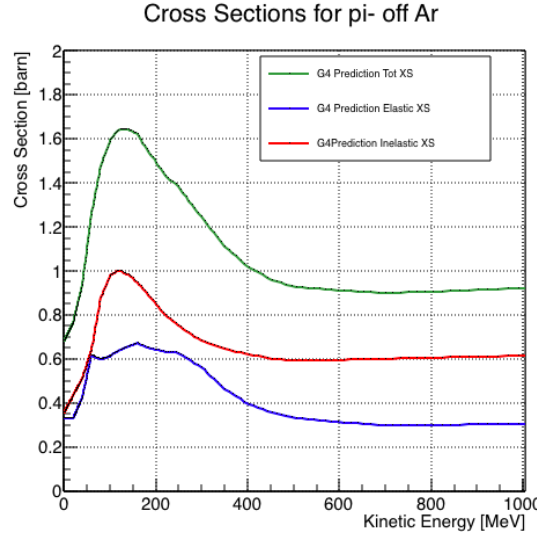


Figure 1.7: Total, elastic and reaction hadronic cross section for  $\pi^-$ -argon implemented in Geant4 10.01.p3.

Resonance	Decay Mode	Lifetime (s)
$\Delta$ (1232) $3/2^+$	$\Delta^{++}(\text{uuu}) \rightarrow p\pi^+$ $\Delta^+(\text{uud}) \rightarrow n\pi^+$ $\Delta^+(\text{uud}) \rightarrow p\pi^0$ $\Delta^0(\text{udd}) \rightarrow n\pi^0$ $\Delta^0(\text{udd}) \rightarrow p\pi^-$ $\Delta^-(\text{ddd}) \rightarrow n\pi^-$	$\sim 5.6 \times 10^{-24}$
$N^*$ (1440) $1/2^+$	$N^* \rightarrow N\pi$ $N^* \rightarrow N\pi\pi$	$\sim 2.2 \times 10^{-24}$

Table 1.3: Main decay modes of the lightest Delta resonance and Nucleon excited state.

N $\pi$ in FS	Channel Name	Reaction	Notes
0	Pion Absorption, $\sigma_{abs}$	$\pi^-(np) \rightarrow nn$ (2-body abs) $\pi^-(nnp) \rightarrow nnn$ (3-body abs) $\pi^-(npp) \rightarrow pnn$ (3-body abs) $\pi^-(nnpn) \rightarrow pnn$ (Multi-body abs)	Suppressed on single nucleon by energy conservation: the process occurs on at least two nucleons system.
1	Elastic Scattering, $\sigma_{el}$	$\pi^- + N \rightarrow \pi^- + N$	Scattering on nucleon or nucleus, the target is left in ground state
1	Charge Exchange, $\sigma_{chex}$	$\pi^- + p \rightarrow \Delta^0 \rightarrow \pi^0 + n$ $\pi^- + N \rightarrow \pi^+ + \text{nucleons}$	Single charge exchange: charged pion converts into neutral pion Double charge exchange: charged pion converts into opposite charge pion
1	Inelastic Scattering, $\sigma_{inel}$	$\pi^- + p \rightarrow \Delta^0 \rightarrow \pi^- + p$ (knock-out) $\pi^- + n \rightarrow \Delta^- \rightarrow \pi^- + n$ (knock-out)	Other possible reactions: Pure Inelastic scattering: population of low energy bound excited states Nuclear break-up with nucleons or fragments knock-out
2+	Pion Production, $\sigma_{\pi prod}$	$\pi^- + N \rightarrow \geq 2\pi + \text{nucleons}$	Possible if pion K.E $\geq 500$ Mev/c

Table 1.4: Summary of negative pion hadronic interactions as a function of the pion multiplicity in the final state in the energy range [100-1200] MeV.

## 1.4.2 Kaon-Argon Total Hadronic Cross Section

This section outlines the importance of the kaon-argon total hadronic cross section. We start by discussing the measurement in the context of nucleon decay searches. We then describe the signal signature and historical measurements of kaon-nucleus cross section, as well as the implementation of this cross sections in the current version of the simulation package used by LArIAT.

### K<sup>+</sup>Ar Cross section in the Context of Nucleon Decay Searches

#### Nucleon decay

Baryon number is accidentally conserved in the Standard Model. Even though no baryon number violation has been experimentally observed thus far, no underlying symmetry in line with the Noether paradigm [61] explains its conservation. As shown in section 1.3.2, almost all Grand Unified Theories predict at some level baryon number violation in the form of nucleon decay on long time-scales. Given the impossibility to reach grand unification energy scales with collider experiments (Energy Scale  $> 10^{15}$  GeV), an indirect proof of GUTs is needed. The experimental observation of nucleon decay may be the only viable way to explore these theories.

In case of nucleon decay discovery, the dominant decay mode may uncover additional information about the GUT type. Supersymmetric GUTs [14, 24] prefer the presence of kaons in the products of the decay, e.g.  $p \rightarrow K^+ \bar{\nu}$  (see fig 1.8, left). Gauge mediated GUTs, in which new gauge bosons are introduced that allow for the transformation of quarks into leptons, and vice versa, prefer the mode  $p \rightarrow e^+ \pi^0$  (see fig 1.8, right).

LArIAT tiny active volume makes it impossible for the experiment to place competitive limits on nucleon decay searches. However, LArIAT provides excellent data to characterize kaons in liquid argon for the “LAr golden mode”,  $p \rightarrow K^+ \bar{\nu}$ . The

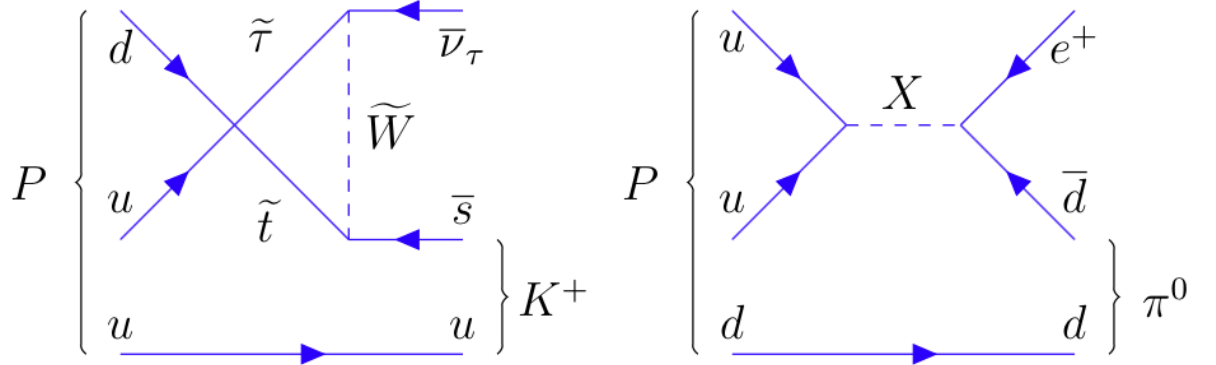


Figure 1.8: Feynman diagrams for proton decay “golden modes”:  $p \rightarrow K^+\bar{\nu}$  for supersymmetric GUTs on the left and  $p \rightarrow e^+\pi^0$  for gauge-mediated GUTs on the right.

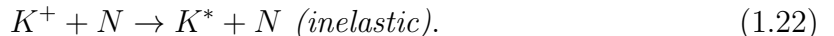
result of these studies will affect future proton decay searches in LArTPCs. Previous work has been done to assess the potential identification efficiency for different decay modes in a LArTPC [29], but, as the time of this writing, no study of kaon selection efficiency in LArTPCs has been performed on data. The  $K^+$ -Ar interaction cross section has never been measured before and can affect the possibility of detecting and measuring kaons when produced in a proton decay event. Kaon interactions with argon can distort the kaon energy spectrum as well as change the topology of single kaon events. In a LArTPC, non-interacting kaons appear as straight tracks with a high ionization depositions at the end (Bragg peak). The topology of interacting kaons can be quite different. In case of elastic scattering, a distinct kink will be present in the track. In case of inelastic scattering the Bragg peak will not be present and additional tracks will populate the event. Performing the total hadronic  $K^+$ -Ar cross section measurement on data serves the double purpose of identifying the rate of “unusual” topologies (kinks and additional tracks) and of developing tools for kaon tracking in LAr.

## **K<sup>+</sup>Ar Hadronic Interaction: Signal Signatures**

The interaction of a mildly relativistic charged kaon with an argon nucleus is determined largely by the strong force. The total hadronic K<sup>+</sup>-Ar interaction cross section is defined as the one related to the single (hadronic) process driven only by the strong interaction. In this case, “total” indicates all strong interactions regardless of the final state. This condition purposefully includes both elastic and inelastic (reaction) channels. Indeed, the total cross section section can be then decomposed into

$$\sigma_{Tot} = \sigma_{Elastic} + \sigma_{Reaction}.$$

For the LArIAT cross section analysis, the kaons considered span a momentum inside the TPC from 100 MeV/c to 800 MeV/c. In this energy range, the relevant K-Nucleon interactions are according to [38]:



## **Previous Measurements: Lighter and Heavier Nuclei**

In general, measurements on kaon cross sections are extremely scarce. The measurement of the kaon interaction cross section would bring the additional benefit of reducing the uncertainties associated with hadron interaction models adopted in MC simulations for argon targets, beneficial for both proton decay studies and kaon production from neutrino interaction studies, where the uncertainties for final state interaction models are big [25].

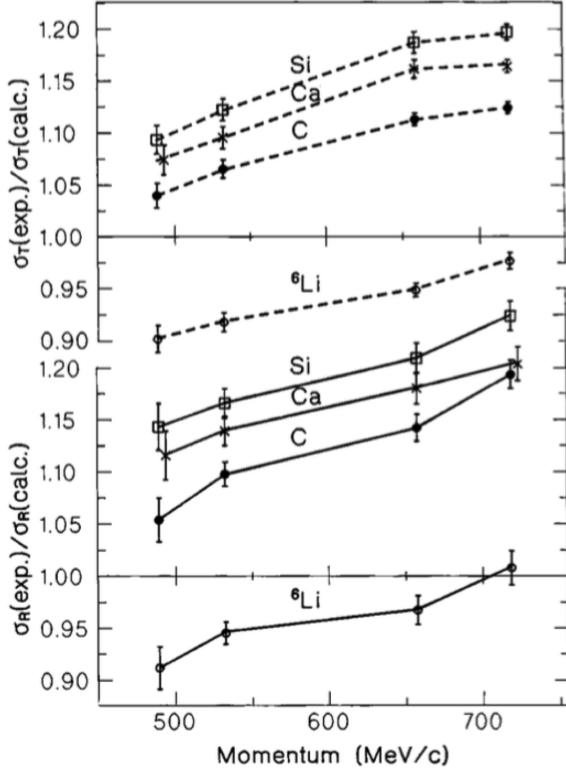


Figure 1.9: Ratios between experimental and calculated cross sections as from [40]. Top: Total cross sections. Bottom: reaction cross sections.

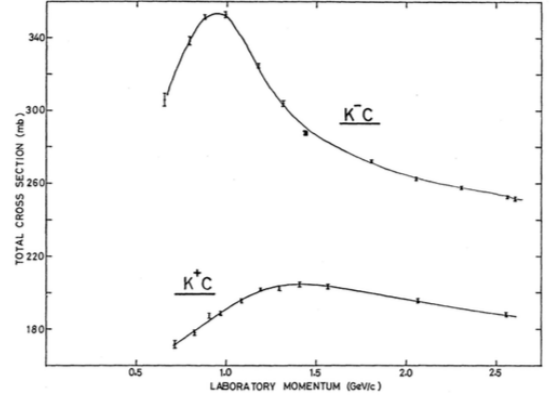


Figure 1.10: Total  $K^+$  and  $K^-$  cross sections on carbon as from [17].

Figure 1.9 shows a 1997 measurement on several elements as performed by Friedmann et al. [40]. As a reference, this paper measures a  $\sigma_{Tot}$  for Si of  $366.5 \pm 4.8$  mb and a  $\sigma_{Tot}$  for Ca of  $494.6 \pm 7.7$  mb at 488 MeV/c. The cross section for argon is expected to lie in between these two measurements. Additional data on the kaon cross section are provided by Bugg et al. [17]. Bugg performs a measurement of the total  $K^+$  and  $K^-$  cross sections on protons and deuterons over the range of 0.6-2.65 GeV/c, as well as a measurement of the total  $K^+$  and  $K^-$  cross sections on carbon for a number of momenta; the results of this paper on carbon are reported in Figure 1.10.

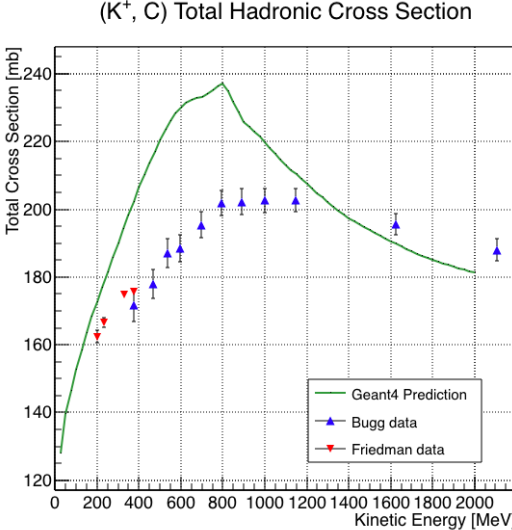


Figure 1.11: Total hadronic cross section for carbon implemented in Geant4 10.01.p3 with overlaid with the Bugg and Friedman data.

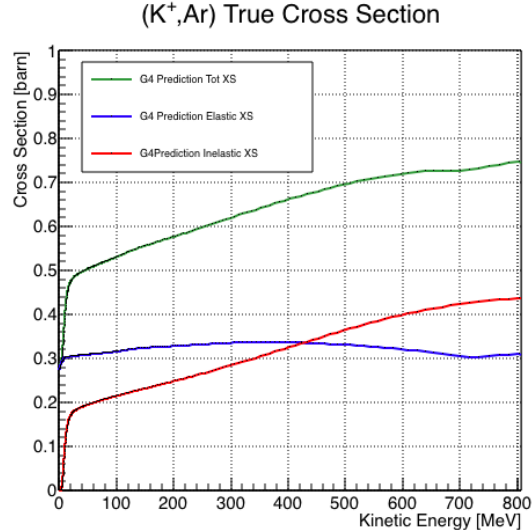


Figure 1.12: Total, elastic and reaction hadronic cross section for  $K^+$ -argon implemented in Geant4 10.01.p3.

### Kaon Interaction Cross Section for thin target in Geant4

Since the kaon cross section in argon has never been measured before, simulation packages tune kaon transportation in argon by extrapolation from lighter and heavier nuclei. LArIAT uses the Geant4 suite for particle transportation. Since kaon data on carbon are available, we used it as a metric to evaluate the Geant4 prediction performances. Figure 1.11 shows the total hadronic cross section for carbon implemented in Geant4 10.01.p3 overlaid with the Bugg and Friedman data. Unfortunately, the current version of Geant4 does not reproduce the data for carbon closely. On one hand, this evidence makes us even more wary when using the Monte Carlo in simulating the kaon-argon interactions. On the other, it further highlights the importance of the kaon measurement. Figure 1.12 shows the Geant4 prediction for the total, elastic and reaction cross section for  $K^+$  on argon.

# Chapter 2

## Liquid Argon Detectors at the Intensity Frontier

In the next few years, LArTPCs will be the tools to answer some of the burning questions in neutrino physics today. This section illustrates the operational principles of this detector technology, as well as the scope of the key detectors in the US liquid argon program – SBN, DUNE and LArIAT.

### 2.1 The Liquid Argon Time Projection Chamber Technology

#### 2.1.1 TPCs, Neutrinos & Argon

David Nygren designed the first Time Projection Chamber (TPC) in the late 1970s [15] for the PEP-4 experiment, a detector apt to study electron-positron collisions at the PEP storage ring at the SLAC National Accelerator Laboratory. From the original design in the seventies – a cylindrical chamber filled with methane gas – the TPC detector concept has seen many incarnations, the employment of several different active media and a variety of different particle physics applications, including, but

not limited to the study of electron/positron storage rings (e.g. PEP4, TOPAZ, ALEPH and DELPHI), heavy ions collisions in fixed target and collider experiments (e.g. EOS/HISSL and ALICE ), dark matter (ArDM), rare decays and capture (e.g. TRIUMF, MuCap), neutrino detectors and nucleon decay (ICARUS, SBN, DUNE), and neutrino less double beta decay (Next). A nice review of the history of TPCs and working principles is provided in [50].

Several features of the TPC technology make these detectors a more versatile tool compared to other ionization detectors and explain such a wide popularity. TPCs are the only electronically read detector which deliver simultaneous three-dimensional track information and a measurement of the particle energy loss. Leveraging on both tracking and calorimetry, particle identification (PID) capabilities are enhanced over a wide momentum range.

Carlo Rubbia first proposed the use of a Liquid Argon TPC for a neutrino experiment, ICARUS [14], in 1977. The active medium in ionization detector has historically been in the gaseous form. Nevertheless, using nobles elements in the liquid form for neutrino detectors is advantageous for several reasons. The density of liquids is  $\sim$ 1000 times greater than gases, increasing the number of target centers for neutrino's interaction in the same volume. Since the energy loss of charged particle is proportional to the target material density, as shown in the Bethe-Block equation in 2.1, the increased density reflects into a proportionally higher energy loss, enhancing the calorimetry capability of detectors with a liquid active medium. Additionally, the ionization energy of liquids is smaller than gasses by the order of tens of eV. Thus, at the passage of charged particles, liquid generally produce more ionization electrons than gas for the same deposited energy and force the particles to deposit more energy in a shorter range. The downside of using noble liquid gasses in experiments is that they require a cryogenic system to cool the gas until it transitions to its the liquid form. The properties of liquid argon in comparison liquid xenon – a popular choice

Element	LAr	LXe
Atomic Number	18	54
Atomic weight A	40	131
Boiling Point Tb at 1 atm	87.3 K	165.0 K
Density	1.4 g/cm <sup>3</sup>	3.0 g/cm <sup>3</sup>
Radiation length	14.0 cm	2.8 cm
Moliere Radius	10.0 cm	5.7 cm
Work function	23.6 eV	15.6 eV
Electron Mobility at $E_{field} = 10^4$ V/m	0.047 m <sup>2</sup> /Vs	0.22 m <sup>2</sup> /Vs
Average dE/dx MIP	2.1 MeV/cm	3.8 MeV/cm
Average Scintillation Light Yield	40000 $\gamma$ /MeV	42000 $\gamma$ /MeV
Scintillation $\lambda$	128 nm	175 nm

Table 2.1: LAr, LXe summary of properties relevant for neutrino detectors.

for dark matter and neutrinoless double beta decay detectors – are summarized in table 2.1. Albeit xenon would be more desirable than argon given some superior properties such as lower ionization energy and higher density and light yield, argon relative abundance abates the cost of argon compared to xenon, making argon a more viable choice for the construction of big neutrino detectors.

LArTPCs are some times referred as to “electronic” bubble-chambers, for the similarity in the tracking and energy resolution which is coupled with an electronic readout of the imaging information in LArTPCs. Compared to these historic detectors however, LArTPC bestow tridimensional tracking and a self triggering mechanism provided by the scintillation light in the noble gas. A comparison between a neutrino interaction in the ArgoNeut LArTPC and in the bubble chamber is shown in picture **EVENT DISPLAY**.

### 2.1.2 LArTPC: Principles of Operation

To the bare bones, a LArTPC is a bulk of liquid argon sandwiched in a flat capacitor, equipped with a light collection system. A uniform electric field of the order of 500 V/cm is maintained constant between the faces of the capacitor. The anode is sensitive to ionization charge and it is usually made of two or more planes segmented

into several hundreds parallel sense wires a few millimeters apart; different geometries for the anode segmentation are under study [26].

Argon ionization and scintillation are the processes leveraged to detect particles in the LArTPC active volume. When a ionizing radiation traverses the argon active volume it leaves a trail of ionization electrons along its trajectory and it excites the argon, leading to the production of scintillation light – details on the production and detection of ionization charge and scintillation light are provided in 2.1.4 and 2.1.4 respectively. The optical part of the detector collects the argon scintillation light in matters of nanoseconds. This flash of light determines the start time of an event in the chamber,  $t_0$ . The uniform electric field drifts the ionization electrons from the production point towards the anode plane in order of hundreds of microseconds or more depending on the chamber dimensions<sup>1</sup>. The anode sense wires see either an induced current by the drifting charge (on induction planes) or an injection of the ionization charge (collection plane) [94]. An appropriate choice of the voltage bias on each wire plane assures ideal charge transparency, so that all the ionization charge is collected on the collection plane and none on the induction planes [95].

The arrival time of the charge on the anode sense wires is used to measure the position of the original ionizing radiation in the drift direction. In fact, since the constant electric field implies that the drift velocity is also constant in the chamber, the position of the original ionization is simply given by the multiplication of the drift velocity by the drift time, where we define as “drift time” the difference between  $t_0$  and the charge arrival time on the wire planes. The spacial resolution on this dimension is limited by the time resolution of the electronics or by longitudinal diffusion of the electrons. The spatial information on the different wire planes maps a bi-dimensional

---

1. The ionized argon also drifts, but in the opposite directions compared to the electrons. Since the drift time is proportional to the particle mass, the ions drift time is much longer than the electrons'. Ionized argon is collected on the cathode which is not instrumented, so it is not used to infer information about the interactions in the chamber.

projection of the interaction pattern in the plane perpendicular to the drift direction. The spacial resolution on this dimension is limited by the transverse electron diffusion in argon and by the grain of the anode segmentation, i.e. the spacing between the wires in the sense planes [100]. The off-line combination of the 2-D information on the wire planes with the timing information allows for the 3D reconstruction of the event in the chamber.

Since the charge deposited by the ionizing radiation in the chamber is proportional to the deposited energy and the charge collected on the sense plane is a function of the deposited charge, LArTPC allow the measurement of the energy deposit in the active volume. Effects due to the presence of free charge and impurities in the active volume, such as a finite electron lifetime, recombination and space charge, complicate the relationship between deposited and collected charge affecting the measurement of the particle's energy, as described in the next section.

### 2.1.3 Liquid Argon: Ionization Charge

The mean rate of energy loss by moderately relativistic elementary charge particles heavier than electrons in the region  $0.1 < \frac{\beta}{\sqrt{1-\beta^2}} < 1000$  is well described by the modified Bethe-Bloch [?] equation

$$-\frac{dE}{dx} = K z^2 \frac{Z}{A} \varrho \frac{1}{\beta^2} \left[ \frac{1}{2} \ln \frac{2m_e c^2 \beta^2 \gamma^2 T_{max}}{I^2} - \beta^2 - \frac{\delta}{2} \right],$$

where  $K = 0.307075 \text{ MeV g}^{-1} \text{ cm}^2$  is a numerical conversion,  $z$  is the number of unit charge of the ionizing radiation,  $Z$ ,  $A$  and  $\varrho$  are the atomic number, mass number and density of the medium,  $m_e$  is the electron mass,  $\gamma = \frac{\beta}{\sqrt{1-\beta^2}}$  is the Lorentz factor of the ionizing radiation,  $T_{max}$  is the maximum kinetic energy which can be imparted to a free electron in a single collision,  $I$  is the mean excitation energy on eV and  $\delta$  is the density correction. The Bethe-Bloch treats as an uniform and continuous

process the energy loss by an ionizing radiation via quantum-mechanical collisions producing ionization or an excitation in the medium. The density correction terms becomes relevant for incident particle with high energy, where screening effects due to the polarization of the medium by high energy particles occur.

Excitation and ionization of the detector medium occur in similar amounts. Since the ionizing collisions occur randomly, we can parametrize their number  $k$  in a segment of length  $s$  along the track with a Poissonian function

$$P(k) = \frac{s^k}{k!\lambda^k} e^{-s/\lambda}, \quad (2.1)$$

where  $\lambda = 1/N_e\sigma_i$ , with  $N_e$  being the electron density of  $\sigma_i$  the ionization cross-section per electron. About 66% of the ionizing collisions in Argon produce only a single electron/ion pair [50]; in the other cases, the transferred kinetic energy is enough for the primary electron to liberate one or more secondary electrons, which usually stay close to the original pair. Occasionally, electrons can receive enough energy to be ejected with high energy, forming so-called “ $\delta$ -ray”: a detectable ionization short track off the particle trajectory, as shown in figure [ADD figure](#). The average number of  $\delta$ -ray with energy  $E > E_0$  per cm follows the empirical form

$$P(E > E_0) \sim \frac{y}{\beta^2 E_0}, \quad (2.2)$$

where  $y$  is an empirical factor depending on the medium (0.114 for gaseous Ar), and  $\beta$  is  $v/c$ .

## Purity & Electron Life Time

The presence of electronegative contaminants in liquid argon, such as oxygen and water, is particularly pernicious, since these molecules quench the charge produced by the ionizing radiation. Thus, amount of charge per unit of length  $dQ/dx$  collected

on the collection plane depends on the charge’s production point in the detector: a ionization produced close to the cathode will see more impurities along its journey to the collection plane than ionization produced close to the anode, resulting in greater attenuation. As a result, the amount of charge collected on the sense wires as a function of the traveled distance follows an exponential decay trend. The traveled distance is generally measured in terms of drift time and the characteristic time constant of the exponential decay is called electron lifetime  $\tau_e$ . Figure ?? shows the typical life time for LArIAT data [cite technote](#). LArIAT small drift distance (47 cm) allows for a relatively short electron life time. The life time for bigger detectors such as MicroBooNE, whose drift distance is 2.5 m, needs to be of the order of to allow charge collection usable for physics analyses. Energy reconstruction in LArTPC applies a correction for the finite lifetime to calibrate the detector calorimetric response; details for LArIAT are provided in Section ??.

LArTPCs use hermetically sealed and leak-checked vessels to abate the leakage and diffusion of contaminants into the system. The liquid argon filling of the volume occurs after the vessel is evacuated or purged with gaseous argon [205] to reduce remaining gases in the volume. Even so, the construction of a pure tank of argon is unviable, as several sources of impurity remain. In particular, impurities can come from the raw argon supply, the argon filtration system and from the outgassing from internal surfaces. Outgassing is a continuous diffusive process producing contaminants, especially water, even after the vessel is sealed, particularly from materials in the ullage region<sup>2</sup>. Since research-grade argon comes from the industrial distillation of air, the impurities with the highest concentration are nitrogen, oxygen and water, generally maintained under the 1 part per million level by the vendor. Even so, a higher level of purity is necessary to achieve a free electron life time usable in meter

---

2. . While the liquid argon low temperature reduces outgassing in the liquid, this process remains significant for absorptive material (such as plastic) above the surface of the liquid phase

scale detectors. Thus, argon is constantly filtered in the cryogenic system, which reduce the oxygen and water contamination to less than 100 parts per trillion. The filtration system depends on the size and drift distance of the experiment and, for experiments on several meters scale, it includes an argon recirculation system.

## Recombination Effect

After production, ionization electrons thermalize with the surrounding medium and may recombine with nearby ions. Recombination might occur either between the electron and the parent ion through Coulomb attraction (Onsager geminate theory [2] ) or thanks to the collective charge density of electrons and ions from multiple ionizations in a cylindrical volume surrounding the particle trajectory (Jaffe[3] columnar model ). Consideration on the average electron-ion distance and the average ion-ion distance for argon show that the probability of geminate recombination is low; thus recombination in argon is mainly due to collective effects [3]. Since protons, kaons and stopping particles present a higher ionization compared to MIPs, recombination effects are more prominent when considering the reconstruction of energy deposited by these particles.

Models for a theoretical descriptions of recombination base on are provided in (Birks model [6]) and in (Box model [7]). The Birks model assumes a gaussian spatial distribution around the particle trajectory during the entire recombination phase and identical charge mobility for ions and electrons. The Box model also assumes that electron diffusion and ion mobility are negligible in liquid argon during recombination In these models, the fraction of ionization electrons surviving recombination is a function of the number of ion-electron pairs per unit length, the electric field, the average ion-electron separation distance after thermalization and the angle of the particle with respect to the direction of the electric field – plus the diffusion coefficient in the Birks model. Given the stringent assumptions, it is perhaps not surprising

that these models are in accordance to data only in specific regimes: the Birks model is generally used to describe recombination for low  $dE/dx$ , the Box model for high  $dEdX$ . In LArTPC, the ICARUS and ArgoNeut have measured recombination in [8] and [3] respectively. Since LArIAT uses the refurbished ArgoNeut TPC and cryostat, LArIAT currently corrects for recombination using the ArgoNeut measurement, shown in figure [find figure](#).

### Space Charge Effect

Slow-moving positive argon ions created during ionization can build-up in LArTPC, causing the distortion of the electric field within the detector. This effect, called “space charge effect” leads to a displacement in the reconstructed position of the signal ionization electrons. In surface LArTPCs the space charge effect is primarily due to the rate of ionization produced by cosmic rays which is slowly drifting in the chamber at all times. Surface LArTPC of the size of several meters are expected to be modestly impacted from the space charge effect, where charge build-up create anisotropy of the electric field magnitude of the order of 5% at a drift field of 500 V/cm. The smallness of the LArIAT drift volume is such that effect of space charge on the electric field is expected to be even smaller. [CHIEDI A FLAVIO](#)

### 2.1.4 Liquid Argon: Scintillation Light

Liquid argon emits scintillation light at the passage of charged particles. LArTPCs leverage this property to determine when the ionization charge begins to drift towards the anode plane.

#### Scintillation Process

Scintillation light in argon peaks in the ultraviolet at a 128 nm, shown in comparison to Xenon and Krypton in Figure [\[183\]](#). The light yield collected by the optical detector

depends on the argon purity, the electric field, the  $dE/dx$  and particle type, averaging at the tens of thousands of photons per MeV. The de-excitation of Rydberg dimers in the argon is responsible for the scintillation light. Rydberg dimers exist in two states: singlets and a triplets. The time constant for the singlet radiative decay is 6 ns, resulting in a prompt component for the scintillation light. The decay of the triplet is delayed by intersystem crossing, producing a slow component with a time constant of  $\sim 1500$  ns. “Self-trapped exciton luminescence” and “recombination luminescence” are the two processes responsible for the creation of the Rydberg dimers. In the first process, a charged particle excites an argon atom which becomes self-trapped in the surrounding bulk of argon, forming a dimer; the dimer is in the singlet state 65% of the times and in the triplet state 35% of the times. In case of recombination luminescence, the charged particle transfers enough energy to ionize the argon. The argon ion forms a charged argon dimer state, which quickly recombines with the thermalized free electron cloud. Excimer states are produced in the recombination, roughly half in the singlet and half in the triplet state. The light yield dependency on the electric field, on the  $dE/dx$  and particle type derives from the role of free charge in the recombination luminescence process. The spacial separation between the argon ions and the free electron cloud depends on the electric field. On one hand, a strong electric field diminishes the recombination probability, leading to a smaller light yield; on the other, it increases the free charge drifting towards the anode plane. Hence, the amount of measurable charge and light anti-correlates as a function of the electric field. Ionizing particles in the argon modify the local density of both free electrons and ions depending on their  $dE/dx$ . Since the recombination rate is proportional to the square of the local ionization density, highly ionizing particles boost recombination and the subsequent light yield compared to MIPs. The possibility to leverage this dependency for pulshape-based particle identification has been shown in [186], [187].

## Effects Modifying the Light Yield

The production mechanism through emission from bound excimer states implies that argon is transparent to its own scintillation light. In fact, the photons emitted from these metastable states are not energetic enough to re-excite the argon bulk, greatly suppressing absorption mechanisms. In a LArTPC however, several processes modify the light yield in between the location where light is produced and the optical detector. In a hypothetical pure tank of argon, Rayleigh scattering would be the most important processes modifying the light yield. Rayleigh scattering changes the path of light propagation in argon, prolonging the time between light production and detection. The scattering length has been measured to be 66 cm [191] , shorter than the theoretical prediction of  $\sim 90$  cm [190]; this value is short enough to be relevant for the current size of LArTPCs detectors. In fact, Rayleigh scattering worsen the resolution on  $t_0$ , the start time for charge drifting, and alters the light directionality, complicating the matching between light and charge coming from the same object in case of multiple charged particles in the detector.

Traces of impurities in argon such as oxygen, water and nitrogen also affect the light yield, mainly via absorption and quenching mechanisms. Absorption occurs as the interaction of a 128 nm photon directly with the impurity dissolved in the liquid argon. Differently, quenching occurs as the interaction of an argon excimer and an impurity, where the excimer transfers its excitation to the impurity and dissociates non-radiatively. Given this mechanism, it is evident how quenching is both a function of the impurity concentrations and the excimer lifetime. Since the triplet states live much longer than the singlet states, quenching occurs mainly on triplet states, affecting primarily the slow component of the light, reducing the scintillation yield and a shortening of the scintillation time constants.

The stringent constraints for the electron life time limit the presence of oxygen and water to such a low level that both absorption and quenching on these impurity

is not expected to be significant [210]. Contrarily, the nitrogen level is not bound by the electron life time constraints – nitrogen being an inert gas, expensive to filter. Thus, nitrogen is often present at the level provided by the vendor. The effects of nitrogen on argon scintillation light have been studied in the WArP R&D program and at several test stands. The quenching process induced by nitrogen in liquid Ar has been measured to be proportional to the nitrogen concentration, with a rate constant of  $\sim 0.11 \mu s^{-1} \text{ ppm}^{-1}$ ; appreciable decreasing in lifetime and relative amplitude of the slow component have been shown for contamination as high as a few ppm of nitrogen [4]. For a nitrogen concentration of 2 parts per million, typical of the current generation of LArTPC, the attenuation length due to nitrogen has been measured to be  $\sim 30$  meters [52].

### Wavelength Shifting of LAr Scintillation Light

Liquid argon scintillation light is invisible for most optical detectors deployed in LArTPC, such as cryogenic PMTs and SiPMs, since a wavelength of 128 nm is generally too short to be absorbed from most in glasses, polymers and semiconductor materials. Research on prototype SiPMs absorbing directly VUV light and their deployment in noble gasses experiment is ongoing but not mature [77]. Thus, experiments need to shift the wavelength of scintillation light to be able to detect it. Albeit deployed in different ways, neutrinos and dark matter experiments commonly use 1,1,4,4-tetraphenyl-butadiene (TPB) to shift the scintillation light. TPB, whose chemical structure is shown in figure , absorbs the vacuum ultraviolet (VUV) light and emits in the visible at  $\sim 425$  nm [231], with a ratio of visible photon emitted per VUV photon absorbed of  $\sim 1.2:1$  [41].

Neutrino experiments typically coat their optical detector system evaporating a layer of TPB either directly on the PMTs glass surface or on acrylic plates mounted in front of the PMTs [cite microboone](#); this technique allows the fast detection light

coming directly from the neutrino interaction. Dark matter experiments typically evaporate TPB on reflective foils mounted on the inside walls of the sensitive volume and detect the light after it has been reflected; this technique leads to a higher and more uniform light yield, though scattering effects for both the visible and VUV light augment the propagation time and hinder directionality information [some DM detector](#). In order to take advantage of both these techniques, hybrid systems with PMT coating and foils are being considered for the next generation of large neutrino detectors [cite SBND?](#).

### 2.1.5 Signal Processing and Event Reconstruction

In this section we illustrate the processing and reconstruction chain of the TPC signals, from the pulses on the sense wire to the construction of three dimensional objects with associated calorimetry.

**Deconvolution.** Induction and collection planes have different field responses, given the different nature of the signals on these planes: the wires on the induction planes see inductive signal of the drifting charge, while the wires on the collection planes see the current derived from the charge entering the conductor. Thus, signals on the induction plane are bi-polar pulse and signal on the collection plane are unipolar pulses, see Figure [ADD PULSES FIGURE](#). The first step in signal processing is deconvolution, that is a series of off-line algorithms geared towards undoing the detector effects. The result of the deconvolution step is the production of a comparable set waveforms on all planes presenting unipolar, approximately gaussian-like pulses. Signal from all planes are treated on equal footage beyond this point. Some LArTPC apply noise filtering in the frequency domain just after the deconvolution to clean up wire cross talk. Since signals from the LArIAT TPC are extremely clean, noise filtering is not necessary.

**Hit Reconstruction.** The second stage of the signal processing is the reconstruction of hits, indicating an energy deposition in the detector. A peak finder scans the deconvolved TPC waveforms for each wire on the whole readout time looking for spikes above the waveform’s baseline. It then fits these peaks with gaussian shapes and stores the fit parameters such as the quality of the fit, the peak time, height and area under the gaussian fit. The information resulting from this process a single spike form a single reconstructed “hit”. The next steps in the event reconstruction chain will then decide if rejecting hits with poor fits. It is important to notice how the height and width of the hit depend on the topology of the event: for example, a particle running parallel to the wire planes will leave a series of sharp hits on many consecutive wires, while a particle traveling towards the planes will leave a long, wide hit on very few wires. The height of the hits and their integral is proportional to the charge collected on the wire, so it depends on the particle type.

The event reconstruction chain uses collection of hits to form more complex objects associated with the particles in the detector. The development of different approaches to accomplish this task is an extremely hot topic in LArTPC event reconstruction which spans from more traditional approaches such as line-clustering [?] [argoneut paper](#) to the use of machine learning tools [?] [KAZU'S paper](#). Generally speaking, the scope of hit clustering and event reconstruction to provide shower-like or track like-objects with an associated energy reconstruction. This is because different particles have different topology in the detector – electrons and photon create electromagnetic showers, resulting in shower-like topologies, while muons and hadrons leave track-like signals. For the scope of these thesis, we will describe only LArIAT’s approach to track reconstruction even if we recognize the breath of LArTPC event reconstruction is much wider. We are interested in the reconstruction of pions and kaons in the active volume, whose topology is track-like.

**2D Clustering Reconstruction.** The LArIAT reconstruction of track-like objects starts by clustering hits on the collection and induction planes separately with the use of the TrajCluster clustering package [?] [Bruce](#). TrajCluster looks for a collection of hits in the wire-time 2D space which can be described with a line-like 2D trajectory. TrajCluster reconstructs trajectories by adding trajectory points to the leading edge of the trajectory while stepping through the 2D space of hits. Several factors determine whether a hit is added to the trajectory, including but not limited to

1. the goodness of the fit of the single hit,
2. the charge of the hit compared to the average charge and RMS of the hits already forming the trajectory,
3. the goodness of trajectory fit with and without the hit addition,
4. the angle between the two lines formed by the collection of hits before and after the considered hit in the trajectory.

**3D TrackReconstruction.** The 3D tracking set of algorithms uses clusters close in time on the induction and collection planes as starting point to form a 3D track. Firstly, it constructs a tentative 3D trajectory using the edges of the clusters. Then, it projects back the tentative trajectory on to the planes and adjusts the parameters of the 3D track fit such that they minimize the distance between the fit projections and the track hits in all wire planes simultaneously. The track algorithm can use multiple clusters in one plane, but it can never break them in smaller groups of hits. This algorithm was first developed for the ICARUS collaboration [11].

## 2.2 The Intensity Frontier Program

### 2.2.1 SBN: Neutrino Interaction and Detection

### 2.2.2 DUNE: Rare Decay Searches

DUNE will achieve a wide non-accelerator physics program. The key elements for a rare decay experiment are: massive active volume, long exposure, high identification efficiency and low background. Figure 2.1 shows the current best experimental limits on nucleon decay lifetime over branching ratio (dots). Historically, the dominant technology used in these searches has been water Cherenkov detectors: all the best experimental limits on every decay mode are indeed set by Super-Kamiokande [?, ?]. It is particularly important to notice that the kaon energy for the proton decay mode  $p \rightarrow K^+ \bar{\nu}$  is under Cherenkov threshold. Super-Kamiokande set the limit on the lifetime for the  $p \rightarrow K^+ \bar{\nu}$  mode by relying on photons from nuclear de-excitation and on the muon tagging in the kaon decay leptonic mode. For this reason, an attractive alternative approach to identifying nucleon decay is the use of a Liquid Argon Time Projection Chamber (LArTPC).

LArTPCs can complement nucleon decay searches in modes where water Cherenkov detectors are less sensitive, especially  $p \rightarrow K^+ \bar{\nu}$ . According to [?], DUNE will have an active volume large enough, have sufficient shielding from the surface, and will run for lengths of time sufficient to compete with Hyper-K, opening up the opportunity for the discovery of nucleon decay.

### 2.2.3 Enabling the next generation of discoveries: LArIAT

LArIAT, a small Liquid Argon Time Projection Chamber (LArTPC) in a test beam, is designed to perform an extensive physics campaign centered on charged particle cross section measurements while characterizing the detector performance for future

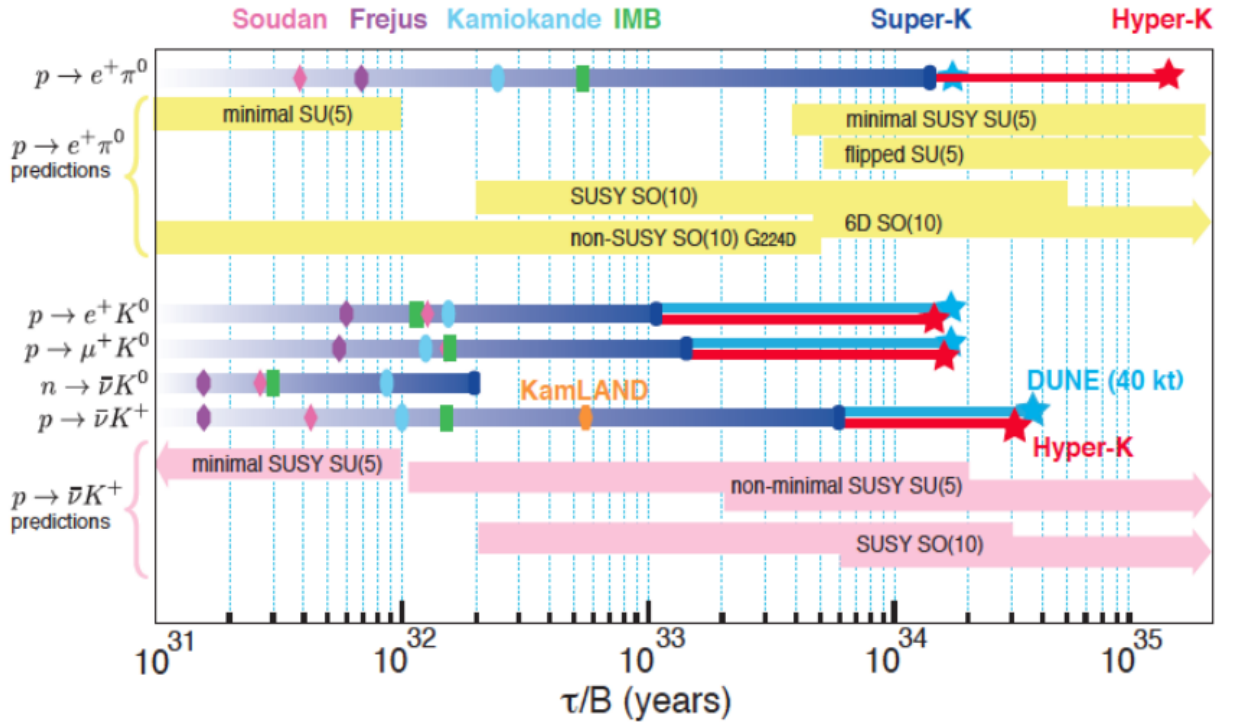


Figure 2.1: Proton decay lifetime limits from passed and future experiments.

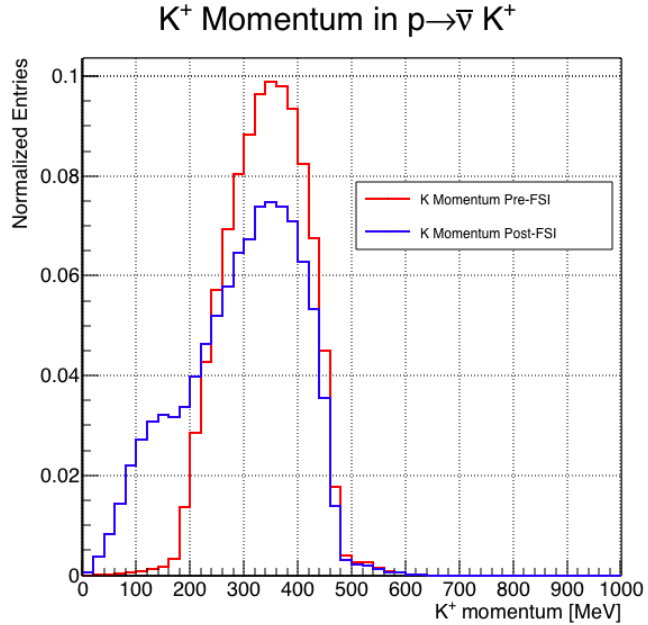


Figure 2.2: Momentum of the kaon outgoing a proton decay event as simulated by the Genie 2.8.10 event generator in argon. The red line represent the kaon momentum distribution before undergoing the simulated final state interaction inside the argon nucleus, while the blue line represents the momentum distribution after FSI.

LArTPCs. LArTPC represents one of the most advanced experimental technologies for physics at the Intensity Frontier due to its full 3D-imaging, excellent particle identification and precise calorimetric energy reconstruction. This complex technology however needs a thorough calibration and dedicated measurements of some key quantities to achieve the precision required for the next generation of discoveries at the Intensity Frontier which LArIAT can provide.

The LArIAT LArTPC is deployed in a dedicated calibration test beamline at Fermilab. We use the LArIAT beamline to characterize the charge particles before they enter the TPC: the particle type and initial momentum is known from beamline information. The precise calorimetric energy reconstruction of the LArTPC technology enables the measurement of the total differential cross section for tagged hadrons. The Pion-Nucleus and Kaon-Nucleus total hadronic interaction cross section have never been measured before in argon and they are a fundamental step to shed light on light meson interaction in nuclei. Additionally, these measures provides a key input to neutrino physics and proton decay studies in future LArTPC experiments like SBN and DUNE. **add paragraph on all wonderful things lariat can do... some event displays would be nice!**

**ADD genie proton decay kaon distribution and lariat beamline overlayed** The signature of a proton decay event in the “LAr golden mode” is the presence of a single kaon of about 400 MeV in the detector.

# Chapter 3

## LArIAT: Liquid Argon In A Testbeam

In this chapter, we describe the LArIAT experimental setup. We start by illustrating the journey of the charge particles in the Fermilab accelerator complex, from the gaseous thermal hydrogen at the Fermilab ion source to the delivery of the LArIAT tertiary beam at MC7. We then describe the LArIAT beamline detectors, the LArTPC, the DAQ and the monitoring system.

### 3.1 The Particles Path to LArIAT

LArIAT's particles history begins in the Fermilab accelerator complex with a beam of protons. The process of protons acceleration develops in gradual stages (see picture 3.1): gaseous hydrogen is ionized in order to form  $H^-$  ions; these ions are boosted to 750 keV by a Cockcroft-Walton accelerator and injected to the Linac linear accelerator that increases their energy up to 400 MeV; then,  $H^-$  ions pass through a carbon foil and lose the two electrons; the resulting protons are then injected into a rapid cycling synchrotron, called Booster; at this stage, protons reach 8 GeV of energy and are compacted into bunches; the next stage of acceleration is the Main Injector,

a synchrotron which accelerates the bunches up to 120 GeV; in the Main Injector, several bunches are merged into one and used for the injection in the last stage.

The Fermilab accelerator complex works in supercycles of roughly 60 seconds in duration. The beam is split by electrostatic septa and delivered at different experimental halls all over the lab. A 120 GeV/c primary proton beam with variable intensity is extracted in four-second “spills” and sent to the Meson Center beam line.

LArIAT’s home at Fermilab is the Fermilab Test Beam Facility (FTBF), where the experiment characterizes a beam of charge particles downstream from the Meson Center beam line. Here, the primary beam is focused onto a tungsten target to create LArIAT’s secondary beam. The composition of the secondary particle beam is mainly positive pions. The momentum peak of the secondary beam was fixed at 64 GeV/c for the LArIAT data considered in this work, although the beam is tunable in momentum between 8-80 GeV/c; this configuration of the secondary beamline assured a stable beam delivery at the LArIAT experimental hall.

The secondary beam impinges then on a copper target within a steel collimator inside the LArIAT experimental hall (MC7) to create the LArIAT tertiary beam, (shown in Fig. 3.2). The steel collimator selects particles produced with a 13° production angle at the target down the beamline. The particles are then bent by 10° through a pair of dipole magnets. By configuring the field intensity of the magnets we allow the particles of LArIAT’s tertiary beam to span a momentum range from 0.2 to 1.4 GeV/c. The polarity of the magnet is also configurable and determines the sign of the beamline particles which are focused on the LArTPC. If the magnets polarity is positive the tertiary beam composition counts mostly pions and protons with a small fraction of electrons, muons, and kaons. It is the job of the LArIAT beamline detectors to select the particles polarity, to perform particle identification in the beamline and to measure the momentum of the tertiary beam particles before they get to the LArTPC. The LArIAT detectors are described in the following paragraphs.

## Fermilab Accelerator Complex

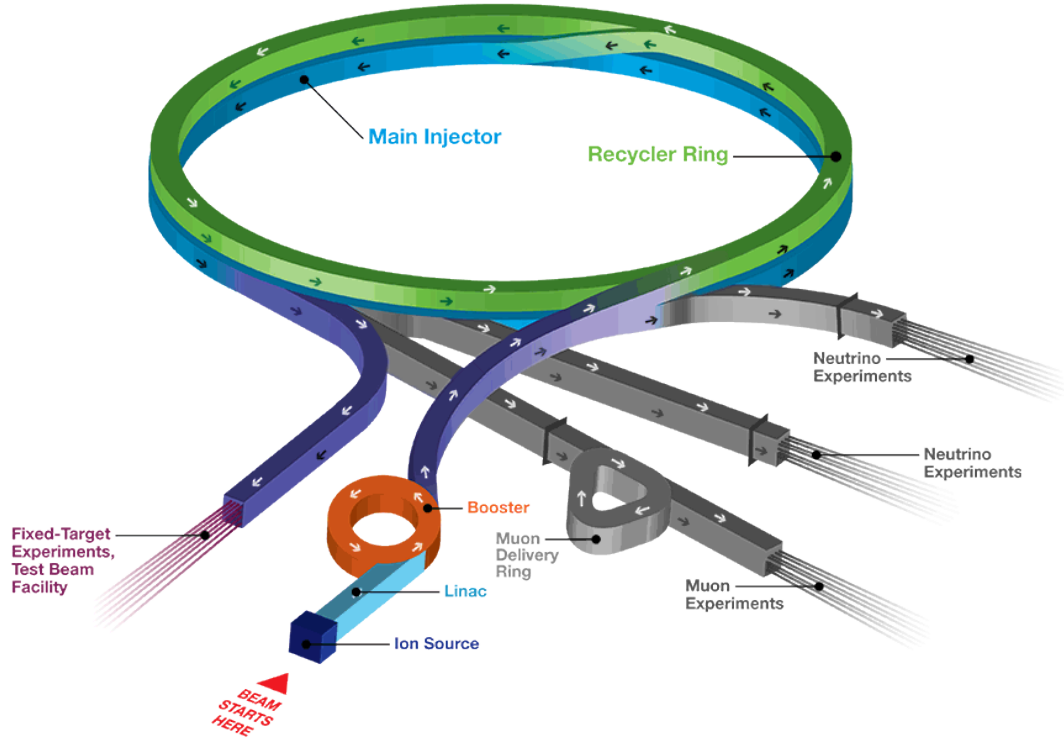


Figure 3.1: Layout of Fermilab Acellerator complex.

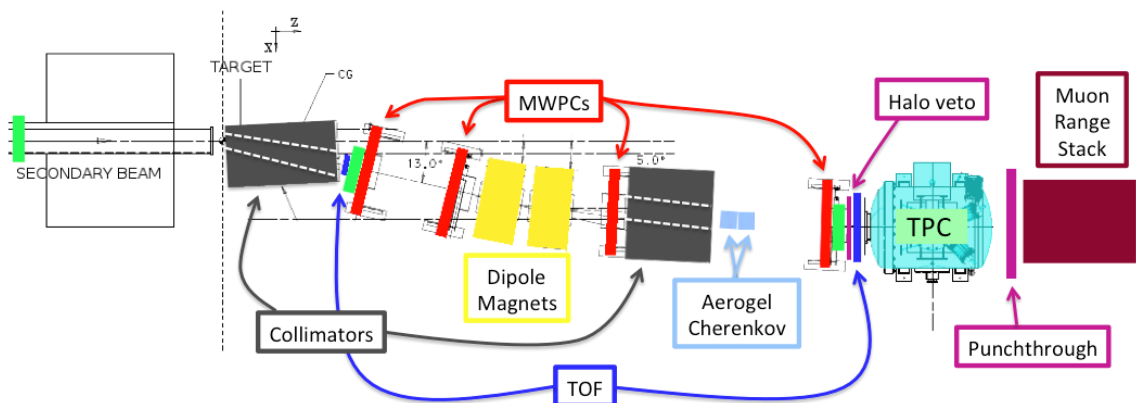


Figure 3.2: Bird's eye view of the LArIAT tertiary beamline. In grey: upstream and downstream collimators; in yellow: bending magnets; in red: wire chambers; in blue: time of flight; in green: liquid argon TPC volume; in maroon: muon range stack.

## 3.2 LArIAT Tertiary Beam Instrumentation

The instrumentation of LArIAT tertiary beam and the TPC components have changed several times during the three years of LArIAT data taking. The following paragraphs describe the components operational during “Run II”, the data taking period relevant to the hadron cross section measurements.

The key components of the tertiary beamline instrumentation for the hadron cross section analyses are the two bending magnets, a set of four wire chambers (WCs) and two time-of-flight scintillating paddles (TOF) and, of course, the LArTPC. The magnets determine the polarity of the particles in the tertiary beam; the combination of magnets and wire chambers determines the particles’ momentum, which is used to determine the particle species in conjunction with the TOF. A muon range stack downstream from the TPC and two sets of cosmic paddles configured as a telescope surrounding the TPC are also used for calibration purposes.

### 3.2.1 Bending Magnets

LArIAT uses a pair of identical Fermilab type “NDB” electromagnets, recycled from the Tevatron’s anti-proton ring, in a similar configuration used for the MINERvA T-977 test beam calibration [34]). The magnets are a fundamental piece of the LArIAT beamline equipment, as they are used for both particle identification and momentum measurement before the LArTPC. The sign of the current in the magnets allows us to select either positively or negatively charged particles; the value of the magnetic field is used in the momentum determination and in the subsequent particle identification.

We describe here the characteristics and response of one magnet, as the second one has a similar response, given its identical shape and history. Each magnet is a box with a rectangular aperture gap in the center to allow for the particle passage. The magnet aperture measures 14.224 cm in height, 31.75 cm in width, and 46.67 cm in length.

Since the wire chambers aperture ( $\sim 12.8 \text{ cm}^2$ ) is smaller than the magnet aperture, only the central part of the magnet gap is utilized. The field is extremely uniform over this limited aperture and was measured with two hall probes, both calibrated with nuclear magnetic resonance probes. The probes measured the excitation curve shown in Figure 3.3.

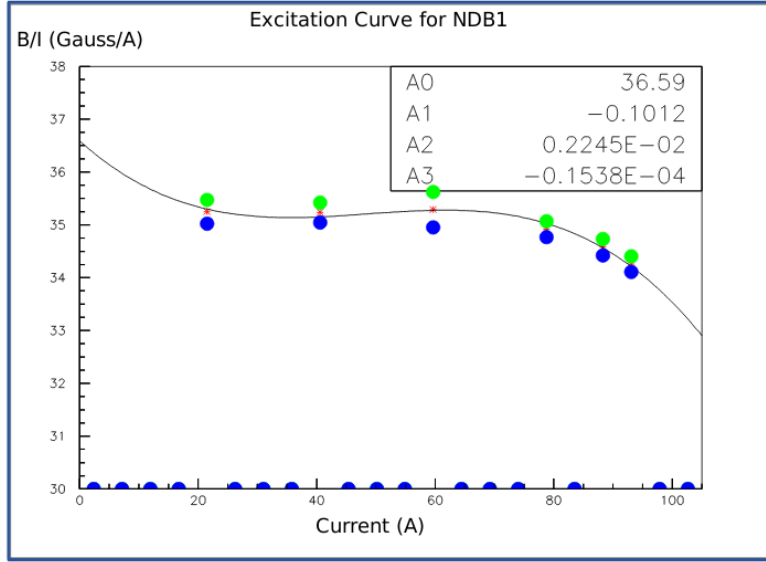


Figure 3.3: Magnetic field over current as a function of the current, for one NDB magnet (excitation curve). The data was collected using two hall probes (blue and green). We fit the readings with a cubic function (black) to average of measurements (red) given in the legend.

The current through the magnets at a given time is identical in both magnets. For the Run II data taking period, the current settings explored were 60A ( $B \sim 0.21 \text{ T}$ ) and 100A ( $B \sim 0.35 \text{ T}$ ) in both polarities. Albeit advantageous to enrich the tertiary beam composition with high mass particles such as kaons, we never pushed the magnets current over 100 A, not to incur in overheating. During operation, we operated a air and water cooling system on the magnets and we remotely monitored the magnets temperature.



Figure 3.4: One of the four Multi Wire Proportional Chambers (WC) used in the LArIAT tertiary beamline and relative read-out electronics.

### 3.2.2 Multi-Wire Proportional Chambers

LArIAT uses four multi-wire proportional chambers, or wire chambers (WC) for short, two upstream and two downstream from the bending magnets. The geometry of one chamber is shown in Figure 3.4: the WC effective aperture is a square of 12.8 cm perpendicular to the beam direction. Inside the chamber, the 128 horizontal and 128 vertical wires hang at a distance of 1 mm from each other in a mixture of 85% Argon and 15% isobutane gas. The WC operating voltage is between 2400 V and 2500 V. The LArIAT wire chambers are an upgraded version of the Fenker Chambers [37], where an extra grounding improves the signal to noise ratio of the electronic readout.

Two ASDQ chips [60] mounted on a mother board plugged into the chamber serve as front end amplifier/discriminator. The chips are connected to a multi-hit TDC [46] which provides a fast OR output used as first level trigger. The TDC time resolution is 1.18 ns/bin and can accept 2 edges per 9 ns. The maximum event rate acceptable by the chamber system is of 1 MHz: this rate is not a limiting factor considering that **the rate of the tertiary particle beam at the first wire chamber is estimated to be less than 15 kHz**. A full spill of data occurring once per supercycle is stored on the TDC board memory at once and read out by a specially designed controller. We use LVDS cables to carry both power and data between the controller and the TDCs and from

the controller to the rest of the DAQ.

### Multi-Wire Proportional Chambers functionality

We use the wire chamber system together with the bending magnets to measure the particle's momentum.

In the simplest scenario, only one hit on each and every of the four wire chambers is recorded during a single readout of the detector systems. Thus, we use the hit positions in the two wire chambers upstream of the magnets to form a trajectory before the bend, and the hit positions in the two wire chambers downstream of the magnets to form a trajectory after the bend. We use the angles in the XZ plane between the upstream and downstream trajectories to calculate the  $Z$  component of the momentum as follows:

$$P_z = \frac{B_{eff}L_{eff}}{3.3(\sin(\theta_{DS}) - \sin(\theta_{US}))}, \quad (3.1)$$

where  $B_{eff}$  is the effective maximum field in a square field approximation,  $L_{eff}$  is the effective length of both magnets (twice the effective length of one magnet),  $\theta_{US}$  is the angle off the  $z$  axis of the upstream trajectory,  $\theta_{DS}$  is the angle off the  $z$  axis of the downstream trajectory and  $3.3 c^{-1}$  is the conversion factor from [T·m] to [MeV/c]. By using the hit positions on the third and fourth wire chamber, we estimate the azimuthal and polar angles of the particle trajectory, and we are able to calculate the other components of the momentum.

The presence of multiple hits in a single wire chamber or the absence of hits in one (or more) wire chambers can complicate this simple scenario. The first complication is due to beam pile up, while the latter is due to wire chamber inefficiency. In the case of multiple hits on a single WC, at most one wire chamber track is reconstructed per event. Since the magnets bend particles only in the X direction, we assume the particle trajectory to be roughly constant in the YZ plane, thus we keep the

combination of hits which fit best with a straight line. It is still possible to reconstruct the particle’s momentum even if the information is missing in either of the two middle wire chambers (WC2 or WC3), by constraining the particle trajectory to cross the plane in between the magnets.

Events satisfying the simplest scenario of one single hit in each of the four wire chambers form the “Picky Track” sample. We construct another, higher statistics sample, where we loosen the requirements on single hit and wire chamber efficiency: the “High Yield” sample. For LArIAT Run II, the High Yield sample is about three times the Picky Tracks statistics. For the first measurements of the LArIAT hadronic cross section, we use the Picky Tracks sample because the uncertainty on the momentum is smaller and the comparison with the beamline MC results is straightforward compared with the High Yield sample; a possible future update and cross check of these analysis would be the use of the High Yield sample.

#### Four point track momentum uncertainty

### 3.2.3 Time-of-Flight System

Two scintillator paddles, one upstream to the first set of WCs and one downstream to the second set of WCs form LArIAT time-of-flight (TOF) detector system.

The upstream paddle is made of a 10 x 6 x 1 cm scintillator piece, read out by two PMTs mounted on the beam left side which collect the light from light guides mounted on all four edges of the scintillator. The downstream paddle is a 14 x 14 x 1 cm scintillator piece read out by two PMTs on the opposite ends of the scintillator. The relatively thin width on the beamline direction minimizes energy loss of the particles coming from the target in the scintillator material.

The CAEN 1751 digitizer is used to digitize the TOF PMTs signals at a sampling rate of 1 GHz. The 12 bit samples are stored in a circular memory buffer. At trigger time, data from the TOF PMTs are recorded to output in a 28.7  $\mu$ s windows starting

approximately 8.4  $\mu$ s before the trigger time.

### TOF functionality

The TOF signals rise time (10-90%) is 4 ns and a full width, half-maximum of 9 ns consistent in time. The signal amplitudes from the upstream TOF and downstream TOF are slightly different: 200 mV for the upstream PMTs but only 50 mV for downstream PMTs. The time of the pulses was calculated utilizing an oversampled template derived from the data itself. We take the pulse pedestal from samples far from the pulse and subtract it to the pulse amplitude. We then stretch vertically a template to match the pedestal-subtracted pulse amplitude and we move it horizontally to find the time. With this technique, we find a pulse time-pickoff resolution better than 100 ps. The pulse pile up is not a significant problem given the TOF timing resolution and the rate of the particle beam. Leveraging on the pulses width uniformity of any given PMT, we flag events where two pulses overlap as closely in time as 4 ns with an 90% efficiency according to simulation.

We combine the pulses from the two PMTs on each paddle to determine the particles' arrival time by averaging the time measured from the single PMT, so to minimize errors due to optical path differences in the scintillator. However, a time spread of approximately 300 ps is present in both the upstream and downstream detectors, likely due to transit time jitter in the PMTs themselves. There is no evidence of systematic timing drift over long data-taking periods such as 3-4 months: the maximum variation of the average time differences between pairs of PMTs reading out the same scintillator is of the order of 150 ps.

#### 3.2.4 Punch-Through and Muon Range Stack Instruments

The punch-thorough and the muon range stack (MuRS) detectors are located downstream of the TPC. These detectors provide a sample of TPC crossing tracks without



Figure 3.5: Image of the down stream time of flight paddle, PMTs and relative support structure before mounting.

relying on TPC information and can be used to improve particle ID for muons and pions with momentum higher than 450 MeV/c.

The punch-thorough is simple sheet of scintillator material, read out by two PMTs. The MuRS is a segmented block of steel with four slots instrumented with scintillation bars. The four steel layers in front of each instrumented slot are 2 cm, 2 cm, 14 cm and 16 cm wide in the beam direction. Each instrumented slot is equipped with four scintillation bars each, positioned horizontally in the direction orthogonal to the beam. Each scintillator bar measures  $\text{?} \times \text{?} \times 2$  cm and it is read out by one PMT.

The signals from both the punch-thorough and the MuRS PMTs are digitized in the CAEN V1740, same as the TPC; the details of this discriminator are laid out in 3.3.2. It is worth noticing that the sampling time of the CAEN V1740 is slow (of the order of 128 ns), so pulse shape information from the PMT is lost. Punch-thorough and MuRS hits are formed utilizing the digital discriminator signals under threshold at a given time, where we obtain the threshold for each PMT directly on data distributions.

### 3.2.5 LArIAT Cosmic Ray Paddle Detectors

LArIAT triggers both on beam events and on cosmic rays events. We perform this latter trigger by using two sets of cosmic ray paddle detectors (a.k.a. “cosmic towers”.) The cosmic towers frame the LArIAT cryostat, as one sits in the downstream left corner and the other sits in the upstream right corner of the cryostat. Two paddle sets of four scintillators pieces each make up each cosmic tower, an upper set and a lower set per tower. Of the four paddles, a couple of two matched paddles stands upright while the a second matched pair lies across the top of the assembly in the top sets (or across the bottom of the assembly in the bottom sets). The horizontal couple is used as a veto for particles traveling from inside the TPC out. The four signals from the vertical paddles along one of the body diagonals of the TPC are combined in a logical “AND”. This allows to select cosmic muons crossing the TPC along one of its diagonals. Cosmic ray tracks crossing both anode and cathode populate the events triggered this way. This particularly useful sample of tracks (which we can safely assume to be associated with 5 GeV muons) can be used for many tasks; for example, we use anode-cathode piercing tracks to cross check the TPC electric field on data (see Appendix A), to calibrate the charge response of the TPC wires for the full TPC volume and to measure the electron lifetime in the chamber (see section ??).

A Zener-diode Hamamatsu H5783 PMT collects the light from a wavelength-shifting optical fiber which runs along one of the long sides of each paddle. A custom-made PMT Amplifier and Discrimination (PAD) circuit mounted at one end of the paddle collects signals from the PMTs and sends them to the Control and Concentrator Unit (CCU). We use the same connection to power the PMT, control voltage and threshold, and output the PMT signal as logic ECL pulse. We retrieved the scintillation paddles from the decommissioning of the CDF detector at Fermilab and we used only the paddles with a counting efficiency greater than 95% and low noise at working

voltage. The measured trigger rate of the whole system is 0.032 Hz, corresponding to  $\sim 2$  muons per minute.



Figure 3.6: Photograph of one of the scintillation counters used in the cosmic towers.

### 3.3 In the Cryostat

#### 3.3.1 Cryogenics and Argon Purity

LArIAT repurposed the ArgoNeuT cryostat [9] in order to use it in a beam of charge particles, and added a new process piping and a new liquid argon filtration system in FTBF. Inside the LArIAT experimental hall, the cryostat sits on the beam of charge particles with its horizontal main axis oriented parallel to the beam.

Two volumes make up LArIAT cryostat, shown in Figure 3.7: the inner vessel and the outer vessel. Purified liquid argon fills the inner vessel, while the outer volume provides insulation through a vacuum jacket equipped with layers of aluminized mylar superinsulation. The inner vessel is a cylinder of 130 cm length and 6.2 cm diameter, containing about 550 L of LAr, corresponding to a mass of 0.76 ton. We run the signal cables for the LArTPC and the high voltage feedthrough through a “chimney” at the top and mid-length of the cryostat.

Given the different scopes of the ArgoNeuT and LArIAT detectors, we made

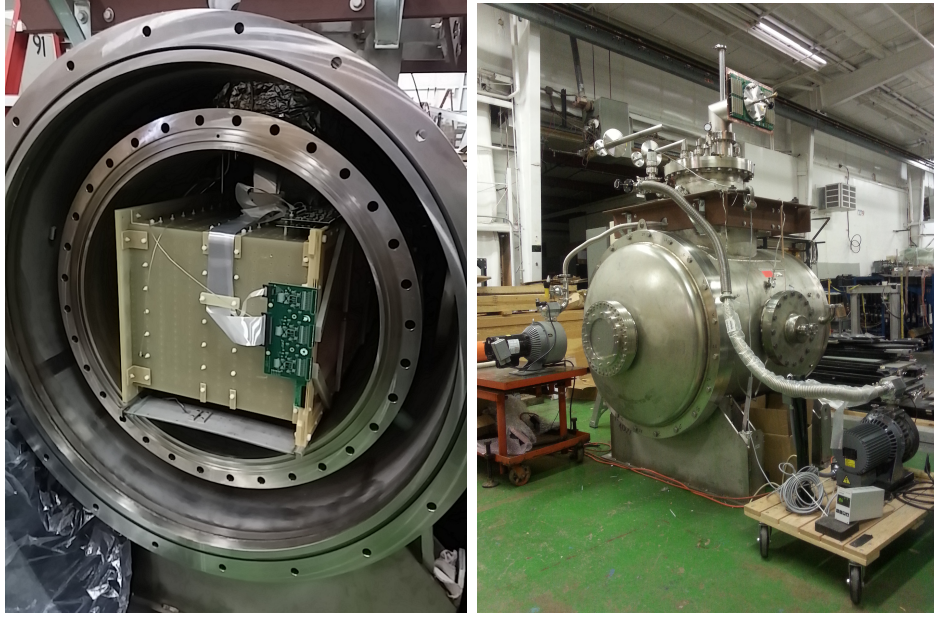


Figure 3.7: Left: the LArIAT TPC in the inner volume of the open cryostat. Right: cryostat fully sealed ready to be transported to FTBF.

several modification to the ArgoNeuT cryostat in order to use it in LArIAT. In particular, the modification shown in Figure 3.8 were necessary to account for the beam of charged particles entering the TPC and to employ the new FTBT liquid argon purification system. We added a “beam window” on the front outer end cap and an “excluder” on the inner endcap, with the scope of minimizing the amount of dead material upstream of the TPC’s active volume. Doing so, we reduced the amount of uninstrumented material before the TPC from  $\sim 1.6$  radiation lengths ( $X_0$ ) (ArgoNeuT) to less than  $0.3 X_0$  (LArIAT). To allow studies of the scintillation light, we added a side port feedthrough which enables the mounting of the light collection system, as well as the connections for the corresponding signal and high-voltage cables (see Section 3.3.3). We modified the bottom of the cryostat adding Conflat and ISO flange sealing to connect the liquid argon transfer line to the new argon cooling and purification system.

As in any other LArTPC, argon purity is a crucial parameter for LArIAT. Indeed, the presence of contaminants effects both the basic working principles of a LArTPC,



Figure 3.8: Main modifications to the ArgoNeuT cryostat: 1) outlet for connection to the purification system at the bottom of the cryostat; 2) the “beam-window” on the outer endcap and “excluder” which reduce the amount of non-instrumented material before the TPC; 3) the side port to host the light collection system.

as shown in section 2.1.2: electronegative contaminants such as oxygen and water decrease the number of ionization electrons collected on the wires after drifting through the volume. In addition, contaminants such as Nitrogen decrease the light yield from scintillation light, especially in its slow component. In LArIAT, contaminations should not exceed the level of 100 parts per trillion (ppt). We achieve this level of purity in several stages. The specifics required for the commercial argon bought for LArIAT are 2 parts per million (ppm) oxygen, 3.5 ppm water, and 10 ppm nitrogen. This argon is monitored with the use of commercial gas analyzer. Argon is stored in a dewar external to LArIAT hall and filtered before filling the TPC. LArIAT uses a filtration system designed for the Liquid Argon Purity Demonstrator (LAPD) [35]: half of a 77 liter filter contains a 4A molecular sieve (Sigma-Aldrich [70]) apt to remove mainly water, while the other half contains BASF CU-0226 S, a highly dispersed copper oxide impregnated on a high surface area alumina, apt to remove mainly oxygen [15]. A single pass of argon in the filter is sufficient to achieve the necessary

purity, unless the filter is saturated. In case the filter saturates, the media needs to be regenerated by using heated gas; this happened twice during the Run II period<sup>1</sup>. The filtered argon reaches the inner vessel via a liquid feedthrough on the top of the cryostat. Argon is not recirculated in the system, rather it boils off and vent to the atmosphere. During data taking, we replenish the argon in the cryostat several times per day to keep the TPC high voltage feedthrough and cold electronics always submerged. In fact, we constantly monitor the level, temperature, and pressure of the argon both in the commercial dewar and inside the cryostat during data taking.

### 3.3.2 LArTPC: Charge Collection

The LArIAT Liquid Argon Time Projection Chamber is a rectangular box of dimensions 47 cm (width) x 40 cm (height) x 90 cm (length), containing 170 liters of Liquid Argon. The LArTPC three major subcomponents are

- 1) the cathode and field cage,
- 2) the wire planes,
- 3) the read-out electronics.

#### Cathode and field cage

A G10 plain sheet with copper metallization on one of the 40 x 90 cm inner surfaces forms the cathode. A high-voltage feedthrough on the top of the LArIAT cryostat delivers the high voltage to the cathode; scope of the high voltage system (Figure 3.9) is to drift ionization electrons from the interaction of charged particles in the liquid argon to the wire planes. The power supply used in this system is a Glassman LX125N16 [44] capable of generating up to -125 kV and 16 mA of current, but

---

1. We deemed the filter regeneration necessary every time the electron lifetime dropped under 100  $\mu$ s.

operated at -23.5kV during LArIAT Run-II. The power supply is connected via high voltage cables to a series of filter pots before finally reaching the cathode.

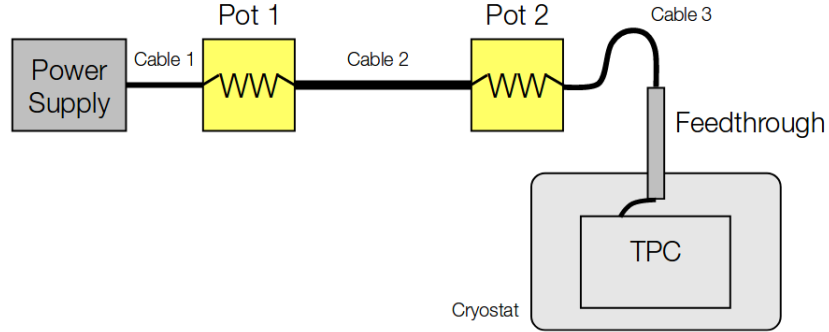


Figure 3.9: Schematic of the LArIAT high voltage system.

The field cage is made of twenty-three parallel copper rings framing the inner walls of the G10 TPC structure. A network of voltage-dividing resistors connected to the field cage rings steps down the high voltage from the cathode to form a uniform electric field. The electric field over the entire TPC drift volume is 486 V/cm (see A). The maximum drift length, i.e. the distance between cathode and anode planes, is 47 cm.

### Wire planes

The wire planes measure the charge deposited in the TPC active volume. The drifting charge induces a current on the wire of the inner planes and it is collected on the collection plane wires. LArIAT counts three wire planes separated by 4 mm spaces: in order of increasing distance from the cathode, they are the shield, the induction and the collection plane. The “wire pitch”, i.e., the distance between two consecutive wires in a given plane, is 4 mm. The shield plane counts 225 parallel wires of equal length oriented vertically. This plane is not connected with the read-out electronics; rather it shields the outer planes from extremely long induction signals due to the ionization chamber in the whole drift volume. As the shield plane acts almost like a

Faraday cage, the shape of signals in the first instrumented plane (induction) results easier to reconstruct. Both the induction and collection planes count 240 parallel wires of different length oriented at  $60^\circ$  from the vertical with opposite signs. Electrons moving past the induction plane will induce a bipolar pulse on its wires; the drifting electrons will be then collected on the collection plane's wires, forming a unipolar pulse.

The three wire planes and the cathode form three drift volumes, as shown in Figure 3.10. The main drift volume is defined as the region between the cathode plane and the shield plane (C-S). The other two drift regions are those between the shield plane and the induction plane (S-I), and between the induction plane and the collection plane (I-C). The electric field in these regions is chosen to satisfy the charge transparency condition and allow for 100% transmission of the drifting electrons through the shield and the induction planes.

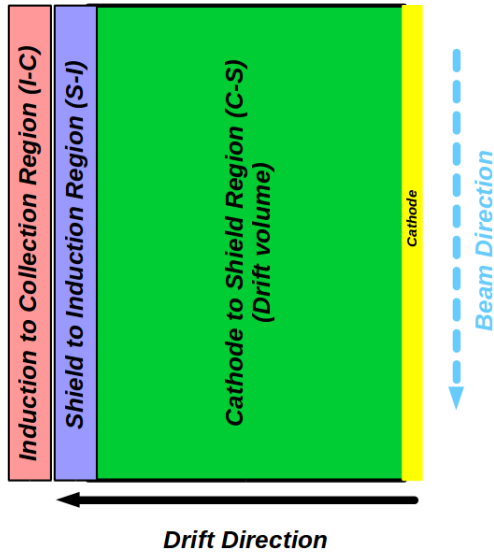


Figure 3.10: Schematic of the three drift regions inside the LArIAT TPC: the main drift volume between the cathode and the shield plane (C-S) in green, the region between the shield plane and the induction plane (S-I) in purple, and the region between the induction plane and the collection plane (I-C) in pink.

Table 3.1 provides the default voltages applied to the cathode and the shield,

induction, and collection plane.

Table 3.1: Cathode and anode planes default voltages

Cathode	Shield	Induction	Collection
-23.17 kV	-298.8 V	-18.5 V	338.5 V

## Electronics

Dedicated electronics read the induction and collection plane wires, for a total of 480-channel analog signal path from the TPC wires to the signal digitizers. A digital control system for the TPC-mounted electronics, a power supply, and a distribution system complete the front-end system. Figure 3.11 shows a block diagram of the overall system. The direct readout of the ionization electrons in liquid argon forms typically small signals on the wires, which need amplification in order to be processed. LArIAT performs the amplification stage directly in cold with amplifiers mounted on the TPC frame inside the liquid argon, achieving a remarkable Signal-to-Noise ratio. The signal from the ASICs are driven to the other end of the readout chain, to the CAEN V1740 digitizers. The CAEN V1740 has a 12 bit resolution and a maximum input range of 2 VDC, resulting in about 180 ADC count for a crossing MIP.

### 3.3.3 LArTPC: Light Collection System

The collection of scintillation photons is the second mechanism of particle detection in argon other than the ionization electrons. Over the course of LArIAT’s three years of data taking, the light collection system changed several times. We describe here the light collection system for Run II. Two PMTs, a 3-inch diameter Hamamatsu R-11065 and 2-inch diameter ETL D757KFL [5], as well as three SiPMs arrays (two Hamamatsu S11828-3344M 4x4 arrays and one single-channel SensL MicroFB-60035) are mounted on the PEEK support structure. PEEK screws into an access flange

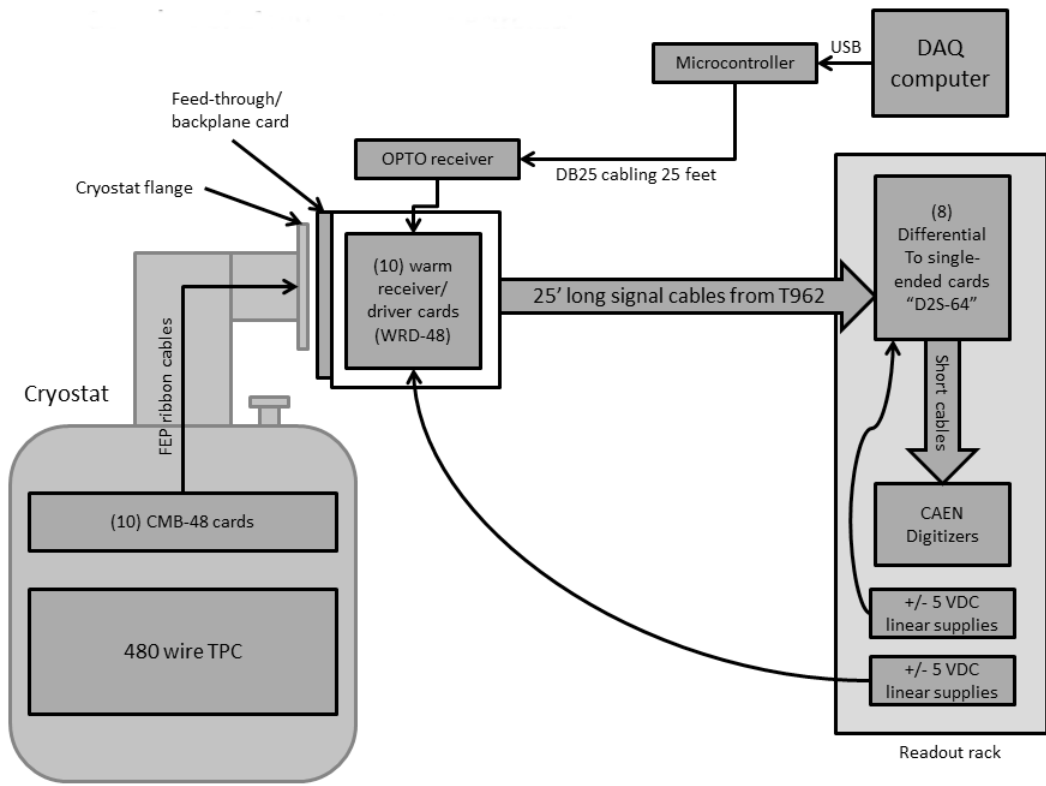


Figure 3.11: Overview of LArIAT Front End electronics.

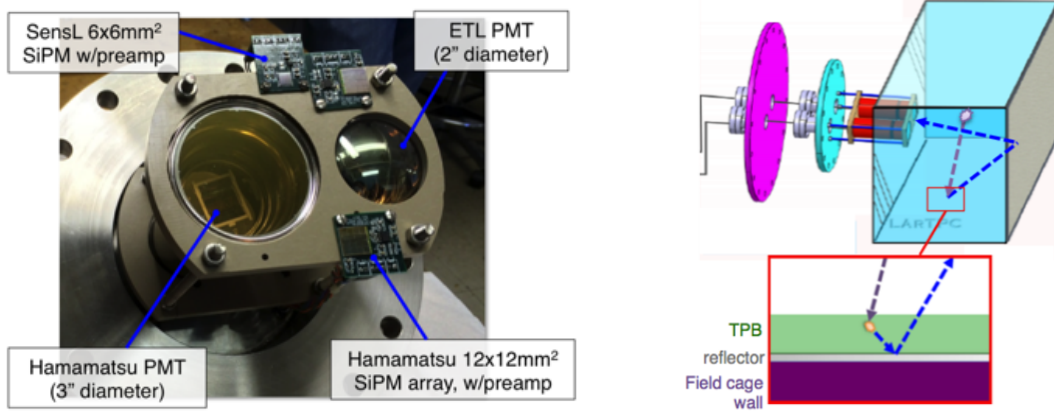


Figure 3.12: LArIAT’s photodetector system for observing LAr scintillation light inside the TPC (left), and a simplified schematic of VUV light being wavelength-shifting along the TPB-coated reflecting foils (right).

as shown in Figure 3.12, on the anode side, leaving approximately 5 cm of clearance from the collection plane.

Liquid argon scintillates in vacuum-ultraviolet (VUV) range at 128 nm; since cryogenic PMTs are not sensitive to VUV wavelengths, we need to shift the light in a region visible to the PMTs. In LArIAT, the wavelength shifting is achieved by installing on the four walls of the TPC highly-reflective VIKUITY dielectric substrate foils coated with a thin layer of tetraphenyl-butadiene (TPB). The scintillation light interaction with the TPC emits one or more visible photons, we are then reflected into the chamber. Thus, the light yield increases and results more uniform across the TPC active volume, allowing the possibility of light-based calorimetry, currently under study.

For Run II, we coated both the windows of the ETL PMT and SensL SiPM with a thin layer of TPB. In doing so, some of the VUV scintillation light converts into visible right at the sensor faces, keeping information on the direction of the light source. Information about the light directionality is lost for light reflected on foils, as the reflection is uniform in angle.

## 3.4 Trigger and DAQ

The LArIAT DAQ and trigger system governs the read out of all the many subsystems forming LArIAT. The CAEN V1495 module and its user-programmable FPGA are the core of this system. Every 10 ns, this module checks for matches between sixteen logical inputs and user-defined patterns in the trigger menu; if it finds a match for two consecutive clock ticks, that trigger fires.

LArIAT receives three logic from the Fermilab accelerator complex related to the beam timing which we use as input triggers: a pulse just before the beam, a pulse indicating beam-on, and a beam-off pulse.

The beam instruments, the cosmic ray taggers, and the light collection system provide the other NIM-standard logic pulse inputs to the trigger decision. We automatically log the trigger inputs configuration with the rest of the DAQ configuration at the beginning of each run.

Fundamental inputs to the trigger card come from the TOF (see Sec. 3.2.3) and the wire chambers (see Sec. 3.2.2), as activity in these systems points to the presence of a charged particle in tertiary beam line. In particular, the discriminated pulses from the TOF PMTs form a NIM logic pulse for the trigger logic. We ask for a coincidence within a 20 ns window for all the pulses from the PMTs looking at the same scintillator block and use the coincidence between the upstream and downstream paddle to inform the trigger decision. In order to form a coincidence between the upstream and downstream paddles, we delay the upstream paddle coincidence by 20 ns and widen it by 100 ns. The delay and widening are necessary to account for both lightspeed particles and slower particles (high-mass) to travel the 6.5 m between the upstream and the downstream paddles. For the read out of the wire chambers, we use a total of sixteen multi-hit TDCs, four per chamber: two TDC per plane (horizontal and vertical), sixty-four wires per TDC. In each TDC, we keep the logical “OR” for any signal over threshold from the sixty-four wires. We then require a

coincidence between the “OR” for the horizontal TDCs and the “OR” for the vertical TDCs: with this logic we make sure that at least one horizontal wire and one vertical wire saw significant signal in one wire chamber. The single logical pulse from each of the four wire chambers feeds into the first four inputs to the V1495 trigger card. We require a coincidence within 20 ns of at least three logical inputs to form a trigger.

The cosmic towers (see Section 3.2.5) provide another primary input to the trigger, in order to capture long tracks from cosmic muons crossing the TPC. We use NIM modules to require coincidences between one upper and one lower paddle set of any opposite cosmic towers. The OR all the opposite towers’ coincidences is fed as an input to the trigger card.

We use the signal from the cryogenic PMTs (see Section ??) to form several interesting triggers. The coincidence of signal from all the PMT pulses within  $\sim$ 20 ns is an indication of ionizing radiation in the TPC and forms a trigger input. The coincidence of two subsequent scintillation logic pulses delayed by a maximum of  $7\ \mu\text{s}$  forms the Michel electron trigger.

## 3.5 Control Systems

LArIAT is a complex ensemble of systems which needed to be monitored at once during data taking. We performed the monitoring of the systems operations with a slow control system, a DAQ monitoring system and a low level data quality monitoring described in the following sections.

### Slow Control

We used the Synoptic Java Web Start framework as a real-time display of subsystem conditions. Its simple Graphical User Interface allowed us to change the operating parameters and to graph the trends of several variables of interest for all the tertiary

beam detectors. Among the most important quantities monitored by Synoptic there are the level of argon in both the inner vessel and the external dewar, the operating voltages of cathode and wire planes, of the PMTs and SiPMs, and of the four wire chambers, as well as the magnets temperature. Figure 3.13 shows an example of the monitoring system. LArIAT uses the Accelerator Control NETwork system (ACNET) to monitor the beam conditions of the MCenter beamline. For example, the horizontal and vertical position of the beam at the first two wire chambers (WC1 and WC2) are shown in 3.14 as seen by the shifter during data taking.

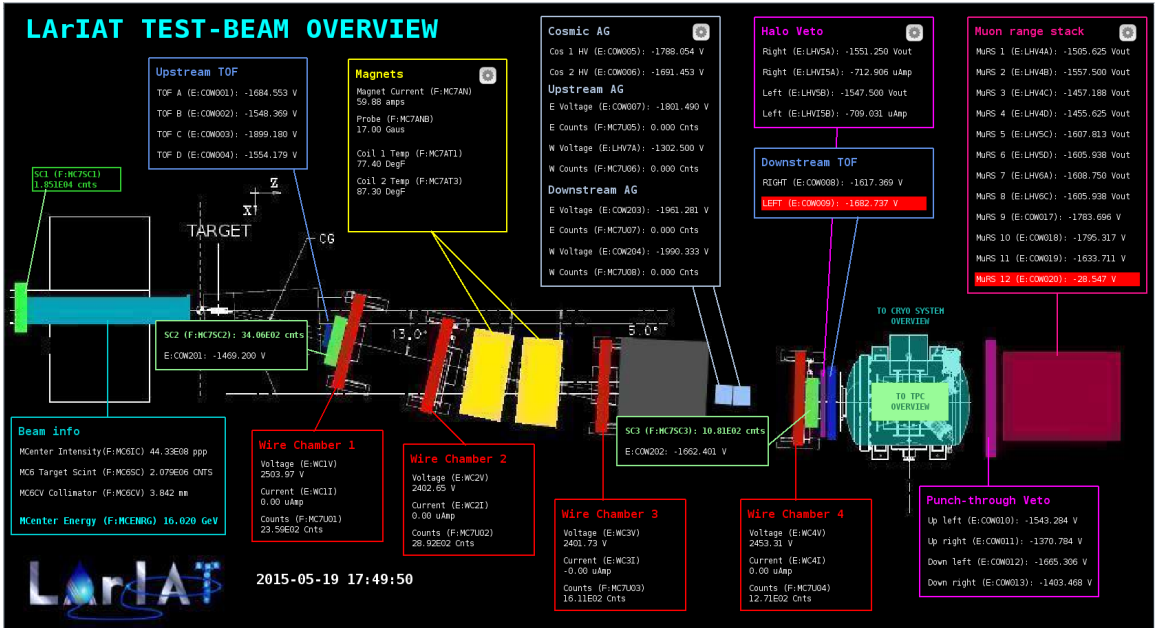


Figure 3.13: Interface of the Synoptic slow control system

## DAQ Monitoring

We monitor the data taking and the run time evolution with the Run Status Webpage (<http://lariat-wbm.fnal.gov/lariat/run.html>), a webpage updated in real-time. The page displays, among other information, the total number of triggers in the event, the total number of detectors triggered during a beam spill, the trigger patterns, the number of times a particular trigger pattern was satisfied during a beam spill, and

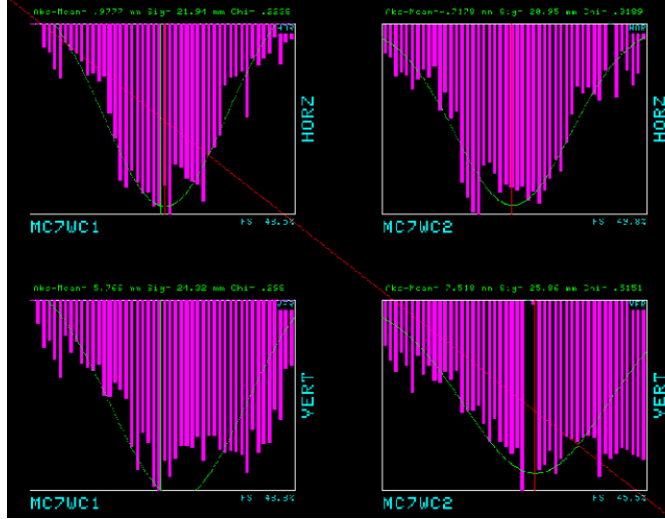


Figure 3.14: Beam position at the upstream wire chambers monitored with ACNET.

the current time relative to the Fermilab accelerator complex supercycle. A screen shot of the page is show in figure 3.15.

## Data Quality Monitoring

We employ two systems to ensure the quality of our data during data taking: the Near-Real-Time Data Quality Monitoring and the Event Viewer.

The Near-Real-Time Data Quality Monitoring (DQM) is a webpage which receives updates from all the VME boards in the trigger system and displays the results of a quick analysis of the DAQ stream of raw data on a spill-by-spill basis. The DQM allows the shifter to monitor almost in real time (typically with a 2-minute delay) a series of low level-quantities and compare them to past collections of beam spills. Some of the variables monitored in the DQM are the pedestal mean and RMS on CAEN digitizer boards of the TPC wires and PMTs of the beamline detectors, the hit occupancy and timing plots on the wire chambers, and number of data fragments recorded that are used to build a TPC event. Abnormal values for low-level quantity in the data activate a series of alarms in the DQM; this quick feedback on the DAQ and beam conditions is fundamental to assure a fast debugging of the detector and a

very efficient data taking during beam uptime.

The online Event Viewer displays a two dimensional representation of LArIAT TPC events on both the Induction and the Collection planes in near real time. The raw pulses collected by the DAQ on each wire are plotted as a function of drift time, resulting in an image of the TPC event easily readable by the shifter. This tool guarantees a particularly good check of the TPC operation which activate an immediate feedback for troubleshooting a number of issues. For example, it is easy for the shifter to spot high occupancy events and request a reduction of the primary beam intensity, or to spot a decrease of the argon purity which requires the regeneration of filters, or to catch the presence of electronic noise and reboot the ASICs. An example of high occupancy event is shown in 3.16.

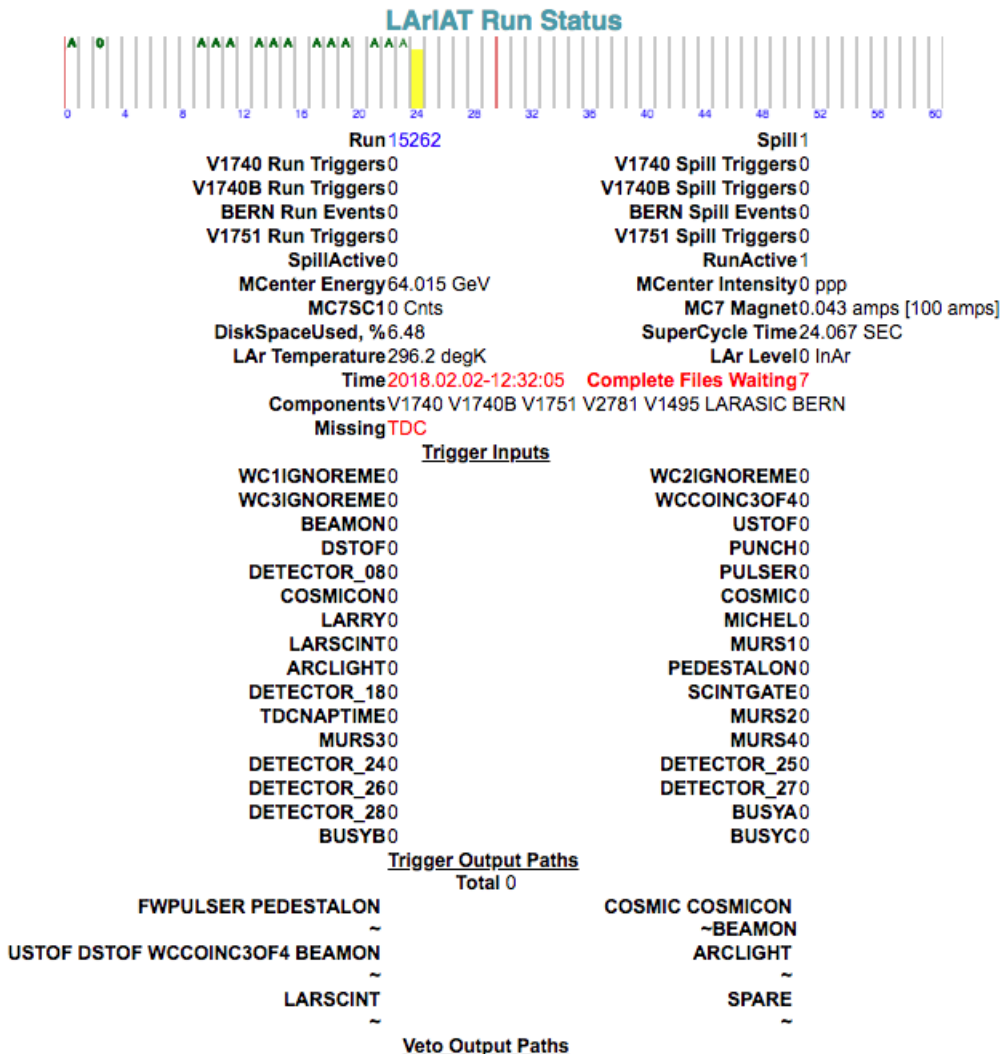


Figure 3.15: Run Status page at LArIAT downtime. At the top the yellow bar displays the current position in the Fermilab supercycle. Interesting information to be monitored by the shifter were the run number and number of spills, time elapsed from data taking (here in red), the energy of the secondary beam and the trigger paths.

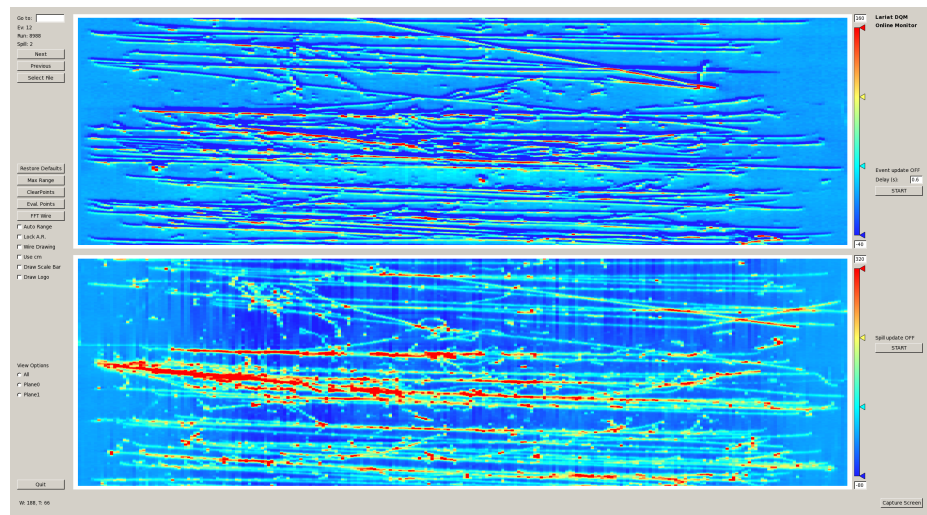


Figure 3.16: High occupancy event display: induction plane (top) and collection plane (bottom).

# Chapter 4

## Hadron Interactions in Argon: Cross Section

### 4.1 How to Measure a Hadron Cross Section in LArIAT

We use both the LArIAT beamline detectors and the LArTPC information to measure hadronic cross sections in argon. Albeit with small differences, both the  $\pi^-$  - Ar and  $K^+$  - Ar total hadronic cross section measurements rely on the same procedure described in details in the following paragraphs: we select the particle of interest using a combination of beamline detectors and TPC information (paragraph 4.1.1), we perform a handshake between the beamline information and the TPC tracking to assure we are selecting the right TPC track (paragraph 4.1.2), and we apply the “thin slice” method to get to the final result (paragraph 4.1.3). We show a cross check of this method in paragraph 4.1.4.

### 4.1.1 Event Selection

#### Beamline events

As will be clear in paragraph 4.1.3, beamline particle identification and momentum measurement before entering the TPC are fundamental information for the hadronic cross sections measurements in LArIAT. Thus, we scan the LArIAT data to keep only events whose wire chamber and time of flight information is registered. Additionally, we perform a check of the plausibility of the trajectory inside the beamline detectors: given the position of the hits in the four wire chambers, we make sure the particle trajectory does not cross any impenetrable material such as the collimator and the magnets steel.

#### Particle Identification in the beamline

In data, the main tool to establish the identity of the hadron of interest is the LArIAT tertiary beamline, in its function of mass spectrometer. We combine the measurement of the time of flight,  $TOF$ , and the beamline momentum,  $p_{Beam}$ , to reconstruct the invariant mass of the particles in the beamline,  $m_{Beam}$ , as follows

$$m_{Beam} = \frac{p_{Beam}}{c} \sqrt{\left(\frac{TOF * c}{l}\right)^2 - 1}, \quad (4.1)$$

where  $c$  is the speed of light and  $l$  is the length of the particle trajectory between the time of flight paddles.

Figure 4.1 shows the mass distribution for the Run II negative polarity runs on the left and positive polarity runs on the right. We perform the classification of events into the different samples as follows:

- $\pi, \mu, e$ :  $0 \text{ MeV} < \text{mass} < 350 \text{ MeV}$
- kaon:  $350 \text{ MeV} < \text{mass} < 650 \text{ MeV}$

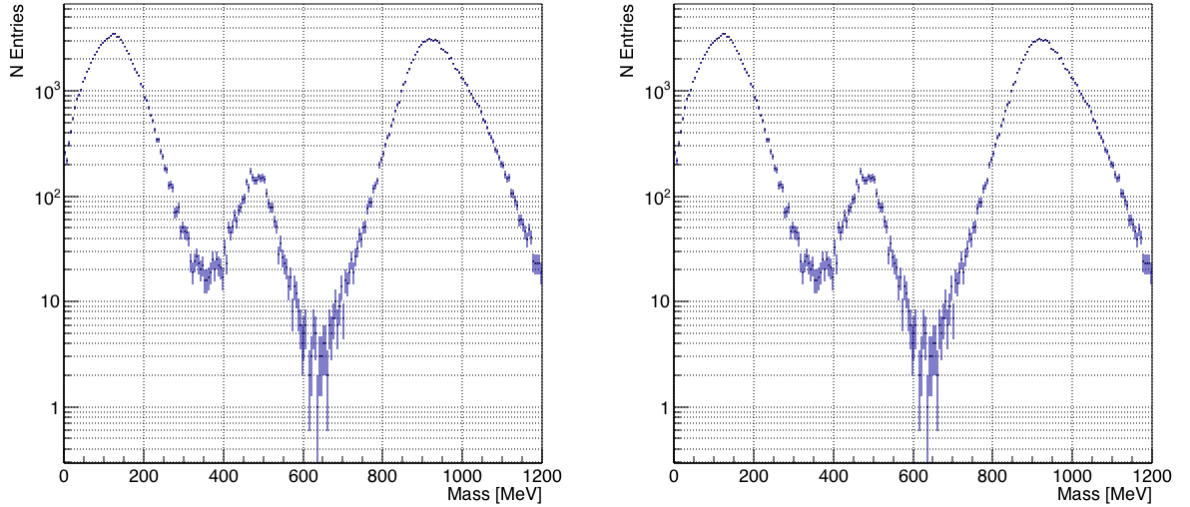


Figure 4.1: The mass plotted for a sample of Run-II events reconstructed in the beamline, negative polarity runs on the left and positive polarity runs on the right. The classification of the events into  $\pi$ ,  $\mu$ ,  $e$ , kaon, or proton is based on this distribution.  
**CHANGE PLOTS**

- proton:  $650 \text{ MeV} < \text{mass} < 3000 \text{ MeV}$ .

### Additional Particle Identification technique

In the case of the  $\pi^-$ -Ar cross section, the resolution of beamline mass spectrometer is not sufficient to select a beam of pure pions. In fact, muons and electrons survive the selection on the beamline mass value. It is important to notice that the composition of the negative polarity beam is mostly pions, as discussed in ???. Anyhow, we devise a selection on the TPC information to mitigate the presence of electrons in the sample used for the pion cross section. The selection relies on the different topologies of a pion and an electron event in the argon: while the former will trace a track inside the TPC active volume, the latter will tend to “shower”, i.e. interact with the medium, produce bremsstrahlung photons which pair convert into several short tracks. We provide details of this selection in section ??.

## Pile up mitigation

The secondary beam impinging on LArIAT secondary target produces a plethora of particles. The presence of upstream and downstream collimators greatly abates the number of particles tracing down the LArIAT beamline. However, more than one beamline particles, or particles produced from the beam interaction with the beamline detectors, may sneak into the LArTPC during its readout time. The TPC readout is triggered by the actual particle firing the beamline detectors; we call “pile up” the additional traces in the TPC. We adjusted the primary beam intensity between LArIAT Run I and Run II to minimize the presence of events with high pile up particles in the data sample. For the cross section analyses, we remove events with more than 4 tracks in the first 14 cm upstream portion of the TPC from the sample.

probably need to do a better job explaining pile up

### 4.1.2 Wire Chamber to TPC Match

For each event passing the selection on its beamline information we need to identify the track inside the TPC corresponding to the particle which triggered the beamline detectors, a procedure we refer to as “WC to TPC match” (WC2TPC for short). In general, the TPC tracking algorithm will reconstruct more than one track in the event, partially due to the fact that hadrons interact in the chamber, as shown in figure ??, and partially because of pile up particles during the triggered TPC drift time, as shown in figure ??.

ADD EVENT DISPLAYS

We attempt to uniquely match one wire chamber track to one and only one reconstructed TPC track. In data, this match leverages on a geometrical selection exploiting both the position of the wire chamber and TPC tracks, and the angle between them. We consider only TPC tracks whose first point is in the first 2 cm upstream portion of the TPC for the match. We project the wire chamber track to the TPC front face where we define the  $x_{FF}$  and  $y_{FF}$  coordinates used for evaluating

the match. We define  $\Delta X$  as the difference between the  $x$  position of the most upstream point of the TPC track and  $x_{FF}$ .  $\Delta Y$  is defined analogously. We define the radius difference,  $\Delta R$ , as  $\Delta R = \sqrt{\Delta X^2 + \Delta Y^2}$ . The angle between the incident WC track and the TPC track in the plane that contains them defines  $\alpha$ . If  $\Delta R < 4$  cm,  $\alpha < 8^\circ$ , a match between WC-track and TPC reconstructed track is found. We describe how we determinate the best value for the radius and angular selection in sec ???. In MC, we mimic the matching between the WC and the TPC track by constructing a fake WC track using truth information at wire chamber four. We then apply the same WC to TPC matching algorithm as in data. We discard events with multiple WC2TPC matches. We use only TPC track matched to WC tracks in the cross section calculation.

#### 4.1.3 The Thin Slice Method

##### Cross Sections on Thin Target

Cross section measurements on a thin target have been the bread and butter of nuclear and particle experimentalists since the Rutherford experiments NEED CITATION. At their core, this type of experiments consists in shooting a beam of particles with a known flux on a thin target and recording the outgoing flux.

In general, the target is not a single particle, but rather a slab of material containing many diffusion centers. The so-called “thin target” approximation assumes that the target centers are uniformly distributed in the material and that the target is thin compared to the interaction length so that no center of interaction sits in front of another. In this approximation, the ratio between the number of particles interacting in the target  $N_{Interacting}$  and number of incident particles  $N_{Incident}$  determines the interaction probability  $P_{Interacting}$ , which is the complementary to one of the survival

probability  $P_{Survival}$ . Equation 4.2

$$P_{Survival} = 1 - P_{Interacting} = 1 - \frac{N_{Interacting}}{N_{Incident}} = e^{-\sigma_{TOT} n \delta X} \quad (4.2)$$

describes the probability for a particle to survive the thin target. This formula relates the total cross section  $\sigma_{TOT}$ , the density of the target centers  $n$  and the thickness of the target along the incident hadron direction  $\delta X$ , to the interaction probability<sup>1</sup>. If the target is thin compared to the interaction length of the process considered, we can Taylor expand the exponential function in equation 4.2 and find a simple proportionality relationship between the number of incident and interacting particles, and the cross section, as shown in equation 4.3:

$$1 - \frac{N_{Interacting}}{N_{Incident}} = 1 - \sigma_{TOT} n \delta X + O(\delta X^2). \quad (4.3)$$

Solving for the cross section, we find:

$$\sigma_{TOT} = \frac{1}{n \delta X} \frac{N_{Interacting}}{N_{Incident}}. \quad (4.4)$$

### Not-so-Thin Target: Slicing the Argon

The LArIAT TPC, with its 90 cm of length, is not a thin target. Find expected interaction length for hadrons and kaons. However, the fine-grained tracking of the LArIAT LArTPC allows us to treat the argon volume as a sequence of many adjacent thin targets.

As described in section 3, LArIAT wire planes count 240 wires each. The wires are oriented at +/- 60° from the vertical direction at 4 mm spacing, while the beam direction is oriented 3 degrees off the  $z$  axis in the  $XZ$  plane. review this math The

---

<sup>1</sup>. The scattering center density in the target,  $n$ , relates to the argon density  $\rho$ , the Avogadro number  $N_A$  and the argon molar mass  $m_A$  as  $n = \frac{\rho N_A}{m_A}$ .

wires collect signals proportional to the energy loss of the hadron along its path in a  $\delta X = 4 \text{ mm}/\sin(60^\circ) \approx 4.7 \text{ mm}$  slab of liquid argon. Thus, one can think to slice the TPC into many thin targets of  $\delta X = 4.7 \text{ mm}$  thickness along the direction of the incident particle.

Considering each slice  $j$  a “thin target”, we can apply the cross section calculation from Eq. 4.4 iteratively, evaluating the kinetic energy of the hadron as it enters each slice,  $E_j^{kin}$ . For each WC-to-TPC matched particle, the energy of the hadron entering the TPC is known thanks to the momentum and mass determination by the tertiary beamline,

$$E_{FrontFace}^{kin} = \sqrt{p_{Beam}^2 - m_{Beam}^2} - m_{Beam} - E_{loss}, \quad (4.5)$$

where  $E_{loss}$  is a correction for the energy loss in the dead material between the beamline and the TPC front face (more on ??). The energy of the hadron at the each slab is determined by subtracting the energy released by the particle in the previous slabs. For example, at the  $j^{th}$  point of a track, the kinetic energy will be

$$E_j^{kin} = E_{FrontFace}^{kin} - \sum_{i < j} \Delta E_i, \quad (4.6)$$

where  $\Delta E_i$  is the energy deposited at each argon slice before the  $j^{th}$  point as measured by the calorimetry associated with the tracking.

If the particle enters a slice, it contributes to  $N_{Incident}(E^{kin})$  in the energy bin corresponding to its kinetic energy in that slice. If it interacts in the slice, it then also contributes to  $N_{Interacting}(E^{kin})$  in the appropriate energy bin. The cross section as a function of kinetic energy,  $\sigma_{TOT}(E^{kin})$  will then be proportional to the ratio  $\frac{N_{Interacting}(E^{kin})}{N_{Incident}(E^{kin})}$ .

The statistical uncertainty for each energy bin is calculated by error propagation from the statistical uncertainty on  $N_{Incident}$  and  $N_{Interacting}$ . Since the number of

incident hadrons in each energy bin is given by a simple counting, we assume that  $N_{Incident}$  is distributed as a poissonian with mean and  $\sigma^2$  equal to  $N_{Incident}$  in each bin. On the other hand,  $N_{Interacting}$  follows a binomial distribution: a particle in a given energy bin might or might not interact. The square of the variance for the binomial is given by

$$\sigma^2 = \mathcal{N}P_{Interacting}(1 - P_{Interacting}); \quad (4.7)$$

since the interaction probability  $P_{Interacting}$  is  $\frac{N_{Interacting}}{N_{Incident}}$  and the number of tries  $\mathcal{N}$  is  $N_{Incident}$ , equation 4.7 translates into

$$\sigma^2 = N_{Incident} \frac{N_{Interacting}}{N_{Incident}} \left(1 - \frac{N_{Interacting}}{N_{Incident}}\right) = N_{Interacting} \left(1 - \frac{N_{Interacting}}{N_{Incident}}\right). \quad (4.8)$$

$N_{Incident}$  and  $N_{Interacting}$  are not independent. The uncertainty on the cross section is thus calculated as

$$\delta\sigma_{tot}(E) = \sigma_{tot}(E) \left( \frac{\delta N_{Interacting}}{N_{Interacting}} + \frac{\delta N_{Incident}}{N_{Incident}} \right) \quad (4.9)$$

where:

$$\delta N_{Incident} = \sqrt{N_{Incident}} \quad (4.10)$$

$$\delta N_{Interacting} = \sqrt{N_{Interacting} \left(1 - \frac{N_{Interacting}}{N_{Incident}}\right)}. \quad (4.11)$$

#### 4.1.4 Procedure testing with truth quantities

The  $\pi^-$ -Ar and  $K^+$ -Ar total hadronic cross section implemented in Geant4 can be used as a tool to validate the measurement methodology. We describe here a closure test done on Monte Carlo to prove that the methodology of slicing the TPC retrieves the underlying cross section distribution implemented in Geant4 within the statistical error.

For pions in the considered energy range, the Geant4 inelastic model adopted to is “BertiniCascade”, while the elastic model “hElasticLHEP”. For kaons, the Geant4 inelastic model adopted to is “BertiniCascade”, while the elastic model “hElasticLHEP”.

For the validation test, we fire about 390000 pions and 140000 kaons inside the LArIAT TPC active volume using the DDMC (see sec ??). We apply the thin-sliced method on using true quantities to calculate the hadron kinetic energy at each slab in order to decouple reconstruction effects to eventual issues with the methodology. For each slab of 4.7 mm length on the path of the hadron, we integrate the true energy deposition as given by the Geant4 transportation model. Then, we recursively subtracted it from the hadron kinetic energy at the TPC front face to evaluate the kinetic energy at each slab until the true interaction point is reached. Doing so, we obtain the true interacting and incident distributions for the considered hadron and we obtain the true MC cross section as a function of the hadron true kinetic energy.

Figure ?? shows the total hadronic cross section for argon implemented in Geant4 10.01.p3 (solid lines) overlaid with the true MC cross section as obtained with the sliced TPC method (markers) for pions on the left and kaons on the right; the total cross section is shown in green, the elastic cross section in blue and the inelastic cross section in red. The nice agreement with the Geant4 distribution and the cross section obtained with the sliced TPC method gives us confidence in the validity of the methodology.

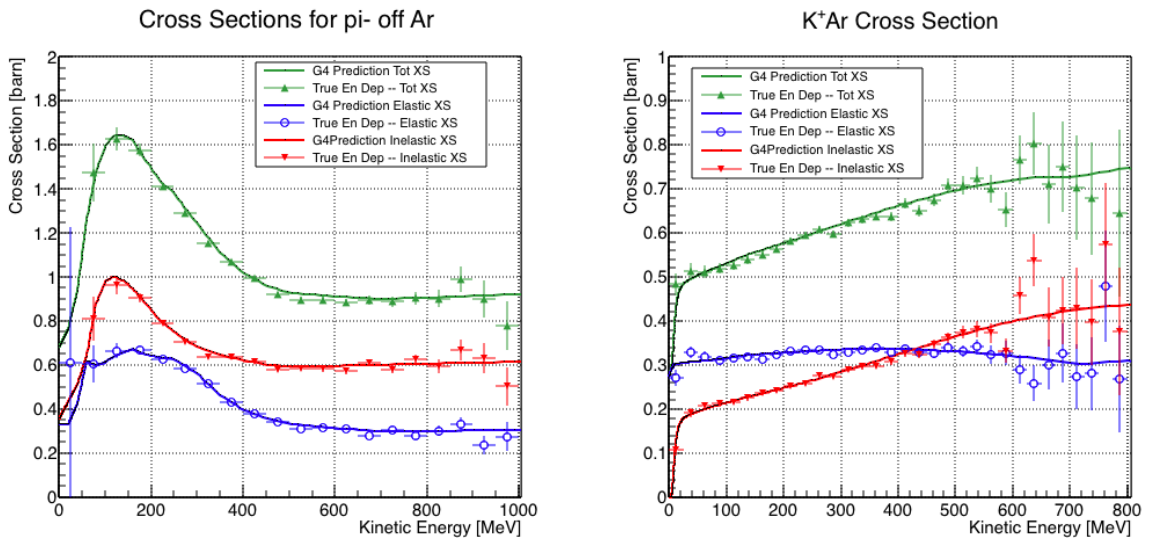


Figure 4.2: Hadronic cross sections for  $\pi^-$ -Ar (left) and  $K^+$ -Ar (right) implemented in Geant4 10.01.p3 (solid lines) overlaid the true MC cross section as obtained with the sliced TPC method (markers). The total cross section is shown in green, the elastic cross section in blue and the inelastic cross section in red.

## Appendix A

# Measurement of LArIAT Electric Field

The electric field of a LArTPC in the drift volume is a fundamental quantity for the proper functionality of this technology, as it affects almost every reconstructed quantity such as the position of hits or their collected charge. Given its importance, we calculate the electric field for LArIAT with a single line diagram from our HV circuit and we cross check the obtained value with a measurement relying only on TPC data.

Before getting into the details of the measurement procedures, it is important to explicit the relationship between some quantities in play. The electric field and the drift velocity ( $v_{drift}$ ) are related as follows

$$v_{drift} = \mu(E_{field}, T)E_{field}, \quad (\text{A.1})$$

where  $\mu$  is the electron mobility, which depends on the electric field and on the temperature (T). The empirical formula for this dependency is described in [?] and shown in Figure A.1 for several argon temperatures.

The relationship between the drift time ( $t_{drift}$ ) and the drift velocity is trivially

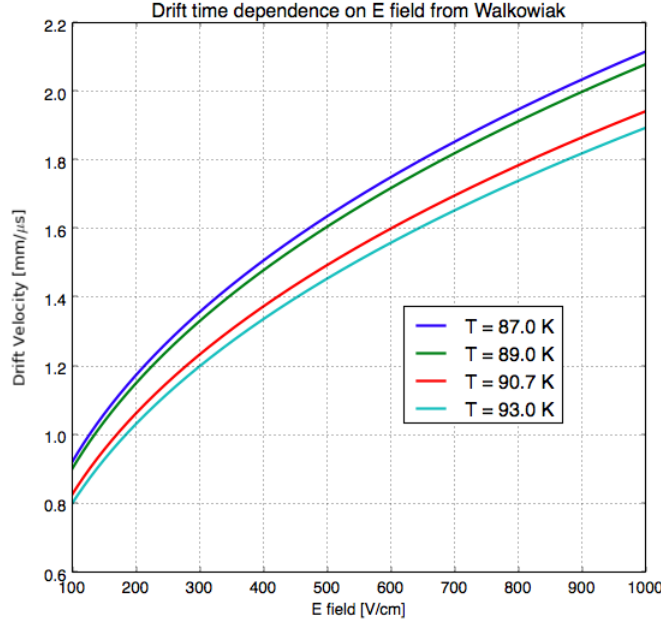


Figure A.1: Drift velocity dependence on electric field for several temperatures. The slope of the line at any one point represents the electron mobility for that given temperature and electric field.

Table A.1: Electric field and drift velocities in LArIAT smaller drift volumes

	Shield-Induction	Induction-Collection
$E_{filed}$	700.625 V/cm	892.5 V/cm
$v_{drift}$	1.73 mm/μs	1.90 mm/μs
$t_{drift}$	2.31 μs	2.11 μs

given by

$$t_{drift} = \Delta x / v_{drift}, \quad (\text{A.2})$$

where  $\Delta x$  is the distance between the edges of the drift region. Table A.1 reports the values of the electric field, drift velocity, and drift times for the smaller drift volumes.

With these basic parameters established, we can now move on to calculating the electric field in the main drift region (between the cathode and the shield plane).

## Single line diagram method

The electric field strength in the LArIAT main drift volume can be determined knowing the voltage applied to the cathode, the voltage applied at the shield plane, and the distance between them. We assume the distance between the cathode and the shield plane to be 470 mm and any length contraction due to the liquid argon is negligibly small ( $\sim 2$  mm).

The voltage applied to the cathode can be calculated using Ohm's law and the single line diagram shown in Figure A.2. A set of two filter pots for emergency power dissipation are positioned between the Glassman power supply and the cathode, one at each end of the feeder cable, each with an internal resistance of  $40 \text{ M}\Omega$ . The output current of the Glassman power supply is then used to determine the electric field strength. Figure A.3 shows an average current of 0.004172 mA from the Glassman power supply.

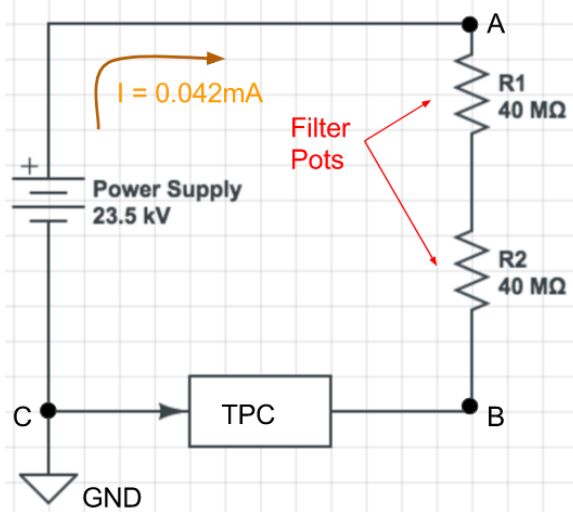


Figure A.2: get rid of current line LArIAT HV simple schematics.

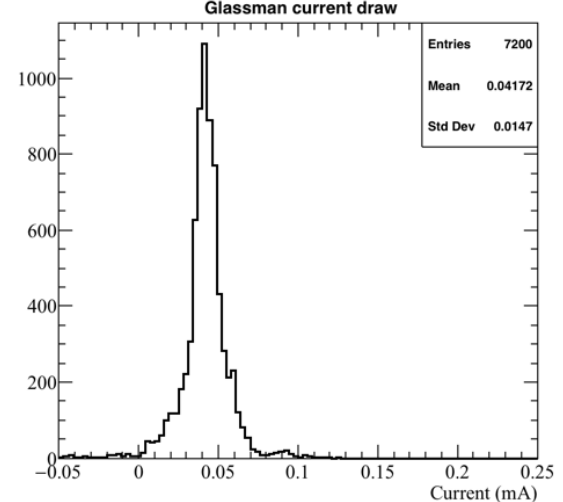


Figure A.3: **the axis is wrong!!** Current reading from the Glassman between May 25th and May 30th, 2016 (typical Run-II conditions).

Using this current, the voltage at the cathode is calculated as

$$V_{BC} = V_{PS} - (I \times R_{eq}) = -23.5 \text{ kV} + (0.00417 \text{ mA} \times 80 \text{ M}\Omega) = -23.17 \text{ kV}, \quad (\text{A.3})$$

where  $I$  is the current and  $R_{eq}$  is the equivalent resistor representing the two filter pots. The electric field, drift voltage, and drift time are then calculated to be

$$E_{\text{field}} = \frac{V_{BC} - V_{\text{shield}}}{\Delta x} = 486.54 \text{ V/cm} \quad (\text{A.4})$$

## E field using cathode-anode piercing tracks

We devise an independent method to measure the drift time (and consequently drift velocity and electric field) using TPC cathode to anode piercing tracks. We use this method as a cross check to the single line method. The basic idea is simple:

0. Select cosmic ray events with only 1 reconstructed track
1. Reduce the events to the one containing tracks that cross both anode and cathode
2. Identify the first and last hit of the track
3. Measure the time difference between these two hits ( $\Delta t$ ).

This method works under the assumptions that the time it takes for a cosmic particle to cross the chamber ( $\sim \text{ns}$ ) is small compared to the charge drift time ( $\sim \text{hundreds of } \mu\text{s}$ ).

We choose cosmic events to allow for a high number of anode to cathode piercing tracks (ACP tracks), rejecting beam events where the particles travel almost perpendicularly to drift direction. We select events with only one reconstructed track to maximize the chance of selecting a single crossing muon (no-michel electron). We utilize ACP tracks because their hits span the full drift length of the TPC, see figure

A.4, allowing us to define where the first and last hit of the tracks are located in space regardless of our assumption of the electric field.

One of the main features of this method is that it doesn't rely on the measurement of the trigger time. Since  $\Delta t$  is the time difference between the first and last hit of a track and we assume the charge started drifting at the same time for both hits, the measurement of the absolute beginning of drift time  $t_0$  is unnecessary. We boost the presence of ACP tracks in the cosmic sample by imposing the following requirements on tracks:

- vertical position (Y) of first and last hits within  $\pm 18$  cm from TPC center (avoid Top-Bottom tracks)
- horizontal position (Z) of first and last hits within 2 and 86 cm from TPC front face (avoid through going tracks)
- track length greater than 48 cm (more likely to be crossing)
- angle from the drift direction (phi in figure A.5) smaller than 50 deg (more reliable tracking)
- angle from the beam direction (theta in figure A.5) grater than 50 deg (more reliable tracking)

Tracks passing all these selection requirements are used for the  $\Delta t$  calculation.

For each track passing our selection, we loop through the associated hits in order to retrieve the timing information. The analysis is performed separately on hits on the collection plane and induction plane, but lead to consistent results. As an example of the time difference, figures A.6 and A.7 represent the difference in time between the last and first hit of the selected tracks for Run-II Positive Polarity sample on the collection and induction plane respectively. We fit with a Gaussian to the peak of the  $\Delta t$  distributions to extract the mean drift time and the uncertainty associated with

it. The long tail at low  $\Delta t$  represent contamination of non-ACP tracks in the track selection. We apply the same procedure to Run-I and Run-II, positive and negative polarity alike.

To convert  $\Delta t$  recorded for the hits on the induction plane to the drift time we utilize the formula

$$t_{drift} = \Delta t - t_{S-I} \quad (\text{A.5})$$

where  $t_{drift}$  is the time the charge takes to drift in the main volume between the cathode and the shield plane and  $t_{S-I}$  is the time it takes for the charge to drift from the shield plane to the induction plane. In Table A.1 we calculated the drift velocity in the S-I region, thus we can calculate  $t_{S-I}$  as

$$t_{S-I} = \frac{l_{S-I}}{v_{S-I}} = \frac{4mm}{1.745mm/\mu s} \quad (\text{A.6})$$

where  $l_{S-I}$  is the distance between the shield and induction plane and  $v_{S-I}$  is the drift velocity in the same region. A completely analogous procedure is followed for the hits on the collection plane, taking into account the time the charge spent in drifting from shield to induction as well as between the induction and collection plane. The value for  $\Delta t_{drift}$ , the calculated drift velocity ( $v_{drift}$ ), and corresponding drift electric field for the various run periods is given in Table A.2 and are consistent with the electric field value calculated with the single line diagram method.

### Delta $t_{drift}$ , drift v and E field with ACP tracks

Data Period	$\Delta t_{Drift}$ [ $\mu s$ ]	Drift velocity [mm/ $\mu s$ ]	E field [V/cm]
RunI Positive Polarity Induction	$311.1 \pm 2.4$	$1.51 \pm 0.01$	$486.6 \pm 21$
RunI Positive Polarity Collection	$310.9 \pm 2.6$	$1.51 \pm 0.01$	$487.2 \pm 21$
RunII Positive Polarity Induction	$315.7 \pm 2.8$	$1.49 \pm 0.01$	$467.9 \pm 21$
RunII Positive Polarity Collection	$315.7 \pm 2.7$	$1.49 \pm 0.01$	$467.9 \pm 21$
RunII Negative Polarity Induction	$315.9 \pm 2.6$	$1.49 \pm 0.01$	$467.1 \pm 21$
RunII Negative Polarity Collection	$315.1 \pm 2.8$	$1.49 \pm 0.01$	$470.3 \pm 21$
Average Values	314.1	$1.50 \pm 0.01$	$474.3 \pm 21$

Table A.2:  $\Delta t$  for the different data samples used for the Anode-Cathode Piercing tracks study.

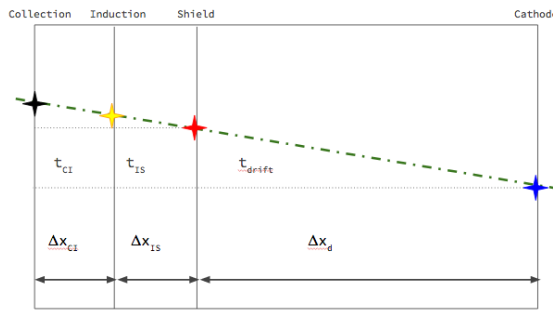


Figure A.4: Pictorial representation of the YX view of the TPC. The distance within the anode planes and between the shield plane and the cathode is purposely out of proportion to illustrate the time difference between hits on collection and induction. A ACP track is shown as an example.

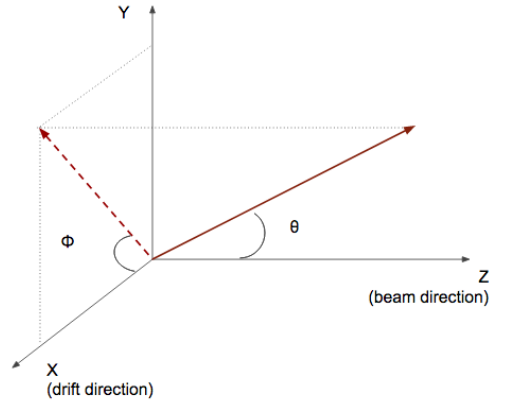


Figure A.5: Angle definition in the context of LArIAT coordinates system.

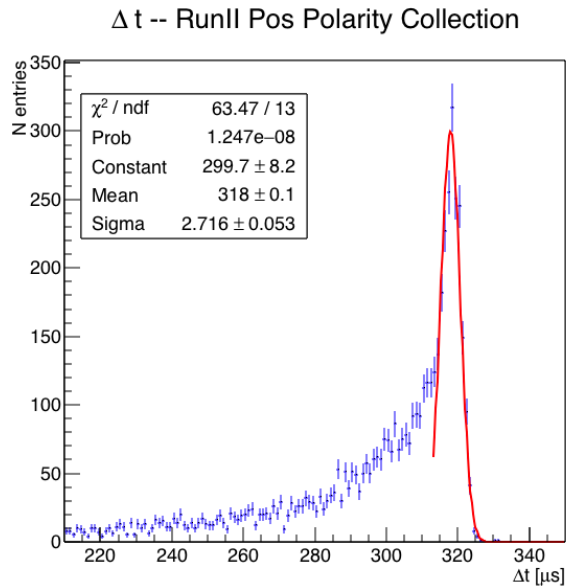


Figure A.6: Collection plane  $\Delta t$  fit for Run II positive polarity ACP data selected tracks.

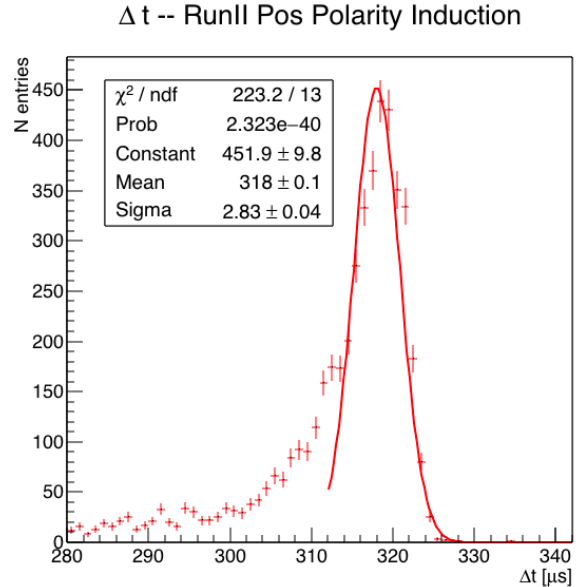


Figure A.7: Induction plane  $\Delta t$  fit for Run II positive polarity ACP data selected tracks.

# Bibliography

- [1] Precision electroweak measurements on the  $Z$  resonance. *Physics Reports*, 427(5):257 – 454, 2006.
- [2] K. Abe, J. Amey, C. Andreopoulos, M. Antonova, S. Aoki, A. Ariga, D. Autiero, S. Ban, M. Barbi, G. J. Barker, G. Barr, C. Barry, P. Bartet-Friburg, M. Batkiewicz, V. Berardi, S. Berkman, S. Bhadra, S. Bienstock, A. Blondel, S. Bolognesi, S. Bordoni, S. B. Boyd, D. Brailsford, A. Bravar, C. Bronner, M. Buizza Avanzini, R. G. Calland, T. Campbell, S. Cao, S. L. Cartwright, M. G. Catanesi, A. Cervera, C. Checchia, D. Cherdack, N. Chikuma, G. Christodoulou, A. Clifton, J. Coleman, G. Collazuol, D. Coplowe, A. Cudd, A. Dabrowska, G. De Rosa, T. Dealtry, P. F. Denner, S. R. Dennis, C. Densham, D. Dewhurst, F. Di Lodovico, S. Di Luise, S. Dolan, O. Drapier, K. E. Duffy, J. Du-marchez, M. Dziewiecki, S. Emery-Schrenk, A. Ereditato, T. Feusels, A. J. Finch, G. A. Fiorentini, M. Friend, Y. Fujii, D. Fukuda, Y. Fukuda, V. Galy-mov, A. Garcia, C. Giganti, F. Gizzarelli, T. Golan, M. Gonin, D. R. Hadley, L. Haegel, M. D. Haigh, D. Hansen, J. Harada, M. Hartz, T. Hasegawa, N. C. Hastings, T. Hayashino, Y. Hayato, R. L. Helmer, A. Hillairet, T. Hiraki, A. Hiramoto, S. Hirota, M. Hogan, J. Holeczek, F. Hosomi, K. Huang, A. K. Ichikawa, M. Ikeda, J. Imber, J. Insler, R. A. Intonti, T. Ishida, T. Ishii, E. Iwai, K. Iwamoto, A. Izmaylov, B. Jamieson, M. Jiang, S. Johnson, P. Jonsson, C. K. Jung, M. Kabirnezhad, A. C. Kabeth, T. Kajita, H. Kakuno, J. Kameda,

D. Karlen, T. Katori, E. Kearns, M. Khabibullin, A. Khotjantsev, H. Kim, J. Kim, S. King, J. Kisiel, A. Knight, A. Knox, T. Kobayashi, L. Koch, T. Koga, A. Konaka, K. Kondo, L. L. Kormos, A. Korzenev, Y. Koshio, K. Kowalik, W. Kropp, Y. Kudenko, R. Kurjata, T. Kutter, J. Lagoda, I. Lamont, M. Lamoureux, E. Larkin, P. Lasorak, M. Laveder, M. Lawe, M. Licciardi, T. Lindner, Z. J. Liptak, R. P. Litchfield, X. Li, A. Longhin, J. P. Lopez, T. Lou, L. Ludovici, X. Lu, L. Magaletti, K. Mahn, M. Malek, S. Manly, A. D. Marino, J. F. Martin, P. Martins, S. Martynenko, T. Maruyama, V. Matveev, K. Mavrokordis, W. Y. Ma, E. Mazzucato, M. McCarthy, N. McCauley, K. S. McFarland, C. McGrew, A. Mefodiev, C. Metelko, M. Mezzetto, P. Mijakowski, A. Minamino, O. Mineev, S. Mine, A. Missant, M. Miura, S. Moriyama, Th. A. Mueller, J. Myslik, T. Nakadaira, M. Nakahata, K. G. Nakamura, K. Nakamura, K. D. Nakamura, Y. Nakanishi, S. Nakayama, T. Nakaya, K. Nakayoshi, C. Nantais, C. Nielsen, M. Nirko, K. Nishikawa, Y. Nishimura, P. Novella, J. Nowak, H. M. O'Keeffe, K. Okumura, T. Okusawa, W. Oryszczak, S. M. Oser, T. Ovsyannikova, R. A. Owen, Y. Oyama, V. Palladino, J. L. Palomino, V. Paolone, N. D. Patel, P. Paudyal, M. Pavin, D. Payne, J. D. Perkin, Y. Petrov, L. Pickard, L. Pickering, E. S. Pinzon Guerra, C. Pistillo, B. Popov, M. Posiadala-Zezula, J.-M. Poutissou, R. Poutissou, P. Przewlocki, B. Quilain, T. Radermacher, E. Radicioni, P. N. Ratoff, M. Ravonel, M. A. Rayner, A. Redij, E. Reinherz-Aronis, C. Riccio, P. A. Rodrigues, E. Rondio, B. Rossi, S. Roth, A. Rubbia, A. Rychter, K. Sakashita, F. Sánchez, E. Scantamburlo, K. Scholberg, J. Schwehr, M. Scott, Y. Seiya, T. Sekiguchi, H. Sekiya, D. Sgalaberna, R. Shah, A. Shaikhiev, F. Shaker, D. Shaw, M. Shiozawa, T. Shirahige, S. Short, M. Smy, J. T. Sobczyk, H. Sobel, M. Sorel, L. Southwell, J. Steinmann, T. Stewart, P. Stowell, Y. Suda, S. Suvorov, A. Suzuki, S. Y. Suzuki, Y. Suzuki, R. Tacik, M. Tada, A. Takeda, Y. Takeuchi, H. K. Tanaka, H. A. Tanaka, D. Terhorst, R. Terri, T. Thakore, L. F. Thompson,

S. Tobayama, W. Toki, T. Tomura, C. Touramanis, T. Tsukamoto, M. Tzanov, Y. Uchida, M. Vagins, Z. Vallari, G. Vasseur, T. Vladislavljevic, T. Wachala, C. W. Walter, D. Wark, M. O. Wascko, A. Weber, R. Wendell, R. J. Wilkes, M. J. Wilking, C. Wilkinson, J. R. Wilson, R. J. Wilson, C. Wret, Y. Yamada, K. Yamamoto, M. Yamamoto, C. Yanagisawa, T. Yano, S. Yen, N. Yershov, M. Yokoyama, K. Yoshida, T. Yuan, M. Yu, A. Zalewska, J. Zalipska, L. Zambelli, K. Zaremba, M. Ziembicki, E. D. Zimmerman, M. Zito, and J. Žmuda. Combined analysis of neutrino and antineutrino oscillations at t2k. *Phys. Rev. Lett.*, 118:151801, Apr 2017.

- [3] R Acciarri, C Adams, J Asaadi, B Baller, T Bolton, C Bromberg, F Cavanna, E Church, D Edmunds, A Ereditato, S Farooq, B Fleming, H Greenlee, G Horton-Smith, C James, E Klein, K Lang, P Laurens, D McKee, R Mehdiyev, B Page, O Palamara, K Partyka, G Rameika, B Rebel, M Soderberg, J Spitz, A M Szelc, M Weber, M Wojcik, T Yang, and G P Zeller. A study of electron recombination using highly ionizing particles in the argoneut liquid argon tpc. *Journal of Instrumentation*, 8(08):P08005, 2013.
- [4] R Acciarri, M Antonello, B Baibussinov, M Baldo-Ceolin, P Benetti, F Calaprice, E Calligarich, M Cambiaghi, N Canci, F Carbonara, F Cavanna, S Centro, A G Cocco, F Di Pompeo, G Fiorillo, C Galbiati, V Gallo, L Grandi, G Meng, I Modena, C Montanari, O Palamara, L Pandola, G B Piano Mortari, F Pietropaolo, G L Raselli, M Roncadelli, M Rossella, C Rubbia, E Segreto, A M Szelc, S Ventura, and C Vignoli. Effects of nitrogen contamination in liquid argon. *Journal of Instrumentation*, 5(06):P06003, 2010.
- [5] R. Acciarri et al. Demonstration and Comparison of Operation of Photomultiplier Tubes at Liquid Argon Temperature. *JINST*, 7:P01016, 2012.

- [6] P. Adamson, L. Aliaga, D. Ambrose, N. Anfimov, A. Antoshkin, E. Arrieta-Diaz, K. Augsten, A. Aurisano, C. Backhouse, M. Baird, B. A. Bambah, K. Bays, B. Behera, S. Bending, R. Bernstein, V. Bhatnagar, B. Bhuyan, J. Bian, T. Blackburn, A. Bolshakova, C. Bromberg, J. Brown, G. Brunetti, N. Buchanan, A. Butkevich, V. Bychkov, M. Campbell, E. Catano-Mur, S. Childress, B. C. Choudhary, B. Chowdhury, T. E. Coan, J. A. B. Coelho, M. Colo, J. Cooper, L. Corwin, L. Cremonesi, D. Cronin-Hennessy, G. S. Davies, J. P. Davies, P. F. Derwent, R. Dharmapalan, P. Ding, Z. Djurcic, E. C. Dukes, H. Duyang, S. Edayath, R. Ehrlich, G. J. Feldman, M. J. Frank, M. Gabrielyan, H. R. Gallagher, S. Germani, T. Ghosh, A. Giri, R. A. Gomes, M. C. Goodman, V. Grichine, R. Group, D. Grover, B. Guo, A. Habig, J. Hartnell, R. Hatcher, A. Hatzikoutelis, K. Heller, A. Himmel, A. Holin, J. Hylen, F. Jediny, M. Judah, G. K. Kafka, D. Kalra, S. M. S. Kasahara, S. Kasetti, R. Keloth, L. Kolupaeva, S. Kotelnikov, I. Kourbanis, A. Kreymer, A. Kumar, S. Kurbanov, K. Lang, W. M. Lee, S. Lin, J. Liu, M. Lokajicek, J. Lozier, S. Luchuk, K. Maan, S. Magill, W. A. Mann, M. L. Marshak, K. Matera, V. Matveev, D. P. Méndez, M. D. Messier, H. Meyer, T. Miao, W. H. Miller, S. R. Mishra, R. Mohanta, A. Moren, L. Mualem, M. Muether, S. Mufson, R. Murphy, J. Musser, J. K. Nelson, R. Nichol, E. Niner, A. Norman, T. Nosek, Y. Oksuzian, A. Olshevskiy, T. Olson, J. Paley, P. Pandey, R. B. Patterson, G. Pawloski, D. Pershey, O. Petrova, R. Petti, S. Phan-Budd, R. K. Plunkett, R. Poling, B. Potukuchi, C. Principato, F. Psihas, A. Radovic, R. A. Rameika, B. Rebel, B. Reed, D. Rocco, P. Rojas, V. Ryabov, K. Sachdev, P. Sail, O. Samoylov, M. C. Sanchez, R. Schroeter, J. Sepulveda-Quiroz, P. Shanahan, A. Sheshukov, J. Singh, J. Singh, P. Singh, V. Singh, J. Smolik, N. Solomey, E. Song, A. Sousa, K. Soustruznik, M. Strait, L. Suter, R. L. Talaga, M. C. Tamsett, P. Tas, R. B. Thayyullathil, J. Thomas, X. Tian, S. C. Tognini, J. Tripathi, A. Tsaris, J. Urheim, P. Vahle, J. Vasel,

- L. Vinton, A. Vold, T. Vrba, B. Wang, M. Wetstein, D. Whittington, S. G. Wojcicki, J. Wolcott, N. Yadav, S. Yang, J. Zalesak, B. Zamorano, and R. Zwaska. Constraints on oscillation parameters from  $\nu_e$  appearance and  $\nu_\mu$  disappearance in nova. *Phys. Rev. Lett.*, 118:231801, Jun 2017.
- [7] A. Aguilar-Arevalo et al. Evidence for neutrino oscillations from the observation of anti-neutrino(electron) appearance in a anti-neutrino(muon) beam. *Phys. Rev.*, D64:112007, 2001.
- [8] A. A. Aguilar-Arevalo et al. Improved Search for  $\bar{\nu}_\mu \rightarrow \bar{\nu}_e$  Oscillations in the MiniBooNE Experiment. *Phys. Rev. Lett.*, 110:161801, 2013.
- [9] C. Anderson et al. The ArgoNeuT Detector in the NuMI Low-Energy beam line at Fermilab. *JINST*, 7:P10019, 2012.
- [10] C. Andreopoulos et al. The GENIE Neutrino Monte Carlo Generator. *Nucl. Instrum. Meth.*, A614:87–104, 2010.
- [11] M. Antonello, B. Baibussinov, P. Benetti, E. Calligarich, N. Canci, S. Centro, A. Cesana, K. Cieslik, D. B. Cline, A. G. Cocco, A. Dabrowska, D. Dequal, A. Dermenev, R. Dolfini, C. Farnese, A. Fava, A. Ferrari, G. Fiorillo, D. Gibin, S. Gninenko, A. Guglielmi, M. Haranczyk, J. Holeczek, A. Ivashkin, J. Kisiel, I. Kochanek, J. Lagoda, S. Mania, A. Menegolli, G. Meng, C. Montanari, S. Otwinowski, A. Piazzoli, P. Picchi, F. Pietropaolo, P. Plonski, A. Rappoldi, G. L. Raselli, M. Rossella, C. Rubbia, P. Sala, A. Scaramelli, E. Segreto, F. Sergiampietri, D. Stefan, J. Stepaniak, R. Sulej, M. Szarska, M. Terrani, F. Varanini, S. Ventura, C. Vignoli, H. Wang, X. Yang, A. Zalewska, and K. Zaremba. Precise 3d track reconstruction algorithm for the ICARUS t600 liquid argon time projection chamber detector. *Advances in High Energy Physics*, 2013:1–16, 2013.

- [12] D. Ashery, I. Navon, G. Azuelos, H. K. Walter, H. J. Pfeiffer, and F. W. Schlepütz. True absorption and scattering of pions on nuclei. *Phys. Rev. C*, 23:2173–2185, May 1981.
- [13] C. Athanassopoulos et al. Evidence for  $\nu(\mu) \rightarrow \nu(e)$  neutrino oscillations from LSND. *Phys. Rev. Lett.*, 81:1774–1777, 1998.
- [14] Borut Bajc, Junji Hisano, Takumi Kuwahara, and Yuji Omura. Threshold corrections to dimension-six proton decay operators in non-minimal {SUSY}  $su(5)$  {GUTs}. *Nuclear Physics B*, 910:1 – 22, 2016.
- [15] BASF Corp. 100 Park Avenue, Florham Park, NJ 07932 USA.
- [16] A. Bodek and J. L. Ritchie. Further studies of fermi-motion effects in lepton scattering from nuclear targets. *Phys. Rev. D*, 24:1400–1402, Sep 1981.
- [17] D. V. Bugg, R. S. Gilmore, K. M. Knight, D. C. Salter, G. H. Stafford, E. J. N. Wilson, J. D. Davies, J. D. Dowell, P. M. Hattersley, R. J. Homer, A. W. O'dell, A. A. Carter, R. J. Tapper, and K. F. Riley. Kaon-nucleon total cross sections from 0.6 to 2.65 gev/ *c*. *Phys. Rev.*, 168:1466–1475, Apr 1968.
- [18] A. S. Carroll, I. H. Chiang, C. B. Dover, T. F. Kycia, K. K. Li, P. O. Mazur, D. N. Michael, P. M. Mockett, D. C. Rahm, and R. Rubinstein. Pion-nucleus total cross sections in the (3,3) resonance region. *Phys. Rev. C*, 14:635–638, Aug 1976.
- [19] D. Casper. The nuance neutrino physics simulation, and the future. *Nuclear Physics B - Proceedings Supplements*, 112(1-3):161–170, nov 2002.
- [20] A. Cervera, A. Donini, M.B. Gavela, J.J. Gomez Cádenas, P. Hernández, O. Mena, and S. Rigolin. Golden measurements at a neutrino factory. *Nuclear Physics B*, 579(1-2):17–55, jul 2000.

- [21] ATLAS Collaboration. Observation of a new particle in the search for the standard model higgs boson with the ATLAS detector at the LHC. *Physics Letters B*, 716(1):1–29, sep 2012.
- [22] CMS Collaboration. Observation of a new boson at a mass of 125 gev with the cms experiment at the lhc. *Physics Letters B*, 716(1):30 – 61, 2012.
- [23] Stefano Dell’Oro, Simone Marcocci, Matteo Viel, and Francesco Vissani. Neutrinoless double beta decay: 2015 review. *Advances in High Energy Physics*, 2016:1–37, 2016.
- [24] Savas Dimopoulos, Stuart Raby, and Frank Wilczek. Proton Decay in Supersymmetric Models. *Phys. Lett.*, B112:133, 1982.
- [25] D. Drakoulakos et al. Proposal to perform a high-statistics neutrino scattering experiment using a fine-grained detector in the NuMI beam. 2004.
- [26] A Ereditato, C C Hsu, S Janos, I Kreslo, M Messina, C Rudolf von Rohr, B Rossi, T Strauss, M S Weber, and M Zeller. Design and operation of argontube: a 5 m long drift liquid argon tpc. *Journal of Instrumentation*, 8(07):P07002, 2013.
- [27] Torleif Ericson and Wolfram Weise. *Pions and Nuclei (The International Series of Monographs on Physics)*. Oxford University Press, 1988.
- [28] A.A. Aguilar-Arevalo et al. The miniboone detector. *Nuclear Instruments and Methods in Physics Research Section A: Accelerators, Spectrometers, Detectors and Associated Equipment*, 599(1):28 – 46, 2009.
- [29] Antonio Bueno et al. Nucleon decay searches with large liquid argon TPC detectors at shallow depths: atmospheric neutrinos and cosmogenic backgrounds. *Journal of High Energy Physics*, 2007(04):041–041, apr 2007.

- [30] A.S. Clough et al. Pion-nucleus total cross sections from 88 to 860 MeV. *Nuclear Physics B*, 76(1):15–28, jul 1974.
- [31] B.W. Allardye et al. Pion reaction cross sections and nuclear sizes. *Nuclear Physics A*, 209(1):1 – 51, 1973.
- [32] C Athanassopoulos et al. The liquid scintillator neutrino detector and LAMPF neutrino source. *Nuclear Instruments and Methods in Physics Research Section A: Accelerators, Spectrometers, Detectors and Associated Equipment*, 388(1-2):149–172, mar 1997.
- [33] F. Binon et al. Scattering of negative pions on carbon. *Nuclear Physics B*, 17(1):168 – 188, 1970.
- [34] L. Aliaga et al. Minerva neutrino detector response measured with test beam data. *Nuclear Instruments and Methods in Physics Research Section A: Accelerators, Spectrometers, Detectors and Associated Equipment*, 789:28 – 42, 2015.
- [35] M Adamowski et al. The liquid argon purity demonstrator. *Journal of Instrumentation*, 9(07):P07005, 2014.
- [36] P. Vilain et al. Coherent single charged pion production by neutrinos. *Physics Letters B*, 313(1-2):267–275, aug 1993.
- [37] H Fenker. Standard beam pwc for fermilab. Technical report, Fermi National Accelerator Lab., Batavia, IL (USA), 1983.
- [38] H Fesbach. Theoretical nuclear physics: Nuclear reactions. 1992.
- [39] J. A. Formaggio and G. P. Zeller. From ev to eev: Neutrino cross sections across energy scales. *Rev. Mod. Phys.*, 84:1307–1341, Sep 2012.
- [40] E. Friedman et al. K+ nucleus reaction and total cross-sections: New analysis of transmission experiments. *Phys. Rev.*, C55:1304–1311, 1997.

- [41] V.M. Gehman, S.R. Seibert, K. Rielage, A. Hime, Y. Sun, D.-M. Mei, J. Maassen, and D. Moore. Fluorescence efficiency and visible re-emission spectrum of tetraphenyl butadiene films at extreme ultraviolet wavelengths. *Nuclear Instruments and Methods in Physics Research Section A: Accelerators, Spectrometers, Detectors and Associated Equipment*, 654(1):116 – 121, 2011.
- [42] Howard Georgi and S. L. Glashow. Unity of all elementary-particle forces. *Phys. Rev. Lett.*, 32:438–441, Feb 1974.
- [43] D.Y. Wong (editor) G.L. Shaw (Editor). *Pion-nucleon Scattering*. John Wiley & Sons Inc, 1969.
- [44] Glassman High Voltage, Inc., Precision Regulated High Voltage DC Power Supply.
- [45] D S Gorbunov. Sterile neutrinos and their role in particle physics and cosmology. *Physics-Uspekhi*, 57(5):503, 2014.
- [46] S. Hansen, D. Jensen, G. Savage, E. Skup, and A. Soha. Fermilab test beam multi-wire proportional chamber tracking system upgrade. June 2014. International Conference on Technology and Instrumentation in Particle Physics (TIPP 2014).
- [47] J. Harada. Non-maximal  $\theta_{23}$  , large  $\theta_{13}$  and tri-bimaximal  $\theta_{12}$  via quark-lepton complementarity at next-to-leading order. *EPL (Europhysics Letters)*, 103(2):21001, 2013.
- [48] Peter W. Higgs. Broken symmetries and the masses of gauge bosons. *Physical Review Letters*, 13(16):508–509, oct 1964.
- [49] P.W. Higgs. Broken symmetries, massless particles and gauge fields. *Physics Letters*, 12(2):132–133, sep 1964.

- [50] H J Hilke. Time projection chambers. *Reports on Progress in Physics*, 73(11):116201, 2010.
- [51] C. Jarlskog. A basis independent formulation of the connection between quark mass matrices, CP violation and experiment. *Zeitschrift für Physik C Particles and Fields*, 29(3):491–497, sep 1985.
- [52] B J P Jones, C S Chiu, J M Conrad, C M Ignarra, T Katori, and M Toups. A measurement of the absorption of liquid argon scintillation light by dissolved nitrogen at the part-per-million level. *Journal of Instrumentation*, 8(07):P07011, 2013.
- [53] Cezary Juszczak, Jarosław A. Nowak, and Jan T. Sobczyk. Simulations from a new neutrino event generator. *Nuclear Physics B - Proceedings Supplements*, 159:211–216, sep 2006.
- [54] D. I. Kazakov. Beyond the standard model: In search of supersymmetry. In *2000 European School of high-energy physics, Caramulo, Portugal, 20 Aug-2 Sep 2000: Proceedings*, pages 125–199, 2000.
- [55] Dae-Gyu Lee, R. N. Mohapatra, M. K. Parida, and Merostar Rani. Predictions for the proton lifetime in minimal nonsupersymmetric  $so(10)$  models: An update. *Phys. Rev. D*, 51:229–235, Jan 1995.
- [56] Jorge L. Lopez and Dimitri V. Nanopoulos. Flipped SU(5): Origins and recent developments. In *15th Johns Hopkins Workshop on Current Problems in Particle Theory: Particle Physics from Underground to Heaven Baltimore, Maryland, August 26-28, 1991*, pages 277–297, 1991.
- [57] Vincent Lucas and Stuart Raby. Nucleon decay in a realistic  $so(10)$  susy gut. *Phys. Rev. D*, 55:6986–7009, Jun 1997.

- [58] Ettore Majorana. Teoria simmetrica dell'elettrone e del positrone. *Il Nuovo Cimento*, 14(4):171–184, apr 1937.
- [59] Hisakazu Minakata and Alexei Yu. Smirnov. Neutrino mixing and quark-lepton complementarity. *Phys. Rev. D*, 70:073009, Oct 2004.
- [60] FM Newcomer, S Tedja, R Van Berg, J Van der Spiegel, and HH Williams. A fast, low power, amplifier-shaper-discriminator for high rate straw tracking systems. *IEEE Transactions on Nuclear Science*, 40(4):630–636, 1993.
- [61] Emmy Noether. Invariant variation problems. *Transport Theory and Statistical Physics*, 1(3):186–207, jan 1971.
- [62] Irene Nutini. Study of charged particles interaction processes on ar in the 0.2 - 2.0 GeV energy range through combined information from ionization free charge and scintillation light. Technical report, jan 2015.
- [63] S. Pascoli, S.T. Petcov, and A. Riotto. Leptogenesis and low energy cp-violation in neutrino physics. *Nuclear Physics B*, 774(1):1 – 52, 2007.
- [64] C. Patrignani et al. Review of Particle Physics. *Chin. Phys.*, C40(10):100001, 2016.
- [65] B. Pontecorvo. Neutrino Experiments and the Problem of Conservation of Leptonic Charge. *Sov. Phys. JETP*, 26:984–988, 1968. [Zh. Eksp. Teor. Fiz.53,1717(1967)].
- [66] Martti Raidal. Relation between the neutrino and quark mixing angles and grand unification. *Phys. Rev. Lett.*, 93:161801, Oct 2004.
- [67] Steve Ritz et al. Building for Discovery: Strategic Plan for U.S. Particle Physics in the Global Context. 2014.

- [68] L.M. Saunders. Electromagnetic production of pions from nuclei. *Nucl. Phys.*, *B7*: 293–310(1968).
- [69] Qaisar Shafi and Zurab Tavartkiladze. Neutrino democracy, fermion mass hierarchies, and proton decay from 5d su(5). *Phys. Rev. D*, 67:075007, Apr 2003.
- [70] Sigma-Aldrich, P.O. Box 14508, St. Louis, MO 63178 USA.
- [71] D.R.O. Morrison N. Rivoire V. Flaminio, W.G. Moorhead. Compilation of Cross Sections I:  $\pi^+$  and  $\pi^-$  Induced Reactions. *CERN-HERA*, pages 83–01, 1983.
- [72] D.R.O. Morrison N. Rivoire V. Flaminio, W.G. Moorhead. Compilation of Cross Sections II:  $K^+$  and  $K^-$  Induced Reactions. *CERN-HERA*, pages 83–02, 1983.
- [73] Hermann Weyl. Gravitation and the electron. *Proceedings of the National Academy of Sciences of the United States of America*, 15(4):323–334, 1929.
- [74] Colin et al Wilkin. A comparison of pi+ and pi- total cross-sections of light nuclei near the 3-3 resonance. *Nucl. Phys.*, B62:61–85, 1973.
- [75] D. H. Wright and M. H. Kelsey. The Geant4 Bertini Cascade. *Nucl. Instrum. Meth.*, A804:175–188, 2015.
- [76] C. S. Wu, E. Ambler, R. W. Hayward, D. D. Hoppes, and R. P. Hudson. Experimental test of parity conservation in beta decay. *Phys. Rev.*, 105:1413–1415, Feb 1957.
- [77] N Yahlali, L M P Fernandes, K Gonzlez, A N C Garcia, and A Soriano. Imaging with sipms in noble-gas detectors. *Journal of Instrumentation*, 8(01):C01003, 2013.
- [78] T. Yanagida. Horizontal symmetry and masses of neutrinos. *Progress of Theoretical Physics*, 64(3):1103–1105, sep 1980.